

Towards Spatial Transcriptomics-driven Pathology Foundation Models

Konstantin Hemker^{*,1,2}, Andrew H. Song^{*,1,3,4}, Cristina Almagro-Pérez^{1,3,4,5}, Guillaume Jaume^{1,3,4}, Sophia J. Wagner^{1,3,4}, Anurag Vaidya^{1,3,4,5}, Nikola Simidjievski^{2,6}, Mateja Jamnik², and Faisal Mahmood^{†,1,3,4,7}

¹*Department of Pathology, Mass General Brigham, Harvard Medical School, Boston, MA, USA*

²*Department of Computer Science & Technology, University of Cambridge, Cambridge, UK*

³*Cancer Program, Broad Institute of Harvard and MIT, Cambridge, MA, USA*

⁴*Data Science Program, Dana-Farber Cancer Institute, Boston, MA, USA*

⁵*Harvard-MIT Division of Health Sciences and Technology, Massachusetts Institute of Technology, Cambridge, MA, USA*

⁶*Télécom Paris, Institut Polytechnique de Paris, Paris, France*

⁷*Harvard Data Science Initiative, Harvard University, Cambridge, MA, USA*

^{*}*Equal contribution*

[†]**Corresponding author:** Faisal Mahmood (FaisalMahmood@bwh.harvard.edu)

Abstract

Spatial transcriptomics (ST) provides spatially resolved measurements of gene expression, enabling characterization of the molecular landscape of human tissue beyond histological assessment as well as localized readouts that can be aligned with morphology. Concurrently, the success of multimodal foundation models that integrate vision with complementary modalities suggests that morphomolecular coupling between local expression and morphology can be systematically used to improve histological representations themselves. We introduce Spatial Expression-Aligned Learning (SEAL), a vision-omics self-supervised learning framework that infuses localized molecular information into pathology vision encoders. Rather than training new encoders from scratch, SEAL is designed as a parameter-efficient vision-omics finetuning method that can be flexibly applied to widely used pathology foundation models. We instantiate SEAL by training on over 700,000 paired gene expression spot-tissue region examples spanning tumor and normal samples from 14 organs. Tested across 38 slide-level and 15 patch-level downstream tasks, SEAL provides a drop-in replacement for pathology foundation models that consistently improves performance over widely used vision-only and ST prediction baselines on slide-level molecular status, pathway activity, and treatment response prediction, as well as patch-level gene expression prediction tasks. Additionally, SEAL encoders exhibit robust domain generalization on out-of-distribution evaluations and enable new cross-modal capabilities such as gene-to-image retrieval. Our work proposes a general framework for ST-guided finetuning of pathology foundation models, showing that augmenting existing models with localized molecular supervision is an effective and practical step for improving visual representations and expanding their cross-modal utility. The code is available at <https://github.com/mahmoodlab/SEAL/>.

Introduction

Computational analysis of whole-slide images (WSIs) relies on models that can encode regions of interest (ROIs or “patches”) or entire tissue slides into low-dimensional, informative embeddings^{1–4}. Recently, pathology foundation models (FMs), trained either on large histopathology image collections (*vision-only*)^{5–10} or on paired histopathology images and captions (*vision-language*)^{11–17}, have improved performance for diagnostic and prognostication tasks. Concurrently, several studies have extended these frameworks to incorporate molecular signals, especially bulk RNA sequencing^{18–20}. However, such bulk readouts lack the spatial resolution required to link fine-grained morphological patterns to their molecular correlates. As a result, current multimodal approaches underutilize spatially resolved morphology–molecular pairs that could support more nuanced tissue representations.

Spatial transcriptomics (ST) directly addresses this limitation by providing spatially resolved gene expression profiles that can be registered to the underlying histomorphology^{21–25}. While the earlier studies primarily remained within the ST domain, based on the analysis of spatially variable genes followed by qualitative correlation with underlying morphology^{21,26,27}, recent works have focused on integrative analysis of both domains. Specifically, the local integration of morphology and molecular state, enabled by the co-registration of two modalities, has been leveraged to produce image representations optimized to predict gene expression profiles from ROIs^{28–37}. However, it has not been established how and to what extent we can build general-purpose ST-guided pathology FMs that improve representation quality beyond ST prediction tasks.

We hypothesize that cohesive vision–omics alignment, trained on diverse paired morphology image patch and ST datasets^{22,25,38}, can enhance image-based downstream clinical tasks, for which pathology FMs already play a crucial role, whilst further enabling new tasks such as cross-modal prediction or retrieval³⁹. With a spectrum of pathology FMs already exhibiting strong downstream performance and the paired morphology-ST pretraining datasets being smaller than typical FM pretraining datasets due to sequencing costs, we identify two crucial requirements for successful vision-omics foundation models. First, the model needs to leverage the already strong morphological representations and finetune existing pathology FMs in a data-efficient manner. Second, the vision-omics alignment recipe needs to be generalizable enough to cater to a range of pathology FMs that harbor different architectures, training data distributions, and pretraining methods.

In this context, we introduce **Spatial Expression-Aligned Learning** (SEAL), a self-supervised vision-omics learning framework for ST-guided pathology FMs, designed to augment prior learned morphological knowledge with localized molecular information, using a computationally efficient finetuning scheme. Concretely, SEAL finetunes widely-used pathology FMs by integrating their patch embeddings with the corresponding Visium ST profiles. Our training objective combines a *contrastive loss*, which aligns vision and

omics embeddings in a shared space, with a *reconstruction loss* that enables accurate prediction of transcriptomic profiles from image patches alone. To mitigate catastrophic forgetting of pretrained features⁴⁰, SEAL uses low-rank adaptation matrices on top of the original backbone weights, preserving morphological representations while integrating molecular signal. This yields general-purpose patch-level FMs with improved vision embeddings as gene-to-image and image-to-gene retrieval capabilities. We train SEAL on MAPLE (Morphology Aligned Dataset with Paired Local Expression), a large-scale repository of over 720K paired histology patches with ST spots from diverse human tissue types.

We demonstrate the effectiveness and generalizability of SEAL finetuning recipe by deploying it on five pathology FMs: CONCH¹², H-Optimus-mini⁴¹, Phikon-v2⁹, UNI-v2-h⁵, and Virchow-v2⁷. In extensive benchmarking across 38 slide-level and 15 patch-level downstream tasks, SEAL vision-omics encoders consistently outperform their original non-finetuned counterparts on predicting across spatial scales such as slide-level molecular status, pathway activation, and morphological classes, as well as patch-level gene expression prediction. Furthermore, the SEAL-finetuned encoders show strong domain generalization on out-of-distribution expression prediction and gene-to-image retrieval, underscoring the benefits of augmenting existing FMs with complementary molecular information to enhance performance in spatial biology tasks.

Results

The main innovation of SEAL is to identify a molecular-guided finetuning recipe that is universally applicable to a range of existing Vision Transformer (ViT)-based⁴² pathology FMs of different model sizes, pre-training methods, and data distributions (**Figure 1A**). This addresses the critical gap not yet filled by the different families of multimodal pathology FMs on a combination of different spatial scales (patches and WSIs) and complementary modalities (language and omics)^{11, 12, 15–20}.

The utilization of existing pathology foundation models for SEAL is driven by the challenges present in curating large-scale training data of image patches and corresponding ST. Despite the concurrent efforts in aggregating and standardizing the publicly available slides and ST pairs^{22, 25, 38}, the image patches and ST pairs within each slide are relatively homogeneous due to non-negligible spatial autocorrelation⁴³, and thus cannot be treated as independent and identically distributed pairs as commonly done in vision-language datasets⁴⁴. Furthermore, with the paired pretraining dataset size not on the scale typically required for training the vision foundation models, the initialization of the vision encoder with weights from the existing pathology foundation models presents an appealing solution to data scarcity and spatial homogeneity. This approach is further corroborated by recent multimodal pathology foundation models^{12, 15, 17} demonstrating the success of the two-step approach of first pretraining the vision encoder only with histomorphology images and then subsequently finetuning with a complementary modality guidance.

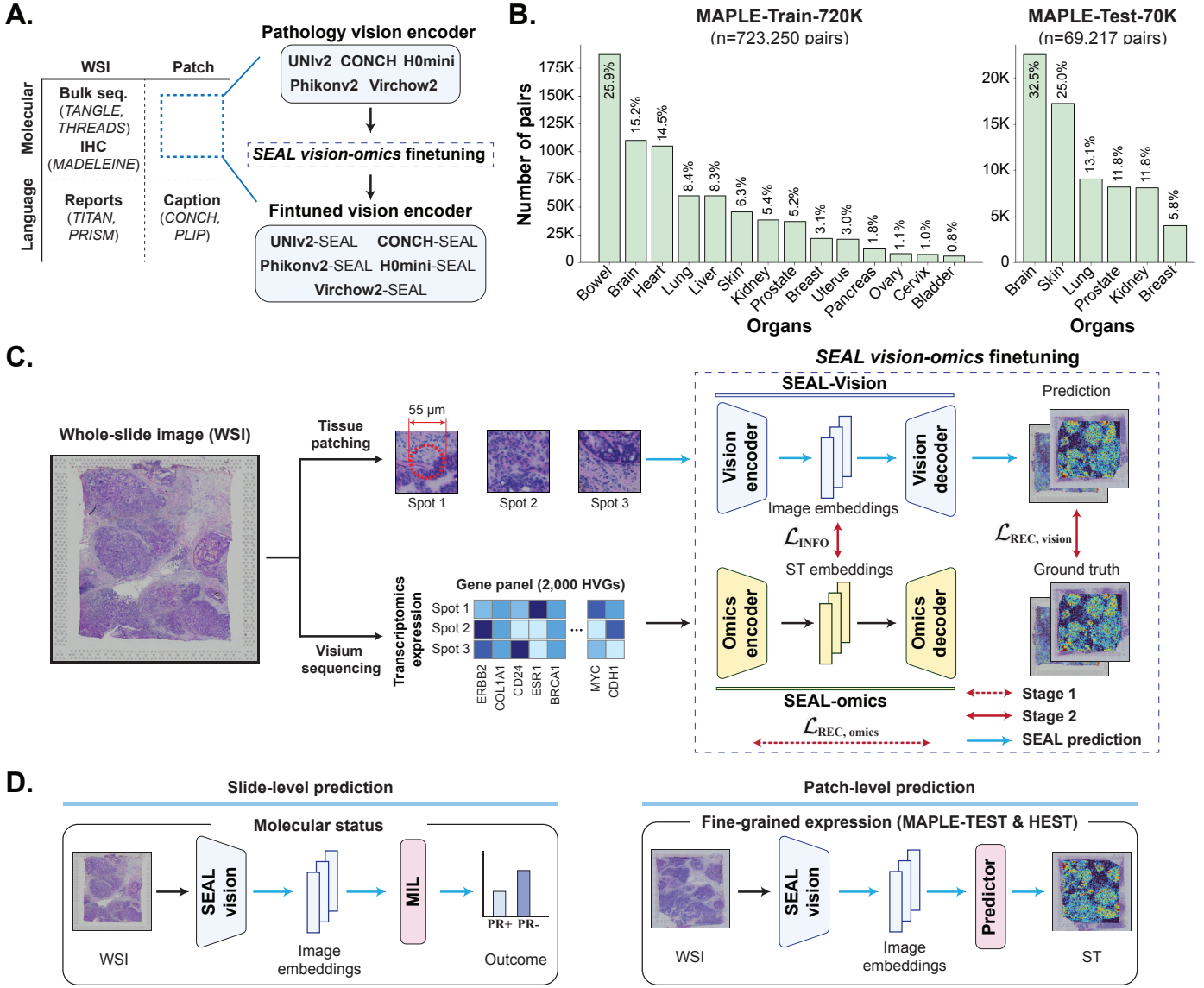


Figure 1: Overview of SEAL. **(A.)** Despite progress in multimodal foundation models for pathology, self-supervised learning using fine-grained vision–omics pretraining remains unexplored. SEAL closes this gap by applying *vision-omics* finetuning to pretrained patch encoders, yielding vision embeddings that better encode local molecular information. **(B.)** Distribution of histology image patches and corresponding spatial transcriptomics (ST) expression profiles in MAPLE-Train-720k and MAPLE-Test-70K, used for training and evaluating SEAL. MAPLE includes cancerous (42.8%), diseased (19.4%), healthy (32.2%), and treated (5.6%) samples. **(C.)** Overview of SEAL dual-pretraining strategy. First, an ST autoencoder is trained (SEAL-omics) on an auxiliary transcriptomics reconstruction task ($\mathcal{L}_{REC, omics}$). Second, the vision encoder (SEAL-vision), equipped with low-rank adapters, is trained to simultaneously align with the embedding space of SEAL-omics (\mathcal{L}_{INFO}) and reconstruct the original gene panel ($\mathcal{L}_{REC, vision}$). **(D.)** SEAL-vision can be applied to a range of downstream tasks, such as molecular outcome prediction from whole-slide images and gene expression prediction. ST: Spatial Transcriptomics, HVG: Highly variable genes.

We train and evaluate SEAL, on MAPLE (**M**orphology **A**ligned **D**ataset with **P**aired **L**ocal **E**xpression), a data repository of paired H&E morphology image patches (224×224 pixels) and corresponding Visium ST spots, each of which aggregates transcripts from multiple cells within $55\mu\text{m}$ diameter spots, comprised of HEST²⁵, public data²⁷, and internal data at Mass General Brigham (MGB) (**Figure 1B, Extended Data Tables 1 to 3**). The dataset is further divided into MAPLE-Train-720K (14 organs) for model development and MAPLE-Test-70K (six organs) for independent evaluation, stratified by patient cohort.

SEAL training proceeds in two stages (**Figure 1C**). In the first stage, we train a transcriptomic encoder-decoder using a variational autoencoder (VAE), with a scale-invariant loss that mitigates the effects of high sparsity and heterogeneous variance in gene expression profiles. This transcriptomics-only pretraining produces a stable molecular latent space that is amenable to subsequent alignment with tissue morphology³¹. In the second stage, we align the *transcriptomics* and *histomorphology* embeddings produced by the transcriptomic encoder and the pretrained vision encoder, respectively, using a contrastive loss that maximizes the joint similarity of matched pairs. We couple this with an image-to-gene reconstruction loss that enforces the prediction of transcriptomic profiles from image patches. To reuse pretrained weights and limit catastrophic forgetting, we apply low-rank adaptation (LoRA)⁴⁵ to a subset of the vision encoder. The SEAL-finetuned vision encoders can then be applied to downstream tasks (**Figure 1D**). Additional information on all training stages is provided in the **Online Methods, SEAL Pipeline** section.

Previous work on morphomolecular alignment with ST has largely focused on predicting gene expression from morphological image patches, with limited assessment of whether these models improve clinically relevant downstream tasks such as slide-level outcome prediction. These approaches typically follow two directions. First, the ST predictors are fitted on patch embeddings with a reconstruction objective^{28, 30, 46–49}. Second, retrieval-based methods^{29, 31, 33, 37, 50–52} employ contrastive loss to align between morphology and ST embedding space by finetuning either the vision or gene encoder. The retrieval-based ST prediction amounts to averaging the closest ST embeddings in the reference database to the query morphology embedding. We hypothesize that either of these approaches is limited in its ability to generalize to clinically-relevant and out-of-distribution tasks, which are predominantly at the slide-level, as we further show in ablation experiments. In contrast, SEAL employs a multi-objective loss function, which provides a direct signal that guides the vision encoder to learn features that are not just aligned (via $\mathcal{L}_{\text{INFO}}$), but also predictive of gene expression (via $\mathcal{L}_{\text{REC, vision}}$), resulting in aligned manifolds that can be leveraged for slide-level tasks.

SEAL improves slide-level downstream task performance

We first investigate whether SEAL models improve slide-level classification tasks over baseline pathology FMs. Specifically, we evaluate SEAL models on molecular status prediction (18 tasks), pathway expres-

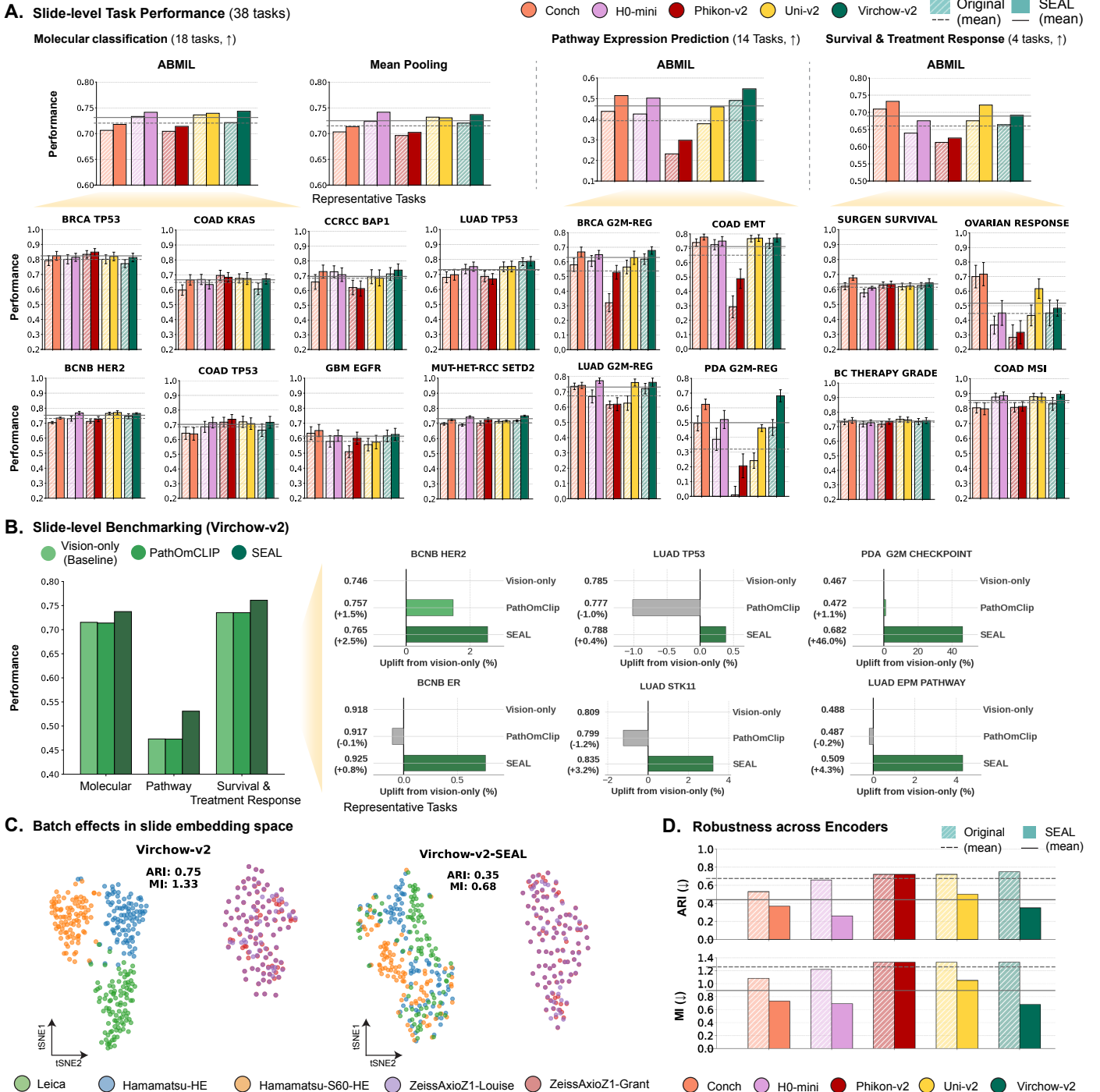


Figure 2: Overview of SEAL slide-level performance. (A.) Evaluation of five foundation models with and without SEAL on slide-level evaluations across 38 tasks covering molecular classification, pathway expression prediction, and marker and response prediction. The patch features from the baseline encoders and SEAL encoders are aggregated using attention-based multiple instance learning (ABMIL). (B.) Slide-level performance comparison between Virchow-v2 finetuned with the SEAL or PathOmCLIP recipes, along with non-finetuned Virchow-v2 (Baseline) on the full set of tasks with ABMIL aggregation: molecular status prediction, pathway expression, and survival & treatment response prediction tasks. (C.) t-SNE visualization comparing the robustness of Virchow-v2 and SEAL counterpart to the batch effects. Each slide was scanned with five different scanners, resulting in subtle differences in color, contrast, and resolution. Each dot represents the mean-pooled slide embedding for 100 identical slides captured using five commonly used WSI scanners. Stronger clusters indicate that the encoder is more prone to batch effects. (D.) ARI and MI scores across five baseline encoders and SEAL counterparts, using the same setup as (C). Lower ARI and MI correspond to weaker cluster formation. ARI: Adjusted Random Index, MI: Mutual Information.

sion (14 tasks), and marker & treatment response prediction tasks (4 tasks). The task categories were selected based on our hypothesis that molecular finetuning of the vision encoders would be beneficial for molecular outcome prediction or clinical tasks where complementary molecular information is critical.

We construct a slide-level embedding that serves as input to the slide-level predictor by aggregating (or pooling) the patch features extracted with the original or SEAL vision encoders. We use two widely-used approaches: attention-based pooling^{4,53,54} and mean pooling⁵⁵ to ensure SEAL is robust to different aggregation strategies. As for the vision encoders, we study five widely-used FMs for pathology, namely, CONCH¹², H0-mini⁴¹, Phikon-v2⁹, UNI-v2⁵, and Virchow-v2⁷. This choice covers multiple ViT sizes from *ViT-Base* (86M parameters, H0-mini & CONCH), to *ViT-Large* (307M parameters, Phikon-v2) and *ViT-Huge* (632M parameters, UNI-v2 and Virchow-v2), as well as multiple pretraining recipes: *vision-language alignment* in CONCH, *distillation* in H0-mini, and *DINOv2* in Phikon-v2, UNI-v2, Virchow-v2. Each encoder is finetuned with the same SEAL recipe with minor encoder-specific adaptations (**Extended Data Table 4**).

We observe that all five pathology FMs benefit from SEAL (**Figure 2A**). In molecular subtyping for gene mutation prediction tasks, we observe that, on average across encoders and all 18 tasks, the SEAL encoders achieve a 1.5% improvement compared to the vision-only models (**Extended Data Figure 2, 3, Extended Data Table 18-35**), with Virchow-v2-SEAL seeing the largest relative improvement (3.1%) and UNI-v2-SEAL seeing the smallest (0.6%) across molecular tasks. Notably, we also observe a minor improvement in performance on two immunohistochemistry (IHC) status prediction tasks (ER and PR status) on additional experiments run for Uni-v2 and Virchow-v2 (+0.3% and +1.0% respectively, **Extended Data Figure 1**). The same trends are observed with mean pooling, where we observe a 1.3% increase on average (**Extended Data Figure 2B**). We also compare Virchow-v2-SEAL with Virchow-v2 finetuned with PathOmCLIP recipe³⁰, which finetunes the vision encoder with ST to enhance patch-level gene expression performance (**Figure 2B**). The superior performance of Virchow-v2-SEAL on the slide-level tasks suggests that even with ST guidance, the finetuning recipes need to be carefully optimized to ensure improved performance across spatial scales. In summary, the consistent slide-level improvement, regardless of the aggregation approaches, underscores the benefit of integrating localized molecular signals for superior slide-level representation quality.

We further evaluate SEAL on morphological subtyping tasks to understand whether molecular finetuning can enhance performance for tasks where clinical outcomes are defined from morphological criteria. Specifically, we identify a set of challenging grading and subtyping tasks to compare the Virchow-v2 and UNI-v2 encoders and their SEAL-finetuned counterparts. We observe that SEAL mostly improves on slide-level morphological tasks as well, albeit by a smaller margin than the molecular slide-level tasks (**Extended Data Figure 1**). We conjecture that the vision-only DINOv2 pretraining on more than 100 million patches, employed by both Virchow-v2 and UNI-v2 (**Extended Data Table 5**), already yields strong morphological representa-

tions leading to saturated performance on morphology-oriented tasks, thus offering diminished benefit when finetuned with the 700k morphology-ST pairs.

Beyond predictive performance on slide-level endpoints, we investigate the robustness of SEAL representations to batch effects arising from variations in data acquisition, a persistent challenge in computational pathology⁵⁶⁻⁵⁹. To this end, we use the ICAIRD dataset⁶⁰ comprising 100 renal cell carcinoma slides digitized with five distinct scanners, which introduces non-biological domain shifts in color, contrast, and resolution (**Extended Data Figure 4A**). Visualizing the mean-pooled slide embeddings across different scanners reveals that the baseline FMs form more distinct clusters compared to SEAL embeddings from the same set of slides (**Figure 2C**). This suggests that SEAL is able to further suppress the visual artifacts and thereby batch effects with the multi-modal finetuning. This is in line with the previous findings on the superior robustness of the multi-modal pathology FMs over uni-modal pathology FMs⁶¹. Additionally, we measure the clustering tendency by scanner domain using the Adjusted Rand Index (ARI) and Mutual Information (MI), where a lower score indicates weaker cluster formation and would indicate higher robustness. SEAL achieves a significantly better ARI and MI for four encoders, except for Phikon-v2. On average, the ARI score drops from 0.67 to 0.44 and the MI from 1.25 to 0.9, indicating that SEAL embeddings are more robust to scanning artifacts (**Figure 2D, Extended Data Figure 4B**).

SEAL improves patch-level gene expression prediction performance

Encouraged by the performance uplift with SEAL on slide-level tasks, we next assess the quality of patch-level representations, which directly determines the quality of slide-level representations^{4,10,15,20}. Specifically, we focus on patch-level cross-modal gene expression prediction as a direct measure of morphomolecular representation quality, similar to the slide-level molecular tasks in previous analyses.

Comparison with vision-only models. SEAL-finetuned encoder is evaluated on two benchmarks for predicting highly variable genes (HVGs) from image patch embeddings, namely MAPLE-Test-70k (six organs) and HESTBench²⁵ (nine organs). Specifically, we fit a linear model on the frozen patch embedding (i.e., linear probe) to predict the expression levels of 10 HVGs (MAPLE-Test) and 50 HVGs for each organ (HESTBench). We use the Pearson correlation coefficient (PCC) to compare the true and predicted expression. Additional information on the linear probing can be found in the **Online Methods, Linear Probing** section.

When evaluated on MAPLE-Test, we observe a consistent and significant performance increase of SEAL-finetuned across all vision encoders in the six test organs: Brain, Breast, Kidney, Lung, Prostate, and Skin (Wilcoxon signed-rank test, $p < 0.001$, **Figure 3A**). Across the five encoders, Virchow-v2 showed the largest average performance gain (+17.3%), whereas H0-mini, the least improved model, still gained +7.3%

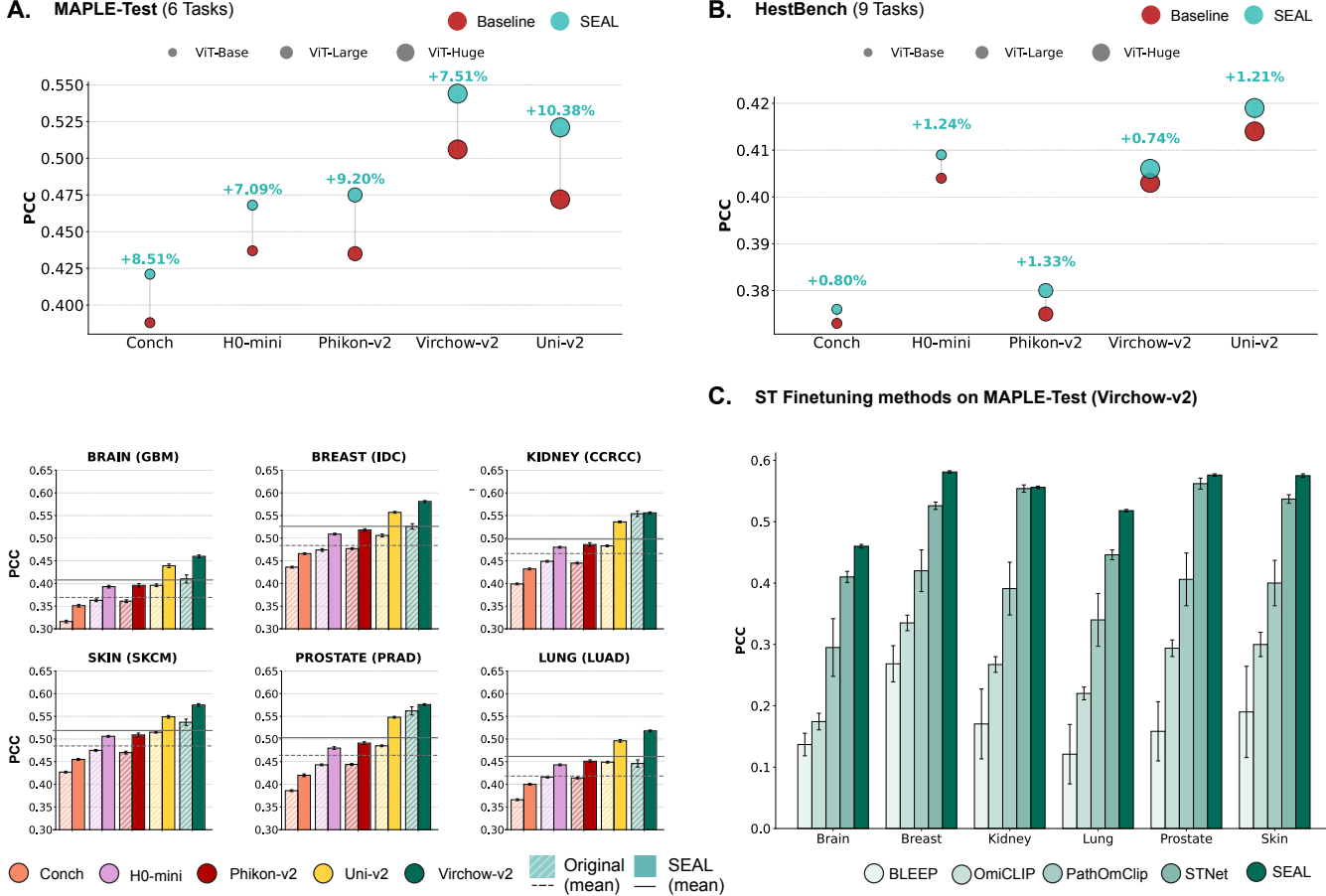


Figure 3: Overview of SEAL patch-level task performance. **(A.)** (top) Average patch-based ST prediction performance on MAPLE-Test dataset (6 organs) across five foundation models for pathology (Conch, H0-mini, Phikon-v2, Virchow-v2, Uni-v2), evaluated using Pearson correlation coefficient (PCC). The circle size indicates the relative number of trainable parameters in each model, from ViT-Base (86M parameters) to ViT-Huge (680M). (bottom) Organ-level predictive performance of five foundation models and their SEAL variants on the MAPLE-Test dataset (six organs). **(B.)** Average performance of five pathology foundation models on HEST-Bench (9 histology-to-gene expression tasks) and corresponding absolute improvements obtained with SEAL relative to the original models. **(C.)** Performance comparison between Virchow-v2 SEAL encoder and other widely-used histology-to-ST prediction baselines on MAPLE-Test. All baselines were also trained using the Virchow-v2 encoder, except OmiCLIP, which uses its corresponding encoder.

on average (**Extended Data Tables 7 to 12**). The same trend is observed when evaluated with mean squared error (MSE), where SEAL-finetuned encoders consistently lead to lower MSE (lower is better), with Virchow-v2 benefiting the most (11% lower MSE). Additional evaluation on the HESTBench further highlights the benefit of SEAL-finetuning (**Figure 3B, Extended Data Table 13**), where all five encoders improve overall performance (evaluated using PCC), with Phikon-v2 improving the most with the average of 1.33%. We attribute the lower performance gain on HESTBench to the significant distributional shift of this test benchmark compared to the SEAL data. While SEAL-Test assesses in-distribution generalization to holdout patients from the same source cohorts, HESTBench is composed of entirely separate study cohorts and ST technology (Xenium), thus representing a more challenging out-of-distribution task. Notably, the results also show improvements on some of the higher resolution Xenium tasks in this benchmark (IDC, PAAD, SKCM, COAD, LUAD) despite the absence of Xenium training data during finetuning, indicating SEAL’s potential to generalize beyond Vismium tasks. These results collectively demonstrate that even powerful pathology vision encoders can be further enhanced via simple finetuning with molecular guidance.

Comparison with ST prediction models. We further compare the predictive performance of SEAL against widely-used patch-level ST prediction methods (**Figure 3C**). Specifically, in addition to linear probing evaluation on embeddings from both SEAL-vision encoders and frozen original vision encoders (i.e., STNet⁴⁶), we implement BLEEP²⁹, OmiCLIP³³, and PathOmCLIP³⁰. For a fair comparison, we use Virchow-v2 as the vision encoder for all frameworks, except for OmiCLIP for which we use the original encoder. When evaluated on MAPLE-Test, we observe that the SEAL vision encoders lead to the highest performance, followed by linear probe on the original vision encoders (STNet). Interestingly, prediction-based approaches (SEAL, STNet, and PathOMCLIP) consistently provide better performance than the retrieval-based approaches (OmiCLIP and BLEEP). This implies that explicitly learning a predictive mapping of morphology to the gene expression is more generalizable and expressive than retrieving nearest “neighbors” from a reference dataset. The large gap is particularly surprising since some samples in the reference database used for retrieval are sourced from the same study cohorts as those in MAPLE-Train. The strong performance of STNet, a simple linear probe on the frozen pathology FM embeddings, underscores that fitting simple models on top of large and extensively trained vision encoders can outperform more complex finetuning frameworks. The lower performance of PathOmCLIP can be attributed to model overfitting induced by the reconstruction task, which may overwrite meaningful morphological features. This trend is consistent with our observations on slide-level prediction tasks for PathOmCLIP (**Figure 2B**). Meanwhile, the SEAL training paradigm outperforms all the ST finetuning baselines across all six test organs with an average PCC improvement of 2.4%, with expression prediction on kidney genes leading to the smallest (0.4%) and lung leading to the largest (16.1%) improvement compared to the next-best model. Additional information on the linear probing can be found in the **Online Methods, Stage III - Evaluation** section.

SEAL design considerations

We next investigate how different components of SEAL pretraining shape downstream performance, comparing the effect of multiple pretraining stages, finetuning strategy, sample efficiency, and reconstruction objective. The ablation analyses are performed on MAPLE-Test (patch-level) and BCNB cohort (slide-level) with Virchow-v2-SEAL and UNI-v2-SEAL.

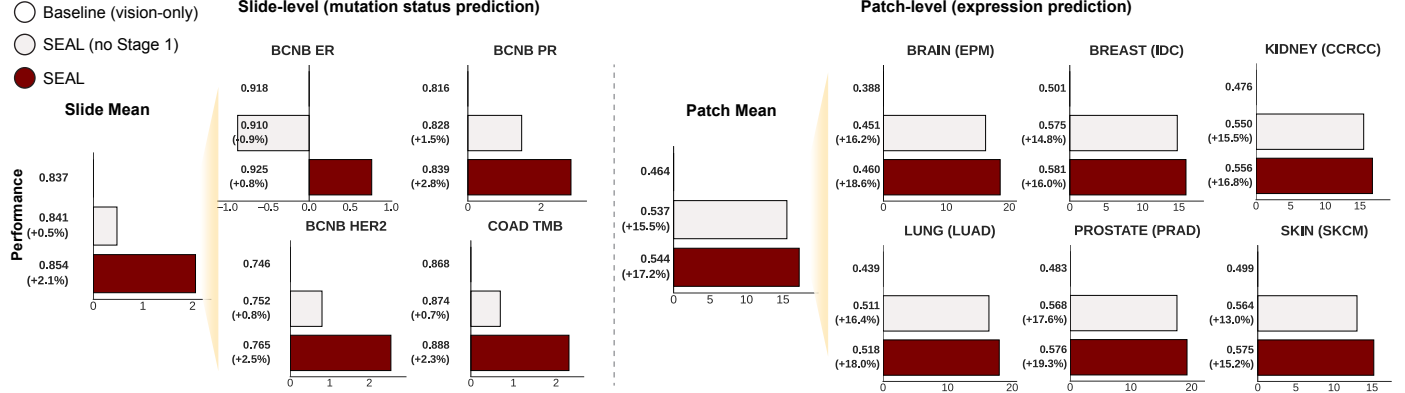
First, we assess SEAL without Stage 1 pretraining to isolate the contribution of first learning a structured transcriptomic embedding space before aligning it with the vision embeddings. We observe that omitting Stage 1 results in an average performance decrease of 1.48% at the patch level and 1.57% at the slide level (**Figure 4A**). This indicates that learning a structured embedding space for each modality prior to cross-modal alignment facilitates more effective coupling, highlighting the importance of Stage 1 in SEAL. These results are consistent with reports in vision–language models that emphasize the value of structured unimodal embeddings before alignment^{12,15}.

We further investigate the impact of the vision encoder finetuning recipe, replacing the parameter-efficient LoRA finetuning by full model finetuning (i.e., finetuning every parameter of the vision encoder). Our analysis shows the trade-off between optimization for the training task (patch-level prediction) and the preservation of general-purpose features for downstream slide-level tasks (**Figure 4B**). While full finetuning leads to marginally higher patch-level expression prediction performance (+0.5%), it also incurs a notable loss in the predictive performance for slide-level tasks (-1.2%). In contrast, the LoRA-based SEAL increases the slide-level task performance while achieving patch-level performance comparable with full finetuning. This demonstrates that SEAL can balance efficient adaptation of molecular information and preservation of the pretrained morphological features.

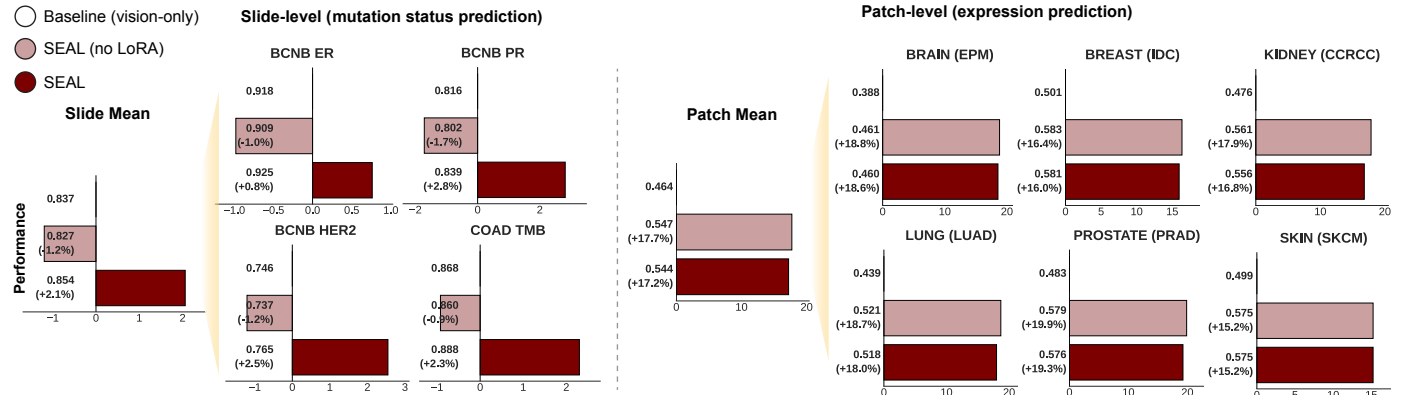
We additionally explore varying the portion of the MAPLE available for SEAL-finetuning. Specifically, we sample 0, 1, 10, and 100% of MAPLE-Train, ensuring equal organ distribution as the original, with 0% and 100% representing non-finetuned and SEAL-finetuned vision encoders. Based on the Virchow-v2 encoder, we observe the increasing performance trend as more ST data is available at both the patch-level and the slide-level tasks (**Figure 4C, Tables 14 and 15**), with the same trend observed for UNI-v2 encoder (**Tables 16 and 17**). This indicates the importance of having a large pretraining dataset, as previously established in foundation modeling literature^{5,15}.

We next conduct an ablation study to validate the design of the gene reconstruction objective introduced in SEAL. A primary challenge of ST data is its high sparsity and varying distribution across genes^{62,63}, which may persist even after normalization and preprocessing. Consequently, common regression objectives, such

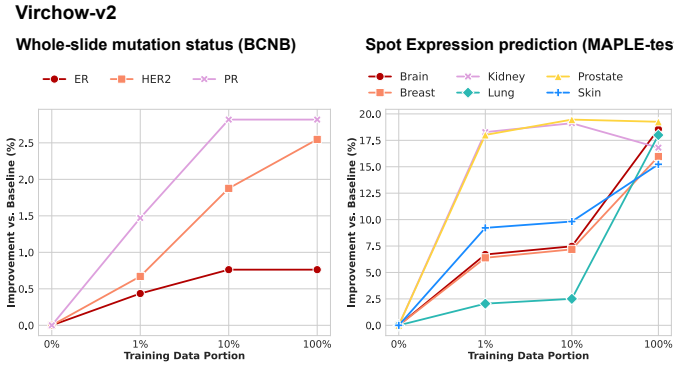
A. Stage 1 Pre-training



B. Full fine-tuning vs. Low-rank matrices



C. SEAL Sample efficiency



D. ST Reconstruction objective

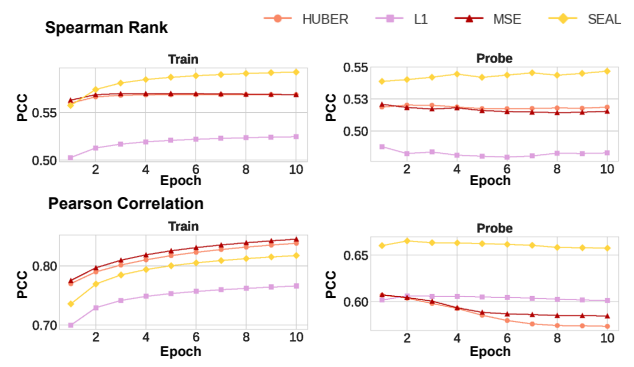


Figure 4: **Investigation of SEAL design considerations.** (A.) Effect of Stage I pretraining (joint pretraining of transcriptomics encoder and decoder) in Virchow-v2 with SEAL, showing a representative set of slide- and patch-level tasks. (B.) Effect of conducting full model finetuning compared to learning low-rank matrices (LoRA) in SEAL. (C.) Effect of data size on MAPLE-Test and the BCNB dataset. Different percentage of MAPLE-Train (0, 1, 10, and 100%) was used for SEAL-finetuning. The y-axis shows the percentage improvement relative to the probe of the vision-only Virchow-v2 embeddings. (D.) Effect of replacing SEAL reconstruction objective ($\mathcal{L}_{REC, vision}$) by a HUBER, L1, or MSE objective. Performance evaluated using Spearman rank and Pearson correlation coefficient.

as Mean Squared Error (MSE), L1, or Huber loss, become biased towards highly variable genes and may neglect genes with lower variance. The SEAL reconstruction objective introduces a scale-invariant loss term to address these challenges (**Online Methods, Stage I – Self-Supervised ST representations**). To validate this choice, we compared the performance of identical models trained with our objective against those trained using only Huber, L1, or MSE (**Figure 4D**). The SEAL objective achieves a higher and more stable Spearman rank and Pearson correlation on both validation sets throughout pre-training.

SEAL learns a representative morphology-omics embedding space

We next investigate the quality of the vision and omics embedding space alignment from SEAL-finetuning. While the strong performance on patch- and slide-level tasks suggests linear separability in some tasks, we seek to evaluate the encoder quality beyond linear probing. We therefore evaluate the cross-modal retrieval performance between localized morphology and transcriptomics by identifying the closest ST expression (or image patch) based on a query image patch (or ST expression). This setting, also referred to as zero-shot cross-modal inference^{11,12,44,64}, allows direct evaluation of the embedding space alignment without fitting an additional linear model. Additionally, it enables investigating the relationship between key pathways and morphological features.

First, we assess image-to-gene retrieval, where for each image patch query we retrieve the 50 nearest ST embeddings from the support (training) set and average them, following retrieval-based strategies^{29,33} (**Figure 5A**). For this analysis, we curate two in-house prostate cancer cohorts: a query cohort of 94,142 Visium spots (eight patients, 20 histological images) and a support cohort of 31,192 Visium spots (six patients, eight histological images). The two cohorts were processed at distinct sequencing cores, leading to visible staining differences due to divergent tissue processing protocols (**Figure 5B**) and introducing additional batch effects. Retrieval performance is quantified with PCC across progressively larger HVG panels.

The comparison of SEAL retrieval against other retrieval-based approaches, namely OmiCLIP and BLEEP, reveals several insights (**Figure 5C**). Specifically, SEAL on average, achieves a 3.1x higher PCC compared to OmiCLIP across gene sets, which highlights the importance of a domain-specific vision encoder, as OmiCLIP omits both vision-only pretraining on histopathology slides and uses a general-purpose language model to encode highly expressed genes. Additionally, BLEEP performance is substantially worse even with the same vision encoder (Virchow2) as SEAL (SEAL: 0.146 vs. BLEEP: 0.003 for *All* genes). This suggests that SEAL finetuning, which adds an additional ST reconstruction objective on top of the contrastive objective, creates a joint embedding space that is more robust to batch effects arising from different tissue processing protocols for the query and support sets. In addition, the SEAL decoder performs better than SEAL-retrieval in a zero-shot setting. This suggests that retrieval-based approaches are less effective for ST

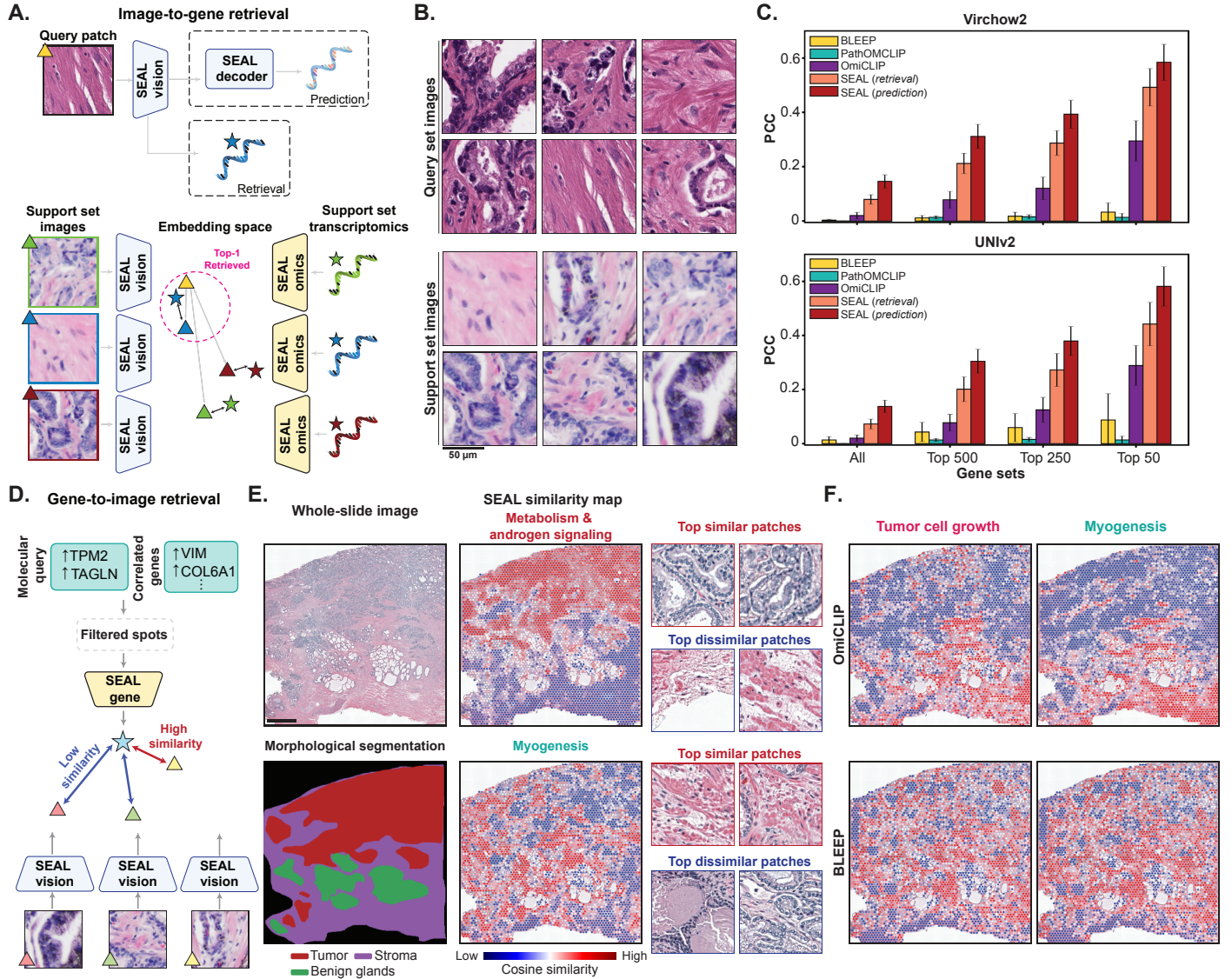


Figure 5: Cross-modal retrieval with SEAL. SEAL can perform cross-modal retrieval (image-to-gene, gene-to-image) leveraging the aligned vision and gene expression embedding space. **(A.)** Schematic overview of image-to-gene retrieval with SEAL. Given a query image, we retrieve the K -nearest images from the support (training) set and average their corresponding transcriptomic embedding to become the predicted expression. For comparison, the direct image-to-gene predictive performance using the SEAL decoder is also shown. **(B.)** Examples of the training (support) and test (query) set from internal prostate cancer samples. The data was split based on two separate cohorts that exhibit clear visual differences, representing an out-of-distribution prediction task. **(C.)** Retrieval performance of SEAL and baselines evaluated with PCC. All models use the same Virchow-v2 as the initial patch encoder, except for OmiCLIP with its own pretrained weights. For SEAL, we evaluate both retrieval (taking the k -nearest image embeddings and averaging the corresponding gene expression) and direct prediction (SEAL decoder). **(D.)** A schematic of gene-to-image retrieval with SEAL. Given a gene or pathway of interest, a molecular query is formulated where important genes are highly expressed, while average expression is used for all other genes. The molecular query embedding is obtained using the SEAL-omics encoder, and the cosine similarity with image patches across the slide of interest is calculated. **(E.)** Example of gene-to-image retrieval with SEAL in prostate cancer. We build a custom query with a set of genes from the *metabolism & androgen signaling* and *myogenesis* pathways. The cosine similarity map illustrates the similarity of each image patch to the query, with red (blue) indicating high (low) similarity. **(F.)** The cosine similarity map for two different molecular queries (*Tumor cell growth* and *Myogenesis* pathways) using BLEEP and OmiCLIP. PCC: Pearson Correlation Coefficient. The scale bar is 1 mm unless specified otherwise.

prediction as the performance solely depends on the quality of the learned embedding space, as also previously observed (**Figure 3C**). These observations are replicated with UNI-v2 encoder, highlighting the robustness of cross-modal alignment for SEAL.

Building on the strong image-to-gene retrieval performance of SEAL, we next examine gene-to-image retrieval (**Figure 5D**). While image-to-gene retrieval can be framed as a standard ST prediction task and quantified with PCC, there is no analogous, well-defined notion of “predicting” images from ST, making gene-to-image retrieval harder to evaluate quantitatively. Instead, our goal is to qualitatively inspect which morphological patterns or WSI regions are most strongly retrieved (i.e., activated) by a given molecular query. To provide more interpretable and functionally meaningful queries than single-spot gene expression, we construct customized transcriptomic queries derived from sets of highly expressed genes associated with specific pathway activation⁶⁵ (**Online Methods, Stage III – Evaluation (Retrieval)** section).

For a prostate cancer slide from MAPLE-Test, annotated with three different morphological classes (tumor, stroma, and benign glands), we construct SEAL similarity map by visualizing the cosine similarity between the transcriptomics query and all image patch embeddings (**Figure 5E**). Based on the WSI visualization and examples of top similar patches, we observe that for *androgen signaling* and *myogenesis* function-related transcriptomics queries, the tumoral and stromal regions are most activated (red), consistent with the literature^{65–67}. In contrast, the top dissimilar patches show the opposite trend, with stromal and adipose/tumoral patterns, respectively.

Finally, we performed a qualitative comparison of SEAL-finetuned Virchow-v2 with BLEEP and OmiCLIP by visualizing the pathway activations for the same prostate cancer sample (**Figure 5F**). We observe that, despite the functionally opposite nature of the *tumor cell growth* and *myogenesis* pathways, which are expected to show more activation in tumor and stromal regions, respectively, almost identical regions are activated for both BLEEP and OmiCLIP. This again suggests that the less structured vision-omics embedding spaces for these approaches do not exhibit natural morphomolecular properties, in contrast to that of SEAL.

Discussion

We introduce Spatial Expression-Aligned Learning (SEAL), a vision-omics self-supervised learning framework, which shows that the localized morphomolecular information from paired spatial transcriptomics (ST) and hematoxylin and eosin (H&E) image patches can enhance existing pathology vision foundation models (FMs) for a wide range of downstream tasks. Given any state-of-the-art FMs for pathology, SEAL infuses localized transcriptomics expression information through a sample-efficient finetuning process that simultaneously aligns image and ST embeddings and predicts ST expression profiles from image embeddings (**Figure 1**).

SEAL encoders, finetuned on a large pretraining cohort that combines public and in-house ST-morphology pairs, lead to significantly improved performance over their non-finetuned counterparts, as evaluated across diverse organs with 38 slide-level molecular and morphological outcome prediction tasks (**Figure 2**) and 15 patch-level ST prediction tasks (**Figure 3**). SEAL finetuning is agnostic to the vision encoder, with consistent results obtained over five popular FMs of different sizes and pretraining data distributions, thereby presenting a highly data- and parameter-efficient finetuning method (**Figure 4**). As an added benefit, the multi-modal finetuning renders the SEAL embeddings more robust to batch effects. Moreover, SEAL-finetuning establishes a geometrically more meaningful joint embedding space compared to other contrastive alignment approaches, as shown by the superior cross-modal retrieval performance of SEAL and more interpretable gene-to-image pathway analysis (**Figure 5**).

Our design choices distinguish SEAL from prior multimodal alignment paradigms in three ways. First, we introduce a robust transcriptomics encoder on a fixed-size gene panel prior to the cross-modal alignment. We introduce a scale-invariant reconstruction objective to pretrain a variational autoencoder which balances absolute error with gene-level correlations. This encoder design explicitly handles the high dimensionality, sparsity, and noise of ST data by using normalizing flows to create a more expressive latent model, allowing it to capture complex data distributions and filter measurement noise (**Online Methods – Stage I**). Second, we employ Low-Rank Adaptation (LoRA) matrices to finetune the vision encoders. LoRA not only provides parameter efficiency but also prevents catastrophic forgetting of the rich prior information of the vision encoders, which we observed with regular finetuning. This allows the model to preserve the morphological information while additionally integrating transcriptomic signals (**Online Methods – Stage II**). Third, SEAL uses a multi-objective training framework to ensure that the resulting vision-omics embeddings are both aligned with one another and directly predictive of gene expression.

In this sense, SEAL molecular alignment of a pathology FM is conceptually analogous to post-training alignment in large language models. By exposing vision encoders to localized transcriptomic supervision, SEAL reshapes the joint embedding space so that clinically relevant morphomolecular patterns become easier to retrieve across diseases. This suggests that the training of foundation models for pathology should not remain purely vision-only. We envision molecular alignment to be adopted as a systematic post-training stage, applied not only to public resources but also scaled with proprietary ST collections wherever available. A notable consequence of this alignment is that generalizable gains in downstream performance and robustness arise as emergent properties of the training objective, rather than from task-specific finetuning.

Despite the strong performance of the SEAL models, several limitations remain. While we demonstrate SEAL’s efficacy on a selection of five major pathology FMs, this does not cover all publicly available models. SEAL is finetuned using Visium data, which captures expression at a spot resolution with multiple cells, rather

than at single-cell resolution. However, we anticipate that the same finetuning principles are transferable to technologies such as Xenium or VisiumHD, as indicated by the moderate performance improvements on the HESTBench Xenium tasks. With the increasing availability of higher-resolution ST, we expect that applying SEAL can unlock more granular insights into cell-level morphomolecular links. Finally, we use a variational autoencoder with an MLP structure for the transcriptomics encoder to handle relatively small pretraining datasets, instead of heavier transcriptomics FMs trained predominantly on single cells^{68,69}. Community-driven efforts on curating larger-scale pretraining datasets^{22,25,38} will allow SEAL to leverage both pathology and transcriptomics FMs in the near future.

In conclusion, the robustness of SEAL across different model architectures, sizes, and pretraining strategies suggests that ST-guided finetuning is a generalized capability rather than a dataset-specific effect. Furthermore, SEAL establishes a scalable and parameter-efficient paradigm for the next chapter of vision-omics multimodal FM development in computational pathology. We anticipate that this work can be leveraged in further multimodal settings to build multi-scale representations of human tissue and disease.

Online Methods

Datasets & Processing

Training Data. Our training data, MAPLE-Train, consists of $N = 723,250$ spot-image pairs stemming from 353 human diseased (64.2%), healthy (30.3%), and treated (5.5%) patient samples across 14 organs (detailed splits and study sources can be found in **Extended Data Table 1- 3**). This corresponds to the majority of human Visium (98.4%) and Visium HD (1.6%) samples from the Hest-1k dataset²⁵, preprocessed to align ST gene panels and normalize cross-slide effects (see **Transcriptomics Data Processing**). We removed the STv1 samples from this dataset to ensure a maximum spot size of $55\mu\text{m}$, which STv1 exceeds. To prevent data leakage across the training, validation, and holdout test sets, we split the data by patient, as some patients may have multiple samples, using a 80-10-10 split. To ensure proportional representation across disease and organ types, we use a stratified sampling strategy by organ and select only Visium samples for MAPLE-Test due to the limited availability of Visium HD slides. For ST expression prediction tasks, we report two sets of results. First, MAPLE-Test evaluates prediction performance on the top 10 highly variable genes (HVGs) by organ for Brain, Breast, Kidney, Lung, Prostate, and Skin samples in the holdout set, based on variance in MAPLE-Train. Second, we evaluate the prediction performance of the top 50 HVGs on five tissue types of Visium (PRAD, READ, ccRCC, Lymph IDC) and Xenium (LUNG, IDC, PAAD, SKCM, COAD) from additional samples that were held out from MAPLE-train and test set, in line with the Hest Benchmark²⁵. These evaluations represent in-distribution (MAPLE) and out-of-distribution (HestBench) patch-level expression prediction tasks.

Image Data Processing. All Whole Slide Images (WSIs) were first processed using a finetuned feature pyramidal network (FPN) for tissue segmentation. Only patches overlapping with the resulting tissue masks were used for subsequent steps. We utilized the HestCore library to extract $224 \times 224\text{px}$ patches at multiple resolutions (0.25, 0.5, and $1.0\mu\text{m}$ per pixel) where the centroid of the patch matches the centroid of the ST spot. Since the tissue samples may exceed the capture area of some ST assays, such as Visium, we select the intersection of patches that can be matched to a spot and barcode the location of all patches such that their relative position can be retrieved and matched to the transcripts. All training samples are normalized across each color channel c $\text{pixel}_c(x, y) = \frac{\text{input}_c(x, y) - \mu_c}{\sigma_c}$ for channel-mean μ_c and standard deviation σ_c at pixel position (x, y) . We used the same means and standard deviations as were used during the training of the respective patch foundation models (UNI-v2-h, CONCH, Virchow-v2, etc.). During training, we randomly sample a magnification for each barcode and apply multiple augmentations to the image, including horizontal ($p=0.5$) and vertical flips, RGB shifts, color jittering effects, greyscaling, and a Gaussian blur, all applied at varying probabilities (see **Extended Data Table 6**).

Transcriptomics Data Processing. We process the transcriptomics samples by filtering and aligning their gene panels. This includes filtering blank, control, and ambiguous transcripts as denoted in the sample metadata. As the gene naming convention was not standardized across samples, we harmonized all samples annotated with Ensembl IDs to HGNC nomenclature using PyBiomart annotations⁷⁰. We implemented a greedy selection algorithm to select the set of transcriptomics samples with a high degree of gene panel overlap, dropping any samples that do not match a minimum of 5,000 genes from a reference set of genes, which led to the exclusion of four samples. The resulting samples have an aligned set of $G = 14,581$ genes for all spots. To reduce sparsity, we filter out genes that are only expressed in <10% of spots as well as empty spots that contain no gene counts. We further normalize each spot i by total counts over all genes j , such that each spot has the same total count after normalization, to reduce variability related to data capture artifacts like varying sequencing depths across samples, using $\mathbf{x}_{ij}^{(g, \text{norm})} = \frac{\mathbf{x}_{ij}^{(g)}}{\sum_j^G \mathbf{x}_{ij}^{(g)}} \times 1e^{-4}$. We apply a log1p transform to reduce data heteroscedasticity commonly seen in count data using $\mathbf{X}^{(g)} = \log(\mathbf{X}^{(g)} + 1)$ where $\mathbf{X}^{(g)} = \left(\mathbf{x}_i^{(g, \text{norm})}\right)_{i=1}^N \in \mathbb{R}^{N \times G}$. For training, we set $G = 2,000$ by selecting the most variable genes using the Seurat V3 method⁷¹ that bins genes by average expression and selects genes which standardized variance significantly exceeds the expected variance. We supplemented the HVG gene panel with 584 Tier 1 genes from the Catalogue of Somatic Mutations in Cancer (COSMIC)⁷² gene census to guarantee the inclusion of known marker genes.

Local Smoothing. Given that ST assays can produce sparse and noisy data due to variable sequencing coverage, we apply local smoothing to make the expression signal more distinguishable from measurement noise. Concretely, for each center spot $\mathbf{x}_{r,c}^{(g)}$ and its spatial coordinates (r, c) , we first identified its set of immediate neighbors on Visium hexagonal spot lattice, $N(r, c)$. We then computed the mean expression of this neighborhood, $\mathbf{x}_{\text{context}}^{(g)} = \frac{1}{N_{\text{adj}}} \sum_{(r', c') \in N(r, c)} \mathbf{x}_{r', c'}^{(g)}$ where $N_{\text{adj}} = |N(r, c)|$ is the number of valid, tissue-containing neighbors, which may be less than 6 spots on the tissue edges. The final smoothed expression value, $\mathbf{x}_i^{(g)}$, is the average of the center spot and its context mean $\mathbf{x}_i^{(g)} = \frac{\mathbf{x}_{r,c}^{(g)} + \mathbf{x}_{\text{context}}^{(g)}}{2}$, where $i = m(r, c)$ is the unique spot index derived from the spot barcode. For computational efficiency, this six-neighbor adjacency graph was pre-calculated for all spots in each sample, allowing computation of $\mathbf{x}_{\text{context}}^{(g)}$ in a single vectorized operation.

SEAL Architecture

The primary objective of SEAL is to finetune patch-level pathology foundation models with spatially resolved molecular information. To do this, SEAL has two main components: 1) a self-supervised **gene model** $g(\cdot)$ that is learning denoised lower-dimensional embeddings $\mathbf{z}_i^{(g)} \in \mathbb{R}^{d_i}$ from the high-dimensional gene inputs $\mathbf{x}_i^{(g)} \in \mathbb{R}^G$; and 2) the patch-level **image model** $f(\cdot)$ that we finetune using low-rank adaptation matrices (LoRA)⁴⁵, which is encoding each histology patch $\mathbf{x}_i^{(p)} \in \mathbb{R}^{224 \times 224 \times 3}$ into a 1D embedding $\mathbf{z}_i^{(p)} \in \mathbb{R}^{d_i}$. SEAL uses a two-stage training procedure. **Stage I** is a warmup period for the gene encoder $g(\cdot)$ and is exclusively

trained on a gene reconstruction task. **Stage II** concurrently finetunes the patch encoder $f(\cdot)$ by aligning the gene and image embeddings $\mathbf{z}_i^{(p)}$ and $\mathbf{z}_i^{(g)}$ for each spot-image pair, while retaining the Stage I objective as an auxiliary task to continue improving the quality of the gene embeddings during contrastive alignment.

SEAL-omics. We implement a variational autoencoder (VAE) as our gene model, which consists of an encoder $g(\cdot)_{enc,\phi}$ and a decoder $g(\cdot)_{dec,\phi}$, both parameterized by ϕ . The encoder $g(\cdot)_{enc,\phi}$ is a feedforward network that maps our high-dimensional input gene panel $\mathbf{x}_i^{(g)} \in \mathbb{R}^G$ to the parameters of a latent Gaussian distribution, whilst ensuring that the latent embedding $\mathbf{z}_i^{(g)}$ matches the image embedding dimension d_i . During the forward pass, $\mathbf{x}_i^{(g)}$ is transformed through several linear and batch normalization layers with ReLU activations to yield an intermediate representation $\mathbf{h}_i \in \mathbb{R}^{d_i}$. Instead of using \mathbf{h} as is, we linearly project it to the parameters of a Gaussian distribution $\mu_i = W_\mu \mathbf{h}_i$, the standard deviation $\sigma = \exp(\frac{1}{2} \log(W_\sigma \mathbf{h}_i))$ and sample $\epsilon \sim \mathcal{N}(0, 1)$, known as the local reparameterization trick⁷³. Given these projections and the stochastic error, we compute our final latent representation $\mathbf{z}_i^{(g)} = \mu_i + \sigma_i \circ \epsilon$. The linear projections in this reparameterization trick are used to enable backpropagation in the stochastic sampling process, and we posit that modeling the latent variables with a distribution may help the model to distinguish the true signal from measurement noise, such as the sparsity mentioned in the previous section. The decoder $g(\cdot)_{dec,\phi}$, which mirrors the encoder’s feedforward architecture, reconstructs the original gene panel $\hat{\mathbf{y}}_i^{(g)} = g(\mathbf{z}_i^{(g)})_{dec,\phi}$ from the latent embedding. The VAE is trained by optimizing the Evidence Lower Bound, which consists of a Kullback-Leibler (KL) divergence loss to regularize the latent space and the reconstruction loss $\mathcal{L}_{rec,i}(\mathbf{x}_i^{(g)}, \hat{\mathbf{y}}_i^{(g)})$, further specified in the section on training **Stage I**.

SEAL-vision. We design SEAL to be a general-purpose finetuning recipe that should work well across image encoders. Therefore, we implement several common benchmarks used in computational pathology, namely ResNet50 with the original torchvision weights⁷⁴, the vision encoder of CONCH¹², a patch-level contrastively trained vision-language model (ViT-Base with 16×16 px image tokens, 12 core layers, 90M parameters), H-optimus-mini⁴¹, a distilled version of Hoptimus-0⁸ (ViT-Base with 14×14 px image tokens, 12 core layers, 86M parameters), Phikon-v2⁹, a Dinov2-trained foundation model (ViT-Large with 16×16 px image tokens), UNI-v2-h⁵, a patch-level foundation model trained at fixed magnification (ViT-Huge with 14×14 px image tokens, 32 core layers, 681M parameters), and Virchow-v2⁷, a large patch-level model trained on mixed magnification (ViT-Huge with 16×16 px image tokens, 32 core layers, 632M parameters). Further information about each encoder tested can be found in **Extended Data Table 5**. For each encoder $f(x)_\theta$, we fit LoRA adapters (see next section) on a variable number of core layers (specified in **Extended Data Table 4**) and attention heads for finetuning in **Stage II**. Given the input patch $\mathbf{x}_i^{(p)}$, the image encoder produces a latent representation $\mathbf{z}_i^{(p)} = f(\mathbf{x}_i^{(p)})_\theta \in \mathbb{R}^{d_i}$. During training, this is used to train the alignment objective with the gene embedding $\mathbf{z}_i^{(p)} \leftrightarrow \mathbf{z}_i^{(g)}$, which is further specified the section on **Stage II**. For inference and evaluation, we train a lightweight task model $t(\cdot)_\gamma$ with a limited amount of parameters γ , such as a linear probe or attention-

based multiple instance learning for different patch- and slide-level tasks, further detailed in section on **Stage III**.

Low-Rank Adapters. Directly finetuning all parameters of ViT backbones is both computationally expensive and risks catastrophic forgetting, a phenomenon where the model overwrites its biologically salient, pre-trained morphological knowledge. To circumvent this, we employ Low-Rank Adaptation (LoRA) as a parameter-efficient finetuning technique. The LoRA hypothesis posits that the change in weights during model adaptation (ΔW) has a low intrinsic rank, meaning that the essential information required to adapt the model can be effectively compressed using a much smaller number of parameters than the full weight matrix. Therefore, we approximate the weight update using a low-rank decomposition. For a given pre-trained weight matrix $W_0 \in \mathbb{R}^{d \times k}$, the update ΔW_0 can be represented by two smaller, trainable matrices, $B \in \mathbb{R}^{d \times r}$ and $A \in \mathbb{R}^{r \times k}$, where the rank $r \ll \min(d, k)$. During training, the original weights are frozen and only A and B are updated. The modified forward pass for the layer then becomes $h = W_0x + \Delta Wx = W_0x + (\frac{\alpha}{r})BAx$. For SEAL, we use a rank of $r = 8$ and alpha $\alpha = 8$ (**Extended Data Table 4**).

SEAL Pipeline

Stage I – Self-supervised ST Representations. One main challenge in finetuning vision encoders with spatial transcriptomics information is to learn meaningful and generalizable embeddings $z_i^{(g)}$ for each transcriptomics spot i that account for common challenges with ST data such as their high dimensionality, highly unequal variance, data sparsity, noise, as well as local and global expression context. High dimensionality, data sparsity, and local context are partially handled through gene selection and local smoothing in the preprocessing pipeline (detailed in the section on **Datasets & Processing**). To handle noisy data, we use a VAE, which has shown effective denoising properties on ST data⁷⁵.

We iterate on the standard **VAE architecture**⁷³, which typically assumes an approximate diagonal Gaussian posterior over the latent variables. While this assumption makes optimization tractable, it restricts the posterior to simple shapes. For ST dat, this can represent a limitation, as gene expression distributions are often sparse, skewed, and governed by non-linear dependencies between genes^{71,75}. To address this, we augment the VAE with planar normalizing flows. After sampling the initial latent variable

$$z_0 = \mu + \sigma \odot \epsilon, \quad \epsilon \sim \mathcal{N}(0, I), \quad (1)$$

we iterative apply a set of learnable and invertible transformations of the form

$$z' = z + \mathbf{u} \tanh(\mathbf{w}^\top z + b), \quad (2)$$

where $\mathbf{u}, \mathbf{w} \in \mathbb{R}^d$ and $b \in \mathbb{R}$ are trainable parameters.

Intuitively, each planar flow performs a smooth and non-linear transform of the latent space along a learned direction⁷⁶. Starting from the simple initial Gaussian sample (Equation 1), successive flow steps (Equation 2) warp the latent distribution, allowing it to approximate more complex geometries. Since each flow step reshapes the latent space, we adjust the probability density using a density correcting term accordingly to ensure that the transformed posterior remains a properly normalized distribution.

Beyond the model architecture, we require a robust **training objective** to learn spot-level representations that: 1) is highly correlated with the ground truth gene panel; and 2) ensure a high-fidelity reconstruction on the initial panel $\hat{\mathbf{y}}_i^{(g)} = g(\mathbf{z}_i^{(g)})_{dec, \phi}$. Some prior works use regression-based reconstruction objectives, such as Mean Squared Error or Huber loss to evaluate the reconstruction^{29,30}, given by Equation 3 as

$$\mathcal{L}_{mse} = \frac{1}{G} \sum_{i=1}^G (\mathbf{x}_i^{(g)} - \hat{\mathbf{y}}_i^{(g)})^2. \quad (3)$$

However, since the gene panel has a strong unequal variance, also after the count-normalization and log1p transforms, we found that objectives exclusively correcting for absolute error over-emphasize highly variable genes and neglect genes with lower variance, leading to a biased training objective. To account for lower variance genes, we introduce an additional loss term that is scale-invariant by repurposing the original Barlow Twins loss⁷⁷. While this loss was originally introduced as an alignment loss between an original and a distorted view of the same data, we found this to work well as a scale-invariant reconstruction loss, which consists of two main components. First, we calculate the gene-level cross-correlation along the batch dimension for each predicted gene in the batch $(\hat{\mathbf{y}}_{b,i}^{(g)})_{b=1}^B$ and its ground truth counterpart $(\mathbf{x}_{b,i}^{(g)})_{b=1}^B$.

$$C_{ij} = \frac{\sum_b \mathbf{x}_{b,i}^{(g)} \hat{\mathbf{y}}_{b,j}^{(g)}}{\sqrt{\sum_b (\mathbf{x}_{b,i}^{(g)})^2} \sqrt{\sum_b (\hat{\mathbf{y}}_{b,j}^{(g)})^2}}. \quad (4)$$

Given the cross-correlation matrix for the training batch, we maximize the element-wise correlation between each predicted gene and the ground truth, which corresponds to the Barlow Twins invariance term

(Equations (4) and (5)), which in our context means that the reconstructed gene panel is invariant to a uniform scaling of the gene expressions. As such, this objective ignores absolute magnitude and is therefore robust to the unequal variance across genes. Second, we minimize the correlation between unpaired genes, meaning that high values on the off-diagonal of C that correspond to redundant information are penalized (Equation 6). In our context, this prevents the VAE from trivially grouping together highly correlated genes which may ignore subtle differences. However, since many genes' expressions may be correlated for legitimate reasons, we apply a lower weighting λ_1 to this penalty (Equation 7).

$$\mathcal{L}_{inv} = \sum_i^G (1 - C_{ii})^2 \quad (5)$$

$$\mathcal{L}_{red} = \sum_i^G \sum_{j \neq i} C_{ij}^2. \quad (6)$$

The final loss is a weighted sum between our three main loss components, balancing the penalty between the correlation-based losses \mathcal{L}_{inv} and \mathcal{L}_{red} that are unbiased and invariant to the magnitude of the predictions, and \mathcal{L}_{mse} that accounts for the magnitude of the predictions.

$$\mathcal{L}_{rec} = \lambda_0 \mathcal{L}_{inv} + \lambda_1 \mathcal{L}_{red} + \lambda_2 \mathcal{L}_{mse} \quad (7)$$

We train the spot-level VAE with a batch size of 384 for a maximum of 3 epochs as a warm-up period with Adaptive Moment Estimation (Adam⁷⁸) as a stochastic optimizer using a learning rate of 0.0005, which is updated using a cosine annealing learning rate schedule. The full list of hyperparameters in the final models can be found in **Extended Data Table 4**.

Stage II - Contrastive Alignment. Following warm-up period for the VAE $g(\cdot)_\phi$, we start the finetuning of the image encoder $f(\cdot)_\theta$. After loading in its pre-trained weights, we unfreeze the final \mathbf{X} blocks of the encoder. We then align the image embeddings $\mathbf{z}^{(p)}$ and gene embeddings $\mathbf{z}^{(g)}$ using an InfoNCE loss, which maximizes their joint likelihood. Given a set of $N \times N$ samples in each training batch, we maximise the joint likelihood of each pair while minimizing the likelihood of negative pairs (non-matching H&E-ST pairs) in the batch:

$$\mathcal{L}_{InfoNCE} = -\frac{1}{N} \sum_{i=1}^N \left[\log \frac{\exp \left(\langle \mathbf{z}_i^{(p)}, \mathbf{z}_i^{(g)} \rangle / \tau \right)}{\sum_{k=1}^N \exp \left(\langle \mathbf{z}_i^{(p)}, \mathbf{z}_k^{(g)} \rangle / \tau \right)} + \log \frac{\exp \left(\langle \mathbf{z}_i^{(p)}, \mathbf{z}_i^{(g)} \rangle / \tau \right)}{\sum_{k=1}^N \exp \left(\langle \mathbf{z}_k^{(p)}, \mathbf{z}_i^{(g)} \rangle / \tau \right)} \right], \quad (8)$$

where $\langle \cdot \rangle$ is the cosine similarity between embeddings, and τ is the temperature of the softmax. Intuitively, this loss forces matching embeddings to be close together with respect to their cosine similarity while pushing non-matching pairs apart such that we learn a joint embedding space, where each image patch is aligned with

its corresponding gene profile, while mismatching pairs are easily distinguishable. Relevant hyperparameters for the contrastive loss are specified in **Extended Data Table 4**.

To preserve the gene panel **reconstruction** capabilities of SEAL during the alignment, we maintain the gene reconstruction task as an auxiliary objective. The SEAL-omics branch continues to be optimized using the Stage I objective $\mathcal{L}_{rec,gene}$ (Equation 7). To ensure the morphological features are concretely predictive of gene expression, the SEAL-vision branch is also trained to reconstruct the transcriptomic profile from the image patch directly, optimized via $\mathcal{L}_{rec,vision}$.

Finally, the SEAL dataset is a heterogeneous collection of studies, organs, and ST technologies, which introduces significant **batch effects** that do not correspond to biological signal. We implement a domain adaptation strategy as a further auxiliary task to ensure that the learned representations are discriminative for the primary task but invariant to the shift between data domains. We achieve this by training an auxiliary domain classifier to predict the study origin of each sample from both the vision and omics encoders. Crucially, a gradient reversal layer (GRL)⁷⁹ is inserted between the feature encoders and the domain classifier. During the forward pass, the GRL acts as an identity transform. Meanwhile, during backpropagation, the GRL multiplies the gradient it receives from the domain classifier by a negative constant before passing it to the preceding encoders. This creates an adversarial training objective where the domain classifier's parameters are optimized to minimize domain classification error (i.e., spotting batch effects) while the feature encoders' parameters are optimized to maximize the same error (i.e., making features from different domains more indistinguishable). This process applies a higher domain adaptation penalty \mathcal{L}_{da} if the model learns domain-specific artifacts and forces the finetuning process to produce more generalizable embeddings.

The final loss function for Stage II training is a weighted function between the contrastive image reconstruction, gene reconstruction, and domain adaptation objectives:

$$\mathcal{L} = \lambda_0 \mathcal{L}_{InfoNCE}(\mathbf{z}^{(p)}, \mathbf{z}^{(g)}) + \lambda_1 \mathcal{L}_{rec,img}(\hat{\mathbf{y}}^{(p)}) + \lambda_2 \mathcal{L}_{rec,gene}(\hat{\mathbf{y}}^{(g)}) + \lambda_3 \mathcal{L}_{da}, \quad (9)$$

where the values of λ are picked to ensure that no single loss dominates the gradient updates.

Stage III - Evaluation.

Evaluation Scope. To demonstrate the versatility of the learned morphomolecular embeddings, we evaluate SEAL on a highly diverse set of 38 slide-level downstream tasks from 14 datasets across seven major organs (Breast, Brain, Colon, Kidney, Lung, Ovary, Pancreas) and 15 patch-level downstream tasks across nine major organs (Breast, Brain, Colon, Kidney, Lung, Lymph Node, Prostate, Rectum, Skin). Our evaluation covers five types of tasks: gene expression prediction (**Extended Data Tables 7 to 13**), molecular status prediction

(**Extended Data Tables 18 to 36**), pathway expression prediction (**Extended Data Tables 41 to 54**), IHC status prediction (**Extended Data Figure 1**), treatment response prediction (**Extended Data Table 39**), survival prediction (**Extended Data Table 40**), gene-to-image retrieval, and image-to-gene retrieval (**Figure 5**). We provide a brief description of each dataset below.

- **BC therapy.** We used the public BC therapy⁸⁰ dataset comprising 166 patients with invasive breast cancer, each associated with an H&E-stained image of the pre-neoadjuvant therapy biopsy. We design two molecular prediction tasks: prediction of ER status (n=166 cases) and prediction of HER2 status (n=166 cases), and cancer grade prediction (n=166 cases). All slides were scanned with an Aperio scanner at 20× (0.50 μ m/px). Results are reported in **Extended Data Tables 18, 19 and 37**.
- **BCNB.** We used the public BCNB dataset⁸¹ (Breast Cancer Core-Needle Biopsy) for IHC status prediction in breast cancer. BCNB comprises 1,058 WSIs (one WSI per patient), which we use for ER status prediction, PR status prediction, and HER2 status prediction. Additional information is provided in **Extended Data Tables 20 to 22**.
- **BReAst Carcinoma Subtyping (BRACS).** We used the public BRACS dataset⁸² for coarse- and fine-grained breast morphological subtyping. BRACS consists of 547 breast carcinoma WSIs from 189 patients sourced from IRCCS Fondazione Pascale. Each WSI is used for coarse-grained (3 classes) and fine-grained (6 classes) morphological subtyping. Due to the limited size of the official test set, we redefined train-test splits with an 80:20 ratio. Because BRACS-Fine and BRACS-Coarse are slide-level prediction tasks with multiple slides per case, we kept all slides belonging to the same patient together, ensuring one patient does not end up in both train and test. Therefore, this dataset was not explicitly label-stratified (as each patient would have multiple labels). Results are reported in **Extended Data Figure 1**.
- **CPTAC.** We used the public CPTAC data for pan-cancer mutation prediction^{83,84}. Specifically, we included (1) CPTAC-BRCA (invasive breast cancer) for PIK3CA and TP53 mutation prediction, (2) CPTAC-CCRCC (clear-cell renal-cell carcinoma) for BAP1, VHL, and PBRM1 mutation prediction, (3) CPTAC-COAD (colon adenocarcinoma) for KRAS, SETD1B, TP53, APC, PIK3CA, ARID1A, and ACVR2A mutation prediction and MSI status, (4) CPTAC-GBM (glioblastoma) for EGFR and TP53 mutation prediction, (5) CPTAC-LUAD (lung adenocarcinoma) for EGFR, STK11, and TP53 mutation prediction, (6) CPTAC-PDAC (pancreatic ductal adenocarcinoma) pathway expression prediction. For all tasks, we predict the pathway expression for the PI3K/AKT/mTOR signalling (MTOR), Epithelial-Mesenchymal Transition (EMT), and G2/M checkpoint (G2M) pathways from the Hallmark gene sets⁸⁵. Results are reported in **Extended Data Tables 23 to 33, 36 and 41 to 54**.

- **DHMC-Kidney.** We used the public DHMC-Kidney dataset⁸⁶ comprising 563 cases of renal cell carcinoma, each associated with one H&E-stained slide (**Extended Data Figure 1**).
- **EBRAINS.** We used the EBRAINS dataset⁸⁷ for coarse- and fine-grained brain tumor subtyping, as well as IDH1 mutation prediction. EBRAINS consists of 3,114 WSIs acquired by the EBRAINS Digital Tumor Atlas at the University of Vienna. We reused splits from UNI⁵, which kept categories with at least 30 samples, resulting in 2,319 slides. Each WSI is used for fine-grained morphological subtyping across 30 diagnostic classes. Splits are stratified by patients to ensure slides from a patient are not found in both train and test splits. Additional information is provided in **Extended Data Figure 1**.
- **ICAIRD.** We used the ICAIRD⁶⁰ data collection, consisting of H&E-stained 100 whole slide images of renal cell carcinoma (Kidney) captured across five commonly used high-resolution slide scanners, each representing different data acquisition domains. As such, the images have subtle differences in color, contrast, and resolution depending on the scanner used. We test this dataset to investigate visual batch effects that pathology foundation models may pick up instead of the true biological signal in the slides. For this study, we included images from the Hamamatsu-2.0-HE (0.45 $\mu\text{m}/\text{px}$), Hamamatsu S60 (0.42 $\mu\text{m}/\text{px}$), Leica Aperio AT2 ($\mu\text{m}/\text{px}$), Zeiss Axio Z1-Grant (0.22 $\mu\text{m}/\text{px}$), and Zeiss Axio Z1-Louise (0.22 $\mu\text{m}/\text{px}$).
- **MGB-Breast.** We used an internal cohort of invasive breast cancer (BRCA) for morphological and immunohistochemistry status prediction^{19,88}. MGB-Breast comprises 1,264 WSIs (mix of biopsies and resections) scanned from Brigham and Women’s Hospital (one WSI per patient). We curated two immunohistochemistry (IHC) status prediction tasks: estrogen receptor (ER) status prediction and progesterone receptor (PR) status prediction. ER and PR status were manually extracted from pathology reports. Results are provided in **Extended Data Figure 1**.
- **MUT-HET-RCC.** We used the MUT-HET-RCC dataset⁸⁹ for mutation prediction in renal cell carcinoma. MUT-HET-RCC comprises 1,291 WSIs (one WSI per patient) which we use for (1) PBRM1 mutation prediction, and (2) SETD2 mutation prediction. Additional information is provided in **Extended Data Table Tables 34 and 35**.
- **Ovarian Treatment Response.** We used the OV-Bevacizumab dataset⁹⁰ for treatment response prediction in ovarian cancer. OV-Bevacizumab consists of 288 WSIs from 78 patients. Non-responders are defined as having a measurable regrowth of the tumor or as a serum CA-125 concentration of more than twice the value of the upper limit of normal during the treatment course for the bevacizumab therapy. We kept all patients who received bevacizumab as their first-line treatment and additionally removed four cases (case IDs: P00181938C, 2630938, 2224393, 2937351), which were labeled as both responders and non-responders, yielding 85 WSIs from 36 patients. Additional information is provided in **Extended Data Table 39**.

- **PANDA.** We used the public PANDA (Prostate cANcer graDe Assessment) data for prostate cancer grading (ISUP grading)⁹¹. PANDA comprises 10,616 core needle biopsies from Radboud University Medical Center and Karolinska Institute, each annotated with an ISUP grade (6-class classification task). We follow prior work^{5,92} in excluding slides with equivocal labels²⁰, which resulted in 9,555 slides. We used the train split (7,647 WSIs) and test split (954 WSIs) from GigaPath¹⁷, and we did not use their validation split (954 WSIs). Additional information is provided in **Extended Data Table 1**.
- **SURGEN.** We used public cases from the SR386 cohort of SurGen⁹³, which includes 389 patients with colon and rectum adenocarcinoma, predicting overall survival for each patient. Additional information is provided in **Extended Data Table 40**.

Linear Probing (Patch-level). Patch-level tasks are evaluated using a linear probe of the frozen patch embeddings. We assess the quality of these representations on two patch-level gene expression prediction tasks (SEAL-Test and HestBench). For the linear probe, we first apply Principal Component Analysis (PCA) to the frozen embeddings to reduce the dimensionality to 256 factors. This is done to prevent performance penalties of the downstream probe for larger embeddings²⁵. A Ridge regression model is trained on the PCA components to predict the count-normalized HVG expression levels. All results are evaluated using 5-fold cross-validation, with the performance quantified by the Pearson Correlation Coefficient (PCC) and Mean Squared Error (MSE) between the predicted and ground truth expression values across folds.

Multiple Instance Learning (Slide-level). To evaluate slide-level task performance, the patch embeddings from a given WSI are aggregated into a single slide-level representation using two standard Multiple Instance Learning (MIL) methods. We use mean pooling as a simple non-parametric baseline where all patch embeddings are averaged to produce the slide-level feature vector. Additionally, we train Attention-based MIL (ABMIL)⁵³, a learnable aggregation method where a gated attention mechanism assigns an importance score to each patch embedding to emphasize more relevant tissue regions. The slide-level representation is then calculated by averaging patch embeddings, weighted by the attention scores.

Retrieval. SEAL has the ability to run cross-modal image-to-gene (i2g) and gene-to-image (g2i) retrieval. Each of these approaches uses a query vector and a set of reference vectors from the aligned embedding space. For i2g retrieval, we use a patch embedding $\mathbf{z}_i^{(p)}$ as the query and the set of all ST embeddings from a support set as the reference vectors. We calculate the cosine similarity vector (for single queries) or matrix (for batched queries) with each value as $s_{ij} = \cos(\mathbf{z}_i^{(p)}, \mathbf{z}_j^{(g)})$ for all $\mathbf{z}_j^{(g)} \in \mathcal{Z}_{train}^{(g)}$ and select the set of indices \mathcal{K} for the Top-K retrieved ST embeddings (with K=50). The final i2g retrieved expression profile $\hat{\mathbf{y}}_i^{(g)}$ is the similarity-weighted

average of the corresponding ground-truth gene panels $\{x_k^{(g)}\}_{k \in \mathcal{K}}$:

$$\hat{y}_i^{(g)} = \frac{\sum_{k \in \mathcal{K}} s_{ik} \cdot x_k^{(g)}}{\sum_{k \in \mathcal{K}} s_{ik}}. \quad (10)$$

For g2i retrieval, we construct an in silico transcriptomic profile $x_{query}^{(g)} \in \mathbb{R}^G$ based on a specific biological pathway or gene signature. First, we define the “active” genes such as *KLK3* and *AMACR* for Prostate retrieval. This gene set is expanded by identifying correlated genes from the train gene panel, selecting all genes with a $PCC > 0.3$ to the active genes. Next, we filter all ST spots within the MAPLE-Train data for the query organ, retaining only spots with at least 50% of genes that show expression above the 75th percentile for each gene. The SEAL-omics embeddings $z_j^{(g)}$ for all these spots are then averaged to create a single and robust molecular query $x_{query}^{(g)}$ and its embedding $z_{query}^{(g)}$. Using this query embedding and the patch reference set $Z_{train}^{(p)}$, we retrieve the patches with the highest cosine similarity.

Evaluation Metrics. We evaluate binary classification tasks using **macro AUC**, a threshold-free measure that plots the true positive rate against the false positive rate. The macro-AUC score ranges from 0.5, indicating random prediction, to 1, indicating perfect prediction. For multi-class subtyping, we report **balanced accuracy**, which accounts for class imbalance by computing the unweighted average of recall for each class. To assess multi-class grading tasks (rank-ordered), we utilize the **quadratic weighted Cohen’s kappa**, which quantifies agreement between model and ground truth while penalizing disagreement on the distance between categories. Kappa scores range from -1 (complete disagreement) to 1 (perfect agreement), while 0 indicates agreement by random chance. For regression tasks, including gene expression and pathway expression prediction, we assessed performance using the Pearson Correlation Coefficient (PCC), Spearman’s rank correlation coefficient, and Mean Squared Error (MSE). PCC measures the strength and direction of the linear relationship between predicted and ground truth values of expression as a measure between -1 and 1, with a higher correlation coefficient indicating improved predictive performance. Spearman’s rank correlation captures the relative ordering of expression levels independent of their absolute magnitude or specific data distribution. Finally, to track the absolute magnitude, we also track the mean squared error between predicted and ground truth values.

Statistical analysis. For all tasks, we report the mean and standard error across all folds for the task-relevant evaluation metrics. If only a single fold is available, we estimate the confidence intervals through bootstrapping 100 iterations. We compare the performance after SEAL training to the vision-only baselines using a one-sided paired Wilcoxon Signed-Rank to determine whether the performance difference between the models is statistically significant for all evaluation metrics.

Computing Hardware and Software This project is implemented using Python 3.9 and PyTorch (version 2.1.2) with CUDA (12.1) (<https://pytorch.org/>), which can be replicated by leveraging several open-source libraries as outlined below. All training was done on three 24 GB NVIDIA GeForce RTX 3090 GPUs using PyTorch’s distributed data parallel backend, which was called through Huggingface’s accelerate library (<https://huggingface.co/docs/accelerate/en/index>). Implementations of the slide encoder backbones can be found at the following links: CONCH (<https://huggingface.co/MahmoodLab/CONCH>), H0-mini(<https://huggingface.co/bioptimus/H0-mini>), Phikon-v2 (<https://huggingface.co/owkin/phikon-v2>), UNI-v2-h (<https://huggingface.co/MahmoodLab/UNI2-h>), and Virchow-v2 (<https://huggingface.co/paige-ai/Virchow2>). Slide processing was done using the TRIDENT library (<https://github.com/mahmoodlab/trident>), which builds on OpenSlide (version 4.0.0.6). Processing and analysis of spatial transcriptomics data was performed using scanpy (version 1.10.3). The LoRA implementation uses the PEFT library (version 0.15.2). The OpenClip implementation was used (https://github.com/mlfoundations/open_clip). The linear probing and dimensionality reduction was implemented through the NVIDIA Rapids cuml library (version 24.8). Image augmentations were implemented using albumentations (<https://albumentations.ai/>). Statistical testing was done using scipy’s stats package (version 1.15.2) and further metrics were calculated using scikit-learn (version 1.4.0). Further dependencies can be found in the environment.yaml file on <https://github.com/mahmoodlab/SEAL/>.

Code availability The model weights and code are available at <https://github.com/mahmoodlab/SEAL/>.

Data availability The source data used to derive the SEAL training, test, and HestBench can be accessed using the HEST package (<https://github.com/mahmoodlab/HEST>). Data splits for the public downstream tasks are available at (<https://github.com/mahmoodlab/Patho-Bench>). The slides for the majority of downstream tasks are publicly available CPTAC (<https://www.cancerimagingarchive.net/collection/cptac-brca/>), Ebrains (<https://doi.org/10.25493/WQ48-ZGX>), BRACS (<https://www.bracs.icar.cnr.it/>), BCNB (<https://bupt-ai-cz.github.io/BCNB/>), PANDA (<https://panda.grand-challenge.org/data/>), MUT-HET-RCC (<https://doi.org/10.25452/figshare.plus.c.5983795>), Surgen (<https://www.ebi.ac.uk/biostudies/bioimages/studies/S-BIAD1285>), DHMC-Kidney (<https://bmirds.github.io/KidneyCancer/>), BC Therapy (<https://zenodo.org/records/6337925#.Y30d1y-11Ls>). Further evaluation data from BWH and MGH are proprietary patient data, and cannot be made publicly available.

Ethics Statement The retrospective analysis of internal pathology images and associated reports used in this study received approval from the Mass General Brigham institutional review board. Prior to the computational analysis and model development, all internal digital data, including whole slide images (WSIs), pathology reports, and electronic medical records, were anonymized. Since the study did not involve direct patient participation or recruitment, informed consent was waived for the analysis of archival pathology slides.

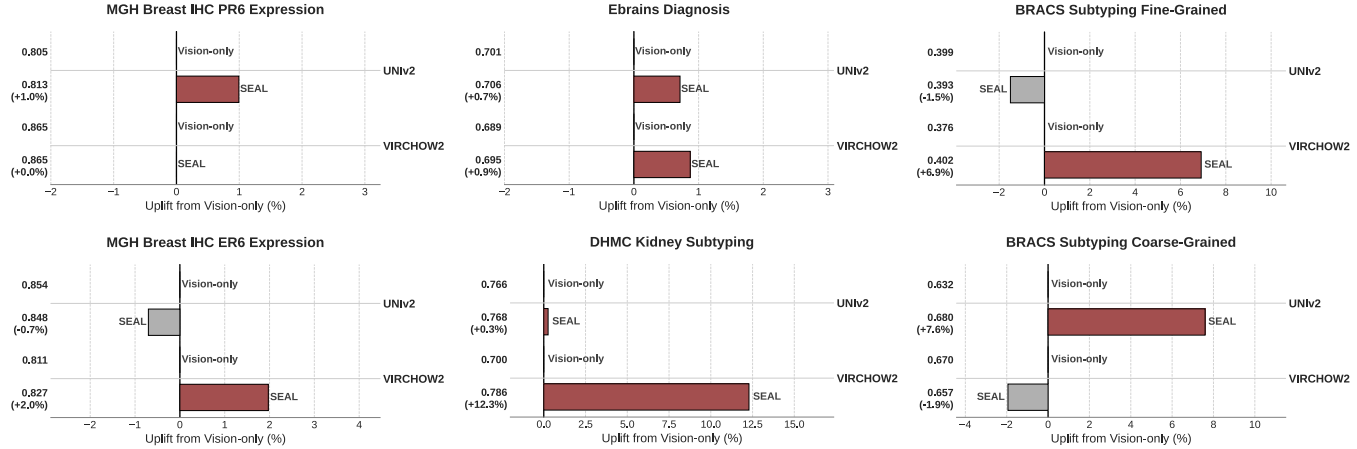
Author Contributions

K.H, A.H.S, and F.M conceived the study and designed the experiments. C.A.P conducted experimental analysis, especially for cross-modal retrieval tasks and the preparation and analysis of the in-house prostate samples. G.J helped the curation of the MAPLE dataset. S.J.W and A.V helped set up the evaluation pipeline for slide-level tasks. K.H and A.H.S prepared the manuscript. All authors contributed to the writing. N.S, M.J and F.M supervised the research.

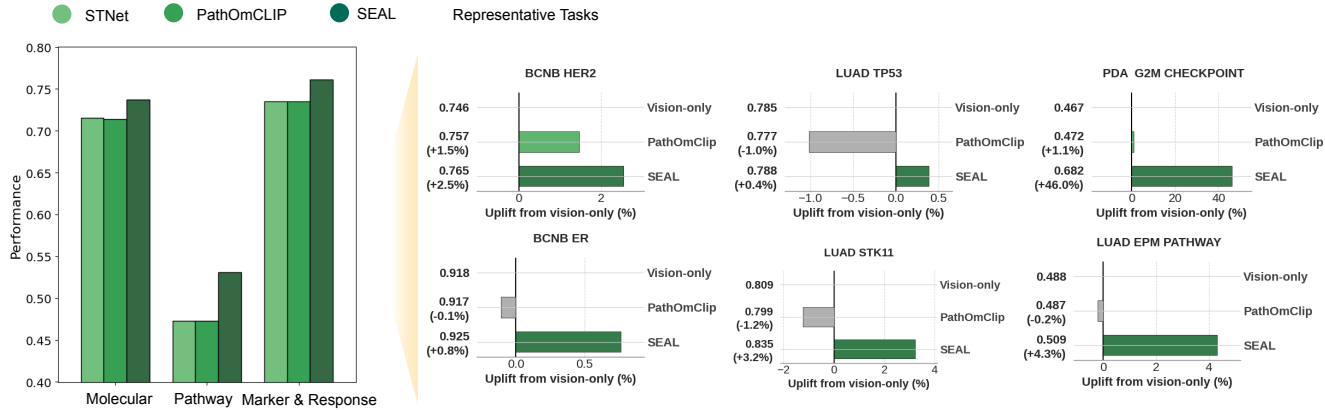
Acknowledgements

This work was funded in part by the Brigham and Women’s Hospital (BWH) President’s Fund, Mass General Hospital (MGH) Pathology and by the National Institute of Health (NIH) National Institute of General Medical Sciences (NIGMS) through R35GM138216. K.H was supported by a scholarship through the Gates Cambridge Trust and University of Cambridge Computer Laboratory Travel Grant. C.A.P was supported by the Rafael del Pino Foundation. N.S and M.J acknowledge the support of the U.S. Army Medical Research and Development Command of the Department of Defense through the FY22 Breast Cancer Research Program of the Congressionally Directed Medical Research Programs, Clinical Research Extension Award GRANT13769713. The content is solely the responsibility of the authors and does not reflect the official views of the NIH, NIGMS, and DoD.

A. Morphological & IHC Tasks (ABMIL) - 6 tasks

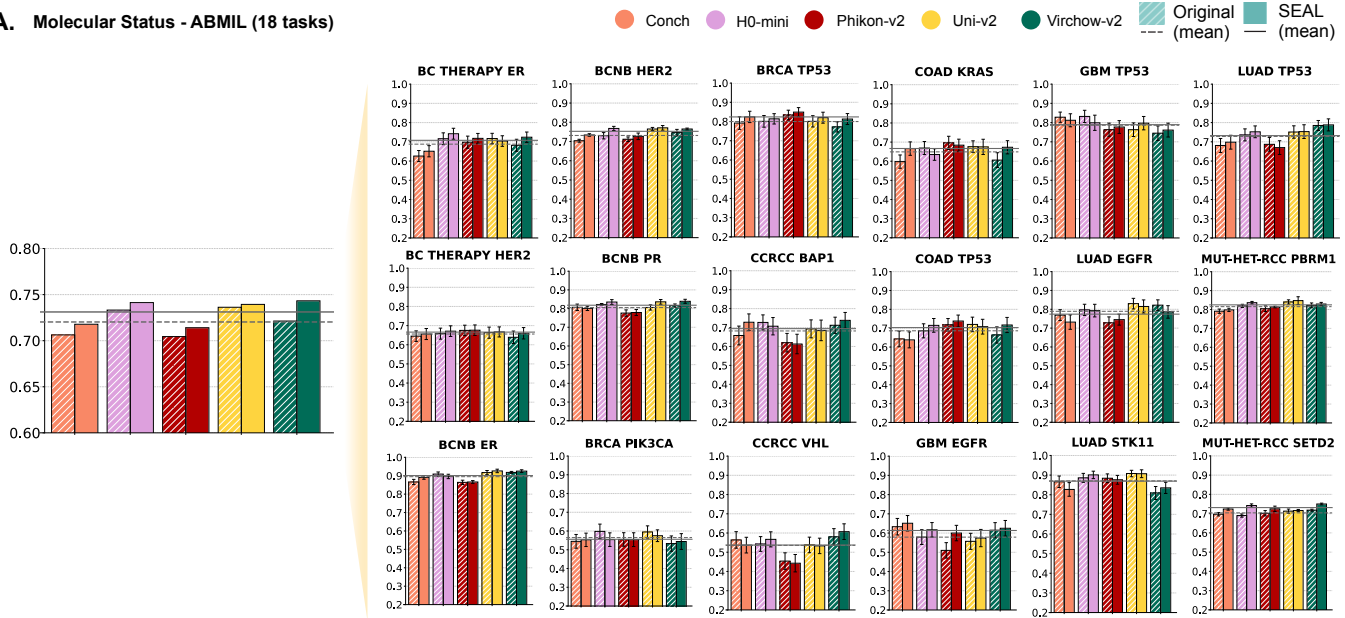


B. ST Baseline Slide-level Task Performance (ABMIL, Virchow-v2) - 6 tasks

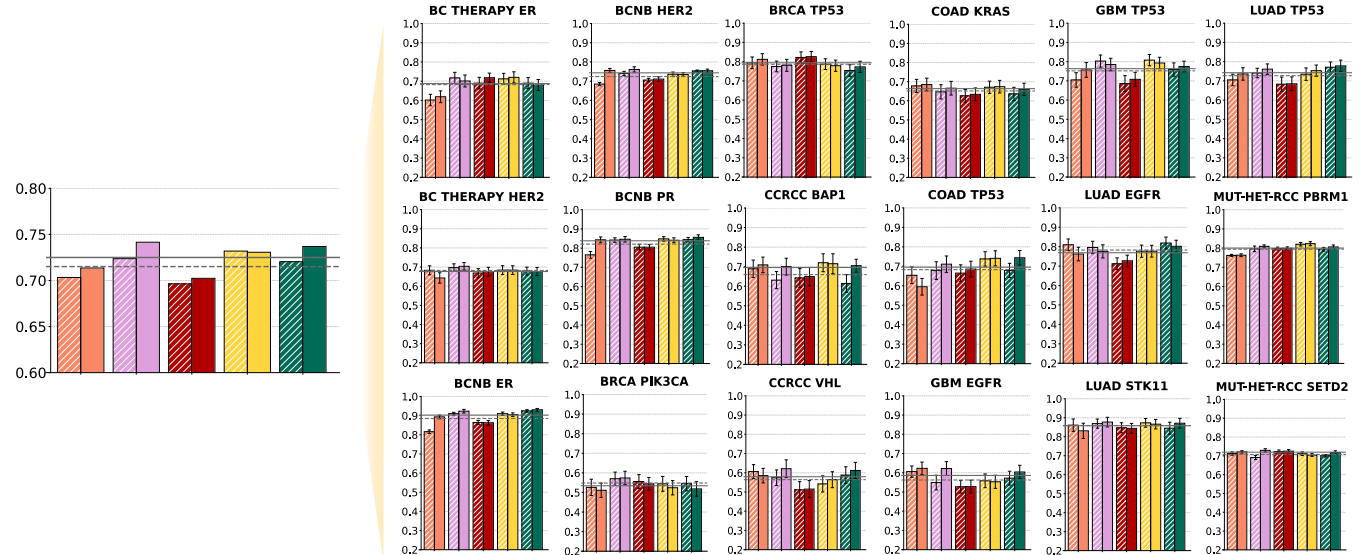


Extended Data Figure 1: **Slide-level morphological and IHC tasks & slide-level comparison with ST baselines.** (A). Slide-level performance on two IHC slide-level prediction and four slide-level morphological classification tasks: IHC ER6 and PR6 expression prediction (6 classes, measured using Cohen's weighted kappa), Ebrains diagnosis classification (30 classes, measured using balanced accuracy), DHMC Kidney subtyping (5 classes, measured using balanced accuracy), BRACS subtyping as fine-grained (7 classes, measured using balanced accuracy) and coarse-grained (3 classes, measured using balanced accuracy) classification task. The chart shows the relative change of SEAL over the vision-only baseline for Uni-v2 and Virchow-v2. (B). Comparison of SEAL with the two best-performing patch-level fine-tuning methods (ST-Net, PathOmCLIP) on the full set of slide-level tasks: molecular status prediction, pathway expression, and marker & response prediction tasks. Performance is measured relative to the ST-Net baseline.

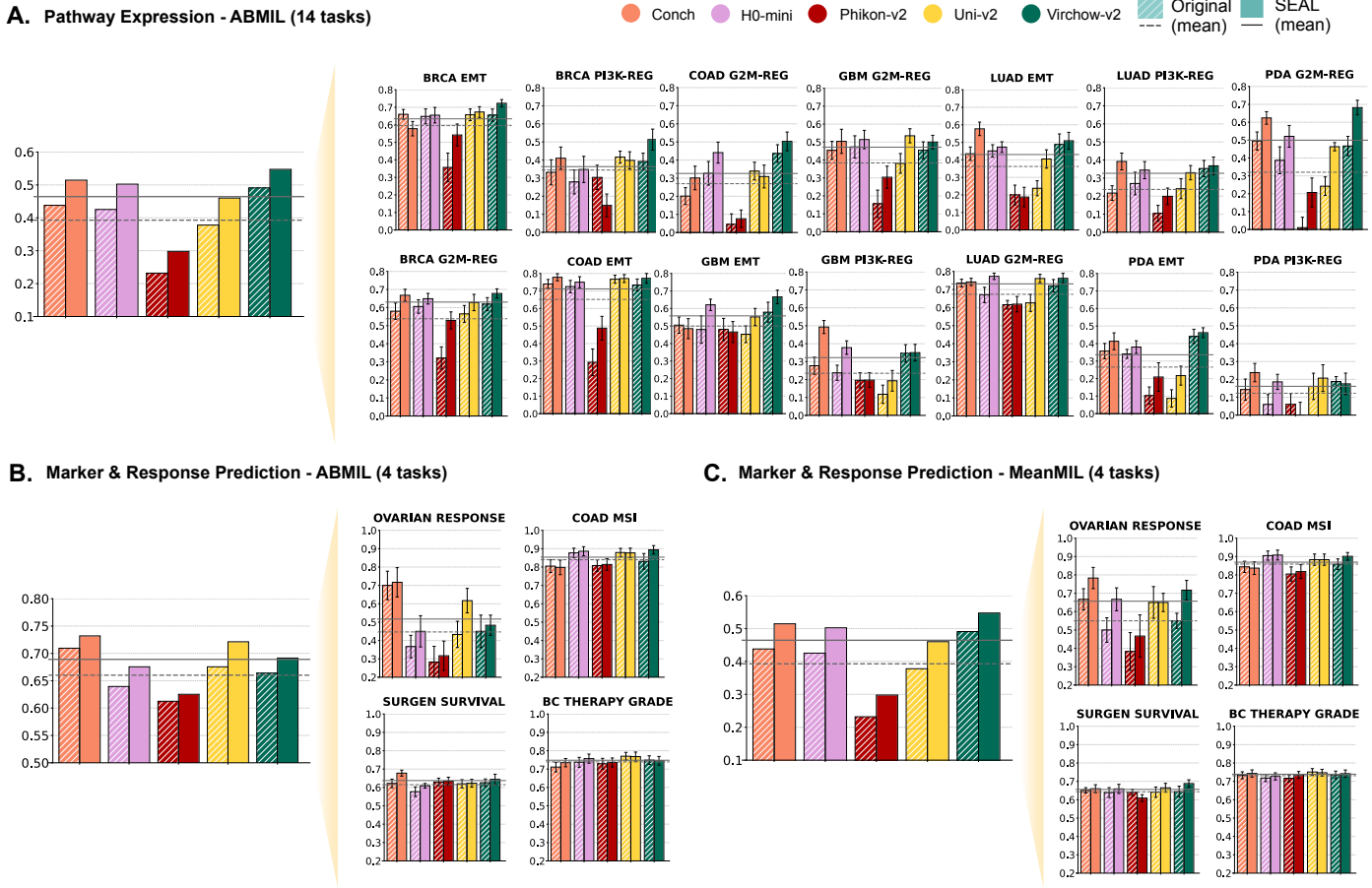
A. Molecular Status - ABMIL (18 tasks)



B. Molecular Status - MeanMIL (18 tasks)

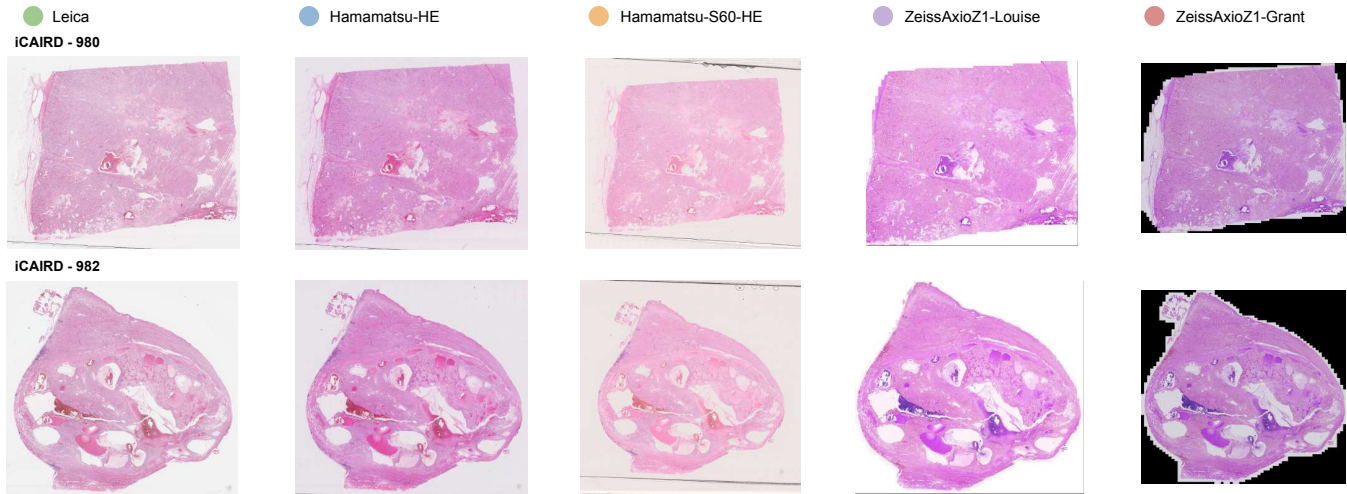


Extended Data Figure 2: Comparison between original and SEAL-finetuned molecular prediction tasks.
(A). Attention-based MIL (ABMIL) performance for 18 slide-level molecular subtyping tasks. ABMIL was applied on patch embeddings extracted from five vision encoders (Conch, H0-mini, Phikon-v2, Uni-v2, and Virchow-v2) and their SEAL-finetuned variants. Binary tasks are evaluated using AUC and multi-class classification tasks using balanced accuracy. **(B).** Same tasks as (A), replacing ABMIL by mean MIL.

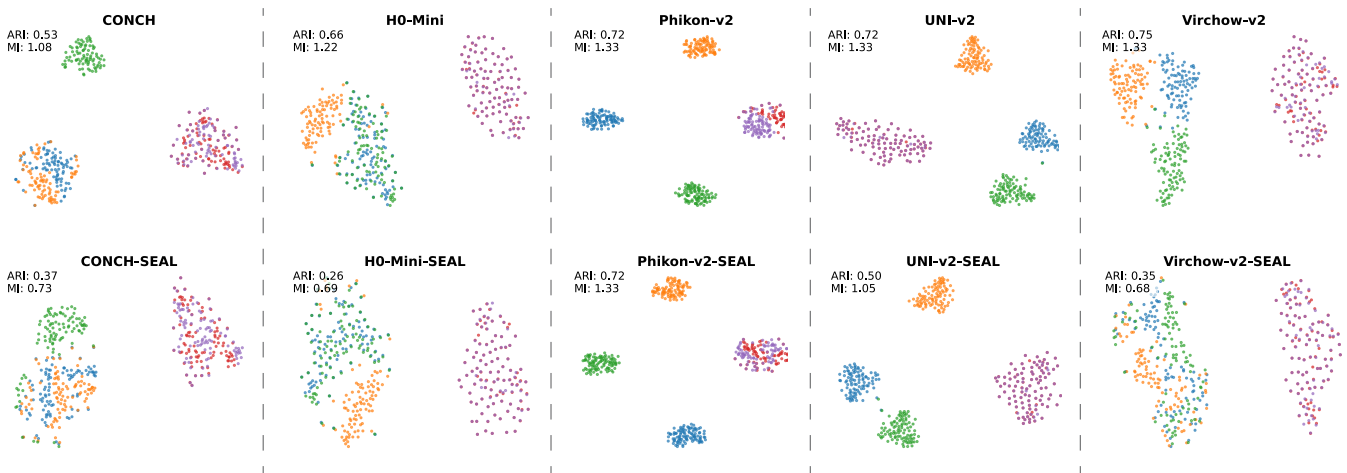


Extended Data Figure 3: **SEAL pathway expression & treatment response prediction.** (A). Slide-level prediction performance of Bulk RNA expression of three MSigDB Hallmark pathways: Genes up-regulated by activation of the PI3K/AKT/mTOR pathway (PI3K-REG), genes involved in the G2/M checkpoint (G2M-REG), and genes defining epithelial-mesenchymal transition (EMT). Performance is measured as the Pearson Correlation Coefficient between predicted pathway expression and measured bulk pathway expression. (B). ABMIL results on four slide-level tasks: treatment response prediction of patients with ovarian cancer and treated with Bevacizumab, microsatellite instability prediction in colon adenocarcinoma (COAD), overall survival prediction of colon and rectum adenocarcinoma, and breast cancer grading. (C). MeanMIL results on the same set of four slide-level tasks as in (B)..

A. Scanner Type Differences



B. Embedding Batch Effect Robustness



Extended Data Figure 4: **Robustness Analysis of SEAL**. We analyze to what extent the baseline foundation models and SEAL are susceptible to batch effects introduced by differing data acquisition domains of the same Hematoxylin & Eosin slides. The ICAIRD dataset contains 100 renal cell carcinoma slides captured across five scanners: Hamamatsu-2.0-HE ($0.45 \mu\text{m}/\text{px}$), Hamamatsu S60 ($0.42 \mu\text{m}/\text{px}$), Leica Aperio AT2 ($\mu\text{m}/\text{px}$), Zeiss Axio Z1-Grant ($0.22 \mu\text{m}/\text{px}$), and Zeiss Axio Z1-Louise ($0.22 \mu\text{m}/\text{px}$). **(A)**. Visual differences of two sample slides in the ICAIRD dataset, exhibiting subtle differences in color, contrast, resolution, and other imaging characteristics across scanners. **(B)**. Benchmarking of five vision foundation models (CONCH, H0-Mini, Phikon-v2, UNI-v2, Virchow-v2) and SEAL for each of the encoders. The scatter plots show the t-SNE of the mean patch embedding for each slide in the dataset, colour-coded by the slide scanner. Weaker clusters (lower ARI and MI) correspond to lower susceptibility to visual batch effects and consequently higher robustness. ARI: Adjusted Rand Index, MI: Mutual Information.

Extended Data Table 1: Training, validation, and test dataset overview of the MAPLE-790k dataset by tissue type. The dataset was curated by filtering human Visium Slides from the HEST-1k dataset. The data was split using a stratified 80-10-10 split by patient and organ to ensure that no spots from the same patient were present in the validation or test set. The in-domain test set was further subset based on the support in the training data.

	Train		Validation		Test		Total	
	WSIs	Spots	WSIs	Spots	WSIs	Spots	WSIs	Spots
Bladder	5	5,200	1	1,017	0	0	6	6,217
Bowel	55	172,901	6	14,312	0	0	61	187,213
Brain	30	100,727	4	9,291	6	22,526	40	132,544
Breast	5	19,685	1	2,518	1	4,015	7	26,218
Cervix	5	7,764	0	0	0	0	5	7,764
Heart	38	95,166	4	9,674	0	0	42	104,840
Kidney	29	36,742	3	2,105	6	8,136	38	46,983
Liver	11	54,905	1	4,991	0	0	12	59,896
Lung	28	56,776	3	3,777	6	9,063	37	69,616
Ovary	2	8,129	0	0	0	0	2	8,129
Pancreas	4	13,001	0	0	0	0	4	13,001
Prostate	9	33,080	1	4,248	2	8,179	12	45,507
Skin	46	41,203	5	4,606	12	17,298	63	63,107
Uterus	15	18,312	2	3,120	0	0	17	21,432
Sum	282	663,591	31	59,659	33	69,217	346	792,467

Extended Data Table 2: Training, validation, and test dataset overview of the MAPLE-790k dataset by disease state. The dataset was curated by filtering human Visium Slides from the HEST-1k dataset. The data was split using a stratified 80-10-10 split by patient and organ to ensure that no spots from the same patient were present in the validation or test set.

	Train		Validation		Test		Total	
	WSIs	Spots	WSIs	Spots	WSIs	Spots	WSIs	Spots
Cancer	88	277,015	13	31,386	10	31,115	111	339,516
Diseased	90	128,466	9	11,805	12	13,892	111	154,163
Healthy	88	228,191	5	12,279	5	15,147	98	255,617
Treated	16	29,919	4	4,189	6	9,063	26	43,171
Sum	282	663,591	31	59,659	33	69,217	346	792,467

Extended Data Table 3: Source overview of the MAPLE-790k Visium slides used for training of SEAL. All raw were obtained through the HEST-1k library.

Dataset	Study Link	Samples used
Spatial transcriptomics landscape of non-communicable inflammatory skin diseases	Link	59
Spatially resolved multiomics of human cardiac niches	Link	41
COLON MAP: Colon Molecular Atlas Project	Link	39
Spatial localization with Spatial Transcriptomics for an atlas of healthy and injured cell states and niches in the human kidney	Link	23
Spatially resolved transcriptomic profiling of degraded	Link	21
A spatially resolved atlas of the human lung characterizes a gland-associated immune niche	Link	20
SARS-CoV-2 Niches in Human Placenta Revealed by Spatial Transcriptomics	Link	15
Spatial transcriptomics reveal unresolved wound repair as potential driver of PFA Ependymoma progression	Link	14
spatialLIBD	Link	12
Multimodal decoding of human liver regeneration	Link	8
Genome-wide Spatial Expression Profiling in Formalin-fixed Tissues: Supplementary Data	Link	8
Genome-wide Spatial Expression Profiling in Formalin-fixed Tissues	Link	7
A Spatial Transcriptomic atlas of the human kidney papilla identifies significant immune injury in patients with stone disease	Link	7
Prostate ST Internal	N/A (internal)	5
Spatial Multimodal Analysis: MALDI-MSI and Spatial Transcriptomics within the same tissue section	Link	5
Human ileum, Visium	Link	4
Human squamous cell carcinoma	Link	4
Schwann Cells Shape Tumor Cells and Cancer-Associated Fibroblasts in the Pancreatic Ductal Adenocarcinoma Microenvironment	Link	4
Single-cell and spatial transcriptomics characterisation of the immunological landscape in the healthy and PSC human liver	Link	4
Charting the Heterogeneity of Colorectal Cancer Consensus Molecular Subtypes using Spatial Transcriptomics: datasets	Link	4
Spatiotemporally Deciphering the Unknown Role of Persistent HPV Infection in Precancer to Cervical Cancer Progression: Integrating Single-Cell RNA-Sequencing Landscape and Spatial Transcriptomics Atlas	Link	4
A single-cell transcriptomic analysis of endometriosis	Link	2
COLON MAP: Colon Molecular Atlas Project	Link	2
Batf3-dendritic cells and 4-1BB-4-1BB ligand axis are required at the effector phase within the tumor microenvironment for PD-1-PD-L1 blockade efficacy	Link	2
High resolution mapping of the tumor microenvironment using integrated single-cell, spatial and in situ analysis	Link	1

Extended Data Table 4: **Hyperparameter overview by encoder backbone used for training and evaluation.**

	Conch-SEAL	H0-mini-SEAL	Phikon-v2-SEAL	Uni-v2-SEAL	Virchow-v2-SEAL
Fine-tuning blocks	3	3	7	5	7
Optimizer	AdamW	AdamW	AdamW	AdamW	AdamW
LoRA Rank	8	8	8	8	8
LoRA Alpha	8	8	8	8	8
LoRA Dropout	0.25	0.25	0.25	0.5	0.25
SEAL-Image LR	0.0001	0.0001	0.0001	0.0001	0.0001
SEAL-Omics LR	0.0001	0.0001	0.0001	0.0001	0.0001
Stage I Warmup LR	0.0005	0.0005	0.0005	0.0005	0.0005
$\lambda_{contrast}$	1	1	3	1	1
$\lambda_{rec,img}$	1	1	3	3	1
$\lambda_{rec,gene}$	1	1	1	1	1
λ_{da}	0.001	0.001	0.001	0.001	0.001
Auxiliary projection	linear	linear	none	linear	none
Embedding Dims	512	1536	1024	1536	2560
Scheduler	CosAnneal	CosAnneal	CosAnneal	CosAnneal	CosAnneal
Batch Size	384	384	300	150	384
VAE Norm Flow	True	True	True	True	True
VAE Dropout	0	0	0	0	0
Decoder Dropout	0	0	0	0.3	0
Layer Decay	0.7	0.7	0.7	0.7	0.7
Temperature	0.05	0.05	0.05	0.05	0.05
Local smoothing	True	True	True	True	True
Weight decay	0.2	0.2	0.2	0.2	0.2
Gene Panel Size	2000	2000	2000	2000	2000
Warmup Epochs	3	3	3	3	3
Linear Probe	ridge	ridge	ridge	ridge	ridge

Extended Data Table 5: **Vision encoders fine-tuned using SEAL**. Encoders were selected to reflect a diverse range of model backbones (size and patch size), pre-training data distributions, and self-supervised learning (SSL) methods.

Encoder	Backbone	Pre-training	# Params	Dim	# Tiles	# Slides	Top 3 Organs
Conch ¹²	ViT-B/16	Contrastive	90 M	512	1.7 M	n/a	Gastro, Soft tissue, Lung
H0-Mini ⁴¹	ViT-B/14	Distillation	86 M	1536	43 M	6093	n/a
Phikon-v2 ⁹	ViT-L/16	Dino-v2	307 M	1024	460 M	58359	Breast, Lung, Colorectal
Uni-v2-h ⁵	ViT-H/14	Dino-v2	681 M	1536	100 M	100000	Heart, Lung, Kidney
Virchow-v2 ⁷	ViT-H/16	Dino-v2	632 M	2560	2000 M	3100000	Breast, Lymph Node, Skin

Extended Data Table 6: **Image augmentation transforms applied during Stage II training**. The augmentations refer to the Albumentations implementations of standard geometric, color jitter, and blurring augmentations, applied at different likelihoods for each sample (p). The "one of group" implies if only one of these implementations is applied for each sample, each at varying probabilities.

Method	Likelihood (p)	Arguments	One of Group
Resized Crop	1.0	Crop scale=(0.8, 1.0)	
Horizontal Flip	0.5		
Vertical Flip	0.25		
Image Compression	1.0	Quality range=(50,100)	
Hue/Saturation/Value Jitter	1.0	hue=(-40, 40), sat=(-20, 20), val=(-30,30)	A
RGB Shift	1.0	r=(-30, 30), g=(-40, 20), b=(-30, 30)	A
Brightness/Contrast Shift	1.0	b=0.1, c=0.1	A
Channel Shuffle	0.5		A
Gaussian Blur	0.1	blur_lim=(9,9), sigma_lim=(0.1,2)	

Extended Data Table 7: **Comparison of 5 Vision-Only vs. SEAL fine-tuned encoders on the Prostate** Maple-test set. Results show a linear probe using PCA (256 factors) + Ridge regression for the top 10 highly variable genes (HVGs) across Maple-train prostate samples for each encoder. Reported results show the mean and standard deviation across 5 probing folds and p-values calculated across the folds. HVGs: IGHM, IGHG3, CD226, CTSE, GNAL, RHOJ, IGLC1, MPP7, SCD5, GLTP

Method	PCC (\uparrow) (std.)	PCC %	MSE (\downarrow) (std.)	MSE %	PCC folds	p-value
CONCH	0.386 ± 0.002	-	0.854 ± 0.004	-	[0.3857, 0.385, 0.388, 0.3861, 0.3866]	-
CONCH-SEAL	0.420 ± 0.003	+8.81%	0.826 ± 0.005	-3.28%	[0.421, 0.4208, 0.4206, 0.4199, 0.4184]	<0.001
H0MINI	0.443 ± 0.002	-	0.805 ± 0.003	-	[0.4436, 0.4428, 0.4433, 0.4421, 0.4419]	-
H0MINI-SEAL	0.480 ± 0.003	+8.35%	0.766 ± 0.005	-4.84%	[0.4795, 0.4791, 0.4791, 0.4823, 0.4805]	<0.001
PHIKON2	0.444 ± 0.002	-	0.808 ± 0.004	-	[0.4436, 0.4446, 0.4435, 0.443, 0.444]	-
PHIKON2-SEAL	0.506 ± 0.002	+13.96%	0.743 ± 0.004	-8.04%	[0.5056, 0.5088, 0.5058, 0.5039, 0.5056]	<0.001
UNIv2	0.485 ± 0.002	-	0.764 ± 0.004	-	[0.483, 0.4846, 0.484, 0.486, 0.4859]	-
UNIv2-SEAL	0.548 ± 0.002	+12.99%	0.689 ± 0.004	-9.82%	[0.5457, 0.5503, 0.5472, 0.5478, 0.5485]	<0.001
VIRCHOW2	0.483 ± 0.002	-	0.764 ± 0.003	-	[0.4832, 0.4821, 0.4834, 0.4838, 0.4833]	-
VIRCHOW2-SEAL	0.576 ± 0.002	+19.25%	0.658 ± 0.003	-13.87%	[0.5752, 0.5752, 0.5744, 0.5765, 0.5772]	<0.001

Extended Data Table 8: **Comparison of 5 Vision-Only vs. SEAL fine-tuned encoders on the Brain Maple-test set.** Results show a linear probe using PCA (256 factors) + Ridge regression for the top 10 highly variable genes (HVGs) across Maple-train brain samples for each encoder. Reported results show the mean and standard deviation across 5 probing folds and p-values calculated across the folds. HVGs: ARHGEF28, TMEM117, RAD51B, SOX7, SCEL, MROH7, TRIM62, PRDM5, FGD6, LRRC10B

Method	PCC (\uparrow) (std.)	PCC %	MSE (\downarrow) (std.)	MSE %	PCC folds	p-value
CONCH	0.316 ± 0.003	-	0.176 ± 0.002	-	[0.3135, 0.3164, 0.3154, 0.3156, 0.3167]	-
CONCH-SEAL	0.351 ± 0.003	+11.08%	0.172 ± 0.002	-2.27%	[0.3499, 0.3502, 0.3516, 0.3507, 0.3524]	<0.001
H0MINI	0.363 ± 0.003	-	0.170 ± 0.002	-	[0.3628, 0.3618, 0.3635, 0.3643, 0.3608]	-
H0MINI-SEAL	0.393 ± 0.003	+8.26%	0.166 ± 0.002	-2.35%	[0.3922, 0.3932, 0.3937, 0.3932, 0.3928]	<0.001
PHIKON2	0.361 ± 0.003	-	0.170 ± 0.002	-	[0.3614, 0.362, 0.3605, 0.3596, 0.3609]	-
PHIKON2-SEAL	0.408 ± 0.003	+13.02%	0.164 ± 0.002	-3.53%	[0.4061, 0.4101, 0.4087, 0.4081, 0.407]	<0.001
UNIV2	0.396 ± 0.003	-	0.166 ± 0.001	-	[0.3945, 0.3967, 0.3949, 0.3983, 0.3959]	-
UNIV2-SEAL	0.439 ± 0.004	+10.86%	0.159 ± 0.002	-4.22%	[0.4374, 0.44, 0.4373, 0.4396, 0.4398]	<0.001
VIRCHOW2	0.388 ± 0.003	-	0.167 ± 0.002	-	[0.3889, 0.3867, 0.3878, 0.3882, 0.3889]	-
VIRCHOW2-SEAL	0.460 ± 0.003	+18.56%	0.157 ± 0.001	-5.99%	[0.4579, 0.4593, 0.4596, 0.4609, 0.4608]	<0.001

Extended Data Table 9: **Comparison of 5 Vision-Only vs. SEAL fine-tuned encoders on the Breast Maple-test set.** Results show a linear probe using PCA (256 factors) + Ridge regression for the top 10 highly variable genes (HVGs) across Maple-train breast samples for each encoder. Reported results show the mean and standard deviation across 5 probing folds and p-values calculated across the folds. HVGs: PLP1, PTPRZ1, SLC22A4, PDCD1LG2, IGHA2, GPM6A, ANO8, TGDS, PCDH9, PSTPIP1

Method	PCC (\uparrow) (std.)	PCC %	MSE (\downarrow) (std.)	MSE %	PCC folds	p-value
CONCH	0.436 ± 0.002	-	0.373 ± 0.002	-	[0.4358, 0.4356, 0.4355, 0.4358, 0.4358]	-
CONCH-SEAL	0.466 ± 0.002	+6.88%	0.361 ± 0.002	-3.22%	[0.466, 0.467, 0.4672, 0.4668, 0.4654]	<0.001
H0MINI	0.474 ± 0.003	-	0.353 ± 0.002	-	[0.476, 0.474, 0.4733, 0.4734, 0.473]	-
H0MINI-SEAL	0.509 ± 0.002	+7.38%	0.332 ± 0.002	-5.95%	[0.5088, 0.5088, 0.5084, 0.5112, 0.5087]	<0.001
PHIKON2	0.477 ± 0.002	-	0.351 ± 0.002	-	[0.4756, 0.476, 0.4775, 0.4771, 0.4785]	-
PHIKON2-SEAL	0.528 ± 0.002	+10.69%	0.317 ± 0.002	-9.69%	[0.5276, 0.5282, 0.5279, 0.5278, 0.5275]	<0.001
UNIv2	0.506 ± 0.003	-	0.328 ± 0.002	-	[0.5053, 0.5085, 0.5058, 0.5065, 0.5057]	-
UNIv2-SEAL	0.557 ± 0.002	+10.08%	0.300 ± 0.002	-8.54%	[0.5562, 0.5585, 0.5568, 0.5565, 0.5586]	<0.001
VIRCHOW2	0.501 ± 0.002	-	0.333 ± 0.002	-	[0.5003, 0.5005, 0.5022, 0.5019, 0.5008]	-
VIRCHOW2-SEAL	0.581 ± 0.002	+15.97%	0.281 ± 0.002	-15.62%	[0.5815, 0.5806, 0.5808, 0.581, 0.581]	<0.001

Extended Data Table 10: **Comparison of 5 Vision-Only vs. SEAL fine-tuned encoders on the Kidney Maple-test set.** Results show a linear probe using PCA (256 factors) + Ridge regression for the top 10 highly variable genes (HVGs) across Maple-train kidney samples for each encoder. Reported results show the mean and standard deviation across 5 probing folds and p-values calculated across the folds. HVGs: CD84, ABI3BP, NLRP1, MNDA, ZNF549, SLC44A4, IGHM, TRAF7, SCNN1B, PAICS

Method	PCC (\uparrow) (std.)	PCC %	MSE (\downarrow) (std.)	MSE %	PCC folds	p-value
CONCH	0.399 ± 0.002	-	0.652 ± 0.003	-	[0.3992, 0.3989, 0.3997, 0.3995, 0.3996]	-
CONCH-SEAL	0.432 ± 0.002	+8.27%	0.633 ± 0.004	-2.91%	[0.4319, 0.4318, 0.4322, 0.4326, 0.432]	<0.001
H0MINI	0.449 ± 0.002	-	0.619 ± 0.003	-	[0.4494, 0.4487, 0.4487, 0.4486, 0.4497]	-
H0MINI-SEAL	0.480 ± 0.002	+6.90%	0.598 ± 0.003	-3.39%	[0.4792, 0.4815, 0.4777, 0.4805, 0.4794]	<0.001
PHIKON2	0.445 ± 0.002	-	0.624 ± 0.004	-	[0.444, 0.4454, 0.4446, 0.4446, 0.4445]	-
PHIKON2-SEAL	0.498 ± 0.002	+11.91%	0.585 ± 0.003	-6.25%	[0.4982, 0.4986, 0.497, 0.499, 0.4973]	<0.001
UNIV2	0.483 ± 0.002	-	0.599 ± 0.004	-	[0.4816, 0.4829, 0.4839, 0.4828, 0.4823]	-
UNIV2-SEAL	0.536 ± 0.002	+10.97%	0.557 ± 0.002	-7.01%	[0.5349, 0.536, 0.5351, 0.5383, 0.5366]	<0.001
VIRCHOW2	0.476 ± 0.002	-	0.602 ± 0.003	-	[0.476, 0.474, 0.4769, 0.476, 0.4774]	-
VIRCHOW2-SEAL	0.556 ± 0.002	+16.81%	0.541 ± 0.003	-10.13%	[0.5563, 0.557, 0.5561, 0.5549, 0.5562]	<0.001

Extended Data Table 11: **Comparison of 5 Vision-Only vs. SEAL fine-tuned encoders on the Skin Maple-test set.** Results show a linear probe using PCA (256 factors) + Ridge regression for the top 10 highly variable genes (HVGs) across Maple-train skin samples for each encoder. Reported results show the mean and standard deviation across 5 probing folds and p-values calculated across the folds. HVGs: TMCC3, LRRC75A, SLAIN1, RTN4RL2, RHOH, COL4A5, KIFC1, CYP3A5, ENPEP, SPRYD7

Method	PCC (\uparrow) (std.)	PCC %	MSE (\downarrow) (std.)	MSE %	PCC folds	p-value
CONCH	0.427 ± 0.002	-	0.343 ± 0.002	-	[0.4262, 0.4271, 0.4277, 0.4281, 0.427]	-
CONCH-SEAL	0.455 ± 0.002	+6.56%	0.335 ± 0.002	-2.33%	[0.4542, 0.4553, 0.4553, 0.4558, 0.4532]	<0.001
H0MINI	0.475 ± 0.002	-	0.328 ± 0.002	-	[0.4745, 0.4747, 0.474, 0.4766, 0.4746]	-
H0MINI-SEAL	0.506 ± 0.002	+6.53%	0.317 ± 0.002	-3.35%	[0.5066, 0.5067, 0.505, 0.5059, 0.5039]	<0.001
PHIKON2	0.470 ± 0.003	-	0.329 ± 0.002	-	[0.471, 0.4697, 0.4692, 0.4685, 0.4699]	-
PHIKON2-SEAL	0.521 ± 0.003	+10.85%	0.311 ± 0.002	-5.47%	[0.5207, 0.5212, 0.5206, 0.5197, 0.5211]	<0.001
UNIv2	0.515 ± 0.002	-	0.312 ± 0.002	-	[0.5128, 0.5148, 0.5146, 0.515, 0.5156]	-
UNIv2-SEAL	0.549 ± 0.003	+6.60%	0.299 ± 0.002	-4.17%	[0.5497, 0.55, 0.5487, 0.549, 0.5489]	<0.001
VIRCHOW2	0.499 ± 0.002	-	0.318 ± 0.002	-	[0.4978, 0.4987, 0.4986, 0.498, 0.5001]	-
VIRCHOW2-SEAL	0.575 ± 0.003	+15.23%	0.291 ± 0.002	-8.49%	[0.5754, 0.5759, 0.5742, 0.5749, 0.5748]	<0.001

Extended Data Table 12: **Comparison of 5 Vision-Only vs. SEAL fine-tuned encoders on the Lung Maple-test set.** Results show a linear probe using PCA (256 factors) + Ridge regression for the top 10 highly variable genes (HVGs) across Maple-train lung samples for each encoder. Reported results show the mean and standard deviation across 5 probing folds and p-values calculated across the folds. HVGs: ANKRD42, ADRA2C, URB2, TMEM200B, ARL13B, ISLR, RSF1, RBP4, PDGFRA, LCP1

Method	PCC (\uparrow) (std.)	PCC %	MSE (\downarrow) (std.)	MSE %	PCC folds	p-value
CONCH	0.366 ± 0.002	-	0.575 ± 0.002	-	[0.3646, 0.3657, 0.3649, 0.3676, 0.3649]	-
CONCH-SEAL	0.400 ± 0.002	+9.29%	0.555 ± 0.002	-3.48%	[0.3992, 0.399, 0.4003, 0.4007, 0.4021]	<0.001
H0MINI	0.416 ± 0.002	-	0.539 ± 0.003	-	[0.4164, 0.4157, 0.4157, 0.4159, 0.4161]	-
H0MINI-SEAL	0.443 ± 0.002	+6.49%	0.517 ± 0.003	-4.08%	[0.4439, 0.4442, 0.4427, 0.4437, 0.4426]	<0.001
PHIKON2	0.414 ± 0.002	-	0.543 ± 0.003	-	[0.4151, 0.4145, 0.4133, 0.4144, 0.4135]	-
PHIKON2-SEAL	0.463 ± 0.003	+11.84%	0.507 ± 0.003	-6.63%	[0.4627, 0.465, 0.4641, 0.4622, 0.4628]	<0.001
UNIV2	0.449 ± 0.002	-	0.515 ± 0.003	-	[0.4491, 0.4474, 0.45, 0.448, 0.4479]	-
UNIV2-SEAL	0.496 ± 0.003	+10.47%	0.479 ± 0.002	-6.99%	[0.4944, 0.4981, 0.4944, 0.4983, 0.4963]	<0.001
VIRCHOW2	0.439 ± 0.002	-	0.525 ± 0.002	-	[0.4399, 0.4381, 0.4388, 0.4394, 0.4391]	-
VIRCHOW2-SEAL	0.518 ± 0.002	+18.00%	0.462 ± 0.002	-12.00%	[0.5185, 0.5181, 0.5182, 0.5194, 0.5174]	<0.001

Extended Data Table 13: Full HestBench results using a Ridge regression linear probe of the baseline pathology patch encoders and the finetuned version using SEAL.

Encoder	IDC	PRAD	PAAD	SKCM	COAD	READ	CCRCC	LUAD	LYMPH IDC	Average
Conch	0.5440 ± 0.0750	0.3540 ± 0.0040	0.4450 ± 0.0590	0.6030 ± 0.0500	0.2660 ± 0.0040	0.1660 ± 0.0480	0.2050 ± 0.0300	0.5240 ± 0.0230	0.2530 ± 0.0460	0.3733 ± 0.0377
	0.5480 ± 0.0720	0.3670 ± 0.0090	0.4390 ± 0.0490	0.5930 ± 0.0420	0.2850 ± 0.0070	0.1610 ± 0.0560	0.2040 ± 0.0360	0.5340 ± 0.0210	0.2540 ± 0.0450	0.3761 ± 0.0374
H0mini	0.5900 ± 0.0730	0.3590 ± 0.0370	0.5050 ± 0.0470	0.6190 ± 0.0600	0.2630 ± 0.0270	0.2030 ± 0.0550	0.2640 ± 0.0440	0.5650 ± 0.0320	0.2650 ± 0.0350	0.4037 ± 0.0456
	0.5920 ± 0.0790	0.3840 ± 0.0170	0.5090 ± 0.0500	0.6080 ± 0.0710	0.3010 ± 0.0220	0.1980 ± 0.0580	0.2650 ± 0.0430	0.5590 ± 0.0270	0.2660 ± 0.0340	0.4091 ± 0.0446
Virchow2	0.5950 ± 0.0850	0.3530 ± 0.0380	0.4760 ± 0.0680	0.6430 ± 0.0330	0.2580 ± 0.0330	0.1990 ± 0.0610	0.2700 ± 0.0510	0.5730 ± 0.0150	0.2580 ± 0.0340	0.4028 ± 0.0464
	0.5960 ± 0.0860	0.3610 ± 0.0430	0.4870 ± 0.0610	0.6320 ± 0.0450	0.2690 ± 0.0300	0.2020 ± 0.0610	0.2770 ± 0.0720	0.5690 ± 0.0230	0.2610 ± 0.0280	0.4060 ± 0.0499
Univ2	0.5900 ± 0.0810	0.3570 ± 0.0490	0.5000 ± 0.0400	0.6610 ± 0.0150	0.3020 ± 0.0040	0.2220 ± 0.0380	0.2640 ± 0.0470	0.5590 ± 0.0130	0.2730 ± 0.0400	0.4142 ± 0.0363
	0.5850 ± 0.0710	0.3650 ± 0.0080	0.5210 ± 0.0650	0.6580 ± 0.0470	0.3190 ± 0.0110	0.2160 ± 0.0420	0.2640 ± 0.0330	0.5730 ± 0.0020	0.2660 ± 0.0360	0.4186 ± 0.0350
Gigapath	0.5520 ± 0.0730	0.3760 ± 0.0240	0.4770 ± 0.0500	0.5570 ± 0.0670	0.3000 ± 0.0240	0.1910 ± 0.0660	0.2410 ± 0.0330	0.5430 ± 0.0340	0.2500 ± 0.0550	0.3874 ± 0.0473
	0.5640 ± 0.0740	0.3480 ± 0.0300	0.4880 ± 0.0620	0.5790 ± 0.1200	0.2940 ± 0.0430	0.2000 ± 0.0510	0.2610 ± 0.0310	0.5430 ± 0.0390	0.2590 ± 0.0340	0.3929 ± 0.0538

Extended Data Table 14: **Training data efficiency of patch-level tasks** measured in **Pearson Correlation Coefficient (PCC)** of the **expression prediction** task on different subsets of the training data for **Virchow-v2-SEAL**. All training was done for the same number of SEAL training iterations, such that models trained on 1% of training data experienced the same number of backpropagation steps as those trained on 100%. 0% data represents the vision-only baseline, 100% the final SEAL model.

Training Portion		0%	1%	10%	100%
Brain	Absolute	0.388 \pm 0.003	0.414 \pm 0.010	0.417 \pm 0.010	0.460 \pm 0.003
	Uplift (%)	0.000	6.701	7.474	18.557
Breast	Absolute	0.501 \pm 0.002	0.533 \pm 0.007	0.537 \pm 0.007	0.581 \pm 0.002
	Uplift (%)	0.000	6.387	7.186	15.968
Kidney	Absolute	0.476 \pm 0.002	0.563 \pm 0.006	0.567 \pm 0.006	0.556 \pm 0.002
	Uplift (%)	0.000	18.277	19.118	16.807
Lung	Absolute	0.439 \pm 0.002	0.448 \pm 0.007	0.450 \pm 0.007	0.518 \pm 0.002
	Uplift (%)	0.000	2.050	2.506	17.995
Prostate	Absolute	0.483 \pm 0.002	0.570 \pm 0.007	0.577 \pm 0.008	0.576 \pm 0.002
	Uplift (%)	0.000	18.012	19.462	19.255
Skin	Absolute	0.499 \pm 0.002	0.545 \pm 0.007	0.548 \pm 0.007	0.575 \pm 0.003
	Uplift (%)	0.000	9.218	9.820	15.230

Extended Data Table 15: **Training data efficiency of slide-level tasks** measured in **ROC Area Under Curve (AUC)** of the **mutation status prediction** task on different subsets of the training data for **Virchow-v2-SEAL**. All training was done for the same number of SEAL training iterations, such that models trained on 1% of training data experienced the same number of backpropagation steps as those trained on 100%. 0% data represents the vision-only baseline, 100% the final SEAL model.

Training Portion		0%	1%	10%	100%
BCNB ER	Absolute	0.918 \pm 0.017	0.922 \pm 0.026	0.925 \pm 0.022	0.925 \pm 0.023
	Uplift (%)	0.000	0.436	0.763	0.763
BCNB HER2	Absolute	0.746 \pm 0.054	0.751 \pm 0.025	0.760 \pm 0.024	0.765 \pm 0.015
	Uplift (%)	0.000	0.670	1.877	2.547
BCNB PR	Absolute	0.816 \pm 0.028	0.828 \pm 0.026	0.839 \pm 0.046	0.839 \pm 0.034
	Uplift (%)	0.000	1.471	2.819	2.819
CPTAC COAD KRAS	Absolute	0.606 \pm 0.122	0.621 \pm 0.108	0.655 \pm 0.120	0.673 \pm 0.109
	Uplift (%)	0.000	2.475	8.086	11.056
CPTAC COAD TP53	Absolute	0.664 \pm 0.136	0.610 \pm 0.131	0.636 \pm 0.120	0.717 \pm 0.127
	Uplift (%)	0.000	-8.133	-4.217	7.982

Extended Data Table 16: **Training data efficiency of patch-level tasks** measured in **Pearson Correlation Coefficient (PCC)** of the **expression prediction** task on different subsets of the training data for **Uni-v2-SEAL**. All training was done for the same number of SEAL training iterations, such that models trained on 1% of training data experienced the same number of backpropagation steps as those trained on 100%. 0% data represents the vision-only baseline, 100% the final SEAL model.

Training Portion		0%	1%	10%	100%
Brain	Absolute	0.396 \pm 0.003	0.432 \pm 0.003	0.415 \pm 0.009	0.439 \pm 0.004
	Uplift (%)	0.000	9.091	4.798	10.859
Breast	Absolute	0.506 \pm 0.003	0.555 \pm 0.003	0.535 \pm 0.007	0.557 \pm 0.002
	Uplift (%)	0.000	9.684	5.731	10.079
Kidney	Absolute	0.483 \pm 0.002	0.531 \pm 0.002	0.567 \pm 0.007	0.536 \pm 0.002
	Uplift (%)	0.000	9.938	17.391	10.973
Lung	Absolute	0.449 \pm 0.002	0.491 \pm 0.002	0.450 \pm 0.008	0.496 \pm 0.003
	Uplift (%)	0.000	9.354	0.223	10.468
Prostate	Absolute	0.485 \pm 0.002	0.546 \pm 0.002	0.576 \pm 0.007	0.548 \pm 0.002
	Uplift (%)	0.000	12.577	18.763	12.990
Skin	Absolute	0.515 \pm 0.002	0.549 \pm 0.003	0.547 \pm 0.008	0.549 \pm 0.003
	Uplift (%)	0.000	6.602	6.214	6.602

Extended Data Table 17: **Training data efficiency of slide-level tasks** measured in **ROC Area Under Curve (AUC)** of the **mutation status prediction** task on different subsets of the training data for **Uni-v2-SEAL**. All training was done for the same number of SEAL training iterations, such that models trained on 1% of training data experienced the same number of backpropagation steps as those trained on 100%. 0% data represents the vision-only baseline, 100% the final SEAL model.

Training Portion		0%	1%	10%	100%
BCNB ER	Absolute	0.917 \pm 0.036	0.907 \pm 0.023	0.912 \pm 0.031	0.926 \pm 0.030
	Uplift (%)	0.000	-1.091	-0.545	0.981
BCNB HER2	Absolute	0.765 \pm 0.026	0.758 \pm 0.040	0.765 \pm 0.060	0.771 \pm 0.038
	Uplift (%)	0.000	-0.915	0.000	0.784
BCNB PR	Absolute	0.806 \pm 0.044	0.813 \pm 0.029	0.820 \pm 0.030	0.836 \pm 0.040
	Uplift (%)	0.000	0.868	1.737	3.722
CPTAC COAD KRAS	Absolute	0.676 \pm 0.097	0.674 \pm 0.105	0.661 \pm 0.097	0.675 \pm 0.126
	Uplift (%)	0.000	-0.296	-2.219	-0.148
CPTAC COAD TP53	Absolute	0.720 \pm 0.122	0.683 \pm 0.109	0.725 \pm 0.109	0.708 \pm 0.124
	Uplift (%)	0.000	-5.139	0.694	-1.667

Extended Data Table 18: Performance comparison between SEAL fine-tuned encoders and vision-only baselines on the **BRCA neoadjuvant therapy response** dataset, showing the **ER status classification** task (n=166). This is a slide-level task evaluated using **AUC** across 50 cross-validation folds. The best-performing model for each encoder backbone in **bold**.

Model	ABMIL			MeanMIL		
	AUC (↑)	% change	Sig.	AUC (↑)	% change	Sig.
CONCH	0.626 ± 0.091	-	-	0.602 ± 0.094	-	-
+SEAL	0.651 ± 0.092	+4.0%	*	0.619 ± 0.097	+2.8%	-
H0MINI	0.716 ± 0.097	-	-	0.717 ± 0.092	-	-
+SEAL	0.742 ± 0.090	+3.6%	*	0.701 ± 0.098	-2.2%	-
PHIKON2	0.698 ± 0.100	-	-	0.690 ± 0.096	-	-
+SEAL	0.718 ± 0.081	+2.9%	*	0.718 ± 0.076	+4.1%	-
UNIv2	0.717 ± 0.086	-	-	0.712 ± 0.091	-	-
+SEAL	0.704 ± 0.087	-1.8%	-	0.720 ± 0.091	+1.1%	*
VIRCHOW2	0.682 ± 0.099	-	-	0.690 ± 0.091	-	-
+SEAL	0.724 ± 0.085	+6.2%	**	0.680 ± 0.091	-1.4%	-
Average	0.688 ± 0.095	-	-	0.682 ± 0.093	-	-
+SEAL	0.708 ± 0.087	+2.9%	-	0.688 ± 0.091	+0.8%	-

Extended Data Table 19: Performance comparison between SEAL fine-tuned encoders and vision-only baselines on the **BRCA neoadjuvant therapy response** dataset, showing the **HER2 status classification** task (n=166). This is a slide-level task evaluated using **AUC** across 50 cross-validation folds. The best-performing model for each encoder backbone in **bold**.

Model	ABMIL			MeanMIL		
	AUC (↑)	% change	Sig.	AUC (↑)	% change	Sig.
CONCH	0.645 ± 0.087	-	-	0.683 ± 0.074	-	-
+SEAL	0.656 ± 0.091	+1.7%	-	0.643 ± 0.086	-5.9%	-
H0MINI	0.658 ± 0.091	-	-	0.697 ± 0.063	-	-
+SEAL	0.671 ± 0.088	+2.0%	-	0.704 ± 0.062	+1.0%	*
PHIKON2	0.675 ± 0.086	-	-	0.669 ± 0.072	-	-
+SEAL	0.676 ± 0.087	+0.1%	-	0.676 ± 0.072	+1.0%	*
UNIv2	0.663 ± 0.092	-	-	0.684 ± 0.073	-	-
+SEAL	0.667 ± 0.083	+0.6%	-	0.684 ± 0.072	+0.0%	-
VIRCHOW2	0.639 ± 0.103	-	-	0.679 ± 0.065	-	-
+SEAL	0.660 ± 0.094	+3.3%	-	0.677 ± 0.067	-0.3%	-
Average	0.656 ± 0.092	-	-	0.682 ± 0.069	-	-
+SEAL	0.666 ± 0.089	+1.5%	-	0.677 ± 0.072	-0.8%	-

Extended Data Table 20: Performance comparison between SEAL fine-tuned encoders and vision-only baselines on the **BCNB** dataset, showing the **ER status classification** task (n=1058). This is a slide-level task evaluated using **AUC** across 5 cross-validation folds. The best-performing model for each encoder backbone in **bold**.

Model	ABMIL			MeanMIL		
	AUC (↑)	% change	Sig.	AUC (↑)	% change	Sig.
CONCH	0.866 ± 0.045	-	-	0.816 ± 0.029	-	-
+SEAL	0.891 ± 0.032	+2.9%	-	0.893 ± 0.030	+9.4%	-
H0MINI	0.909 ± 0.036	-	-	0.910 ± 0.022	-	-
+SEAL	0.896 ± 0.038	-1.4%	-	0.923 ± 0.030	+1.4%	-
PHIKON2	0.864 ± 0.037	-	-	0.864 ± 0.035	-	-
+SEAL	0.866 ± 0.024	+0.2%	-	0.862 ± 0.038	-0.2%	-
UNIV2	0.917 ± 0.036	-	-	0.910 ± 0.027	-	-
+SEAL	0.926 ± 0.030	+1.0%	-	0.905 ± 0.029	-0.5%	-
VIRCHOW2	0.918 ± 0.017	-	-	0.924 ± 0.021	-	-
+SEAL	0.925 ± 0.023	+0.8%	-	0.930 ± 0.023	+0.6%	-
Average	0.895 ± 0.034	-	-	0.885 ± 0.027	-	-
+SEAL	0.901 ± 0.029	+0.7%	-	0.903 ± 0.030	+2.0%	-

Extended Data Table 21: Performance comparison between SEAL fine-tuned encoders and vision-only baselines on the **BCNB** dataset, showing the **HER2 status classification** task (n=1058). This is a slide-level task evaluated using **AUC** across 5 cross-validation folds. The best-performing model for each encoder backbone in **bold**.

Model	ABMIL			MeanMIL		
	AUC (↑)	% change	Sig.	AUC (↑)	% change	Sig.
CONCH	0.704 ± 0.024	-	-	0.685 ± 0.026	-	-
+SEAL	0.734 ± 0.021	+4.3%	*	0.756 ± 0.033	+10.4%	**
H0MINI	0.730 ± 0.052	-	-	0.740 ± 0.035	-	-
+SEAL	0.768 ± 0.034	+5.2%	*	0.761 ± 0.043	+2.8%	-
PHIKON2	0.712 ± 0.037	-	-	0.706 ± 0.028	-	-
+SEAL	0.727 ± 0.054	+2.1%	-	0.711 ± 0.038	+0.7%	-
UNIV2	0.765 ± 0.026	-	-	0.736 ± 0.037	-	-
+SEAL	0.771 ± 0.038	+0.8%	-	0.735 ± 0.030	-0.1%	-
VIRCHOW2	0.746 ± 0.054	-	-	0.753 ± 0.016	-	-
+SEAL	0.765 ± 0.015	+2.5%	-	0.754 ± 0.028	+0.1%	-
Average	0.731 ± 0.039	-	-	0.724 ± 0.028	-	-
+SEAL	0.753 ± 0.032	+3.0%	-	0.743 ± 0.034	+2.7%	-

Extended Data Table 22: Performance comparison between SEAL fine-tuned encoders and vision-only baselines on the **BCNB** dataset, showing the **PR status classification** task (n=1058). This is a slide-level task evaluated using **AUC** across 5 cross-validation folds. The best-performing model for each encoder backbone in **bold**.

Model	ABMIL			MeanMIL		
	AUC (↑)	% change	Sig.	AUC (↑)	% change	Sig.
CONCH	0.807 ± 0.054	-	-	0.765 ± 0.056	-	-
+SEAL	0.801 ± 0.036	-0.7%	-	0.843 ± 0.048	+10.2%	-
H0MINI	0.822 ± 0.016	-	-	0.842 ± 0.037	-	-
+SEAL	0.835 ± 0.041	+1.6%	-	0.846 ± 0.045	+0.5%	-
PHIKON2	0.776 ± 0.054	-	-	0.805 ± 0.046	-	-
+SEAL	0.779 ± 0.051	+0.4%	-	0.805 ± 0.042	+0.0%	-
UNIv2	0.806 ± 0.044	-	-	0.848 ± 0.037	-	-
+SEAL	0.836 ± 0.040	+3.7%	**	0.841 ± 0.040	-0.8%	-
VIRCHOW2	0.816 ± 0.028	-	-	0.844 ± 0.037	-	-
+SEAL	0.839 ± 0.034	+2.8%	-	0.856 ± 0.042	+1.4%	*
Average	0.805 ± 0.039	-	-	0.821 ± 0.043	-	-
+SEAL	0.818 ± 0.040	+1.6%	-	0.838 ± 0.043	+2.1%	-

Extended Data Table 23: Performance comparison between SEAL fine-tuned encoders and vision-only baselines on the **CPTAC BRCA** dataset, showing the **PIK3CA mutation classification** task (n=112). This is a slide-level task evaluated using **AUC** across 50 cross-validation folds. The best-performing model for each encoder backbone in **bold**.

Model	ABMIL			MeanMIL		
	AUC (↑)	% change	Sig.	AUC (↑)	% change	Sig.
CONCH	0.545 ± 0.116	-	-	0.526 ± 0.131	-	-
+SEAL	0.553 ± 0.113	+1.5%	-	0.511 ± 0.116	-2.9%	-
H0MINI	0.598 ± 0.123	-	-	0.570 ± 0.107	-	-
+SEAL	0.554 ± 0.115	-7.4%	-	0.574 ± 0.108	+0.7%	-
PHIKON2	0.555 ± 0.114	-	-	0.556 ± 0.111	-	-
+SEAL	0.554 ± 0.116	-0.2%	-	0.544 ± 0.103	-2.2%	-
UNIv2	0.595 ± 0.103	-	-	0.544 ± 0.120	-	-
+SEAL	0.575 ± 0.099	-3.4%	-	0.524 ± 0.115	-3.7%	-
VIRCHOW2	0.533 ± 0.129	-	-	0.545 ± 0.116	-	-
+SEAL	0.544 ± 0.133	+2.1%	-	0.518 ± 0.117	-5.0%	-
Average	0.565 ± 0.117	-	-	0.548 ± 0.117	-	-
+SEAL	0.556 ± 0.115	-1.6%	-	0.534 ± 0.112	-2.6%	-

Extended Data Table 24: Performance comparison between SEAL fine-tuned encoders and vision-only baselines on the **CPTAC BRCA** dataset, showing the **TP53 Mutation classification** task (n=112). This is a slide-level task evaluated using **AUC** across 50 cross-validation folds. The best-performing model for each encoder backbone in **bold**.

Model	ABMIL			MeanMIL		
	AUC (↑)	% change	Sig.	AUC (↑)	% change	Sig.
CONCH	0.792 ± 0.103	-	-	0.794 ± 0.096	-	-
+SEAL	0.824 ± 0.093	+4.0%	**	0.812 ± 0.093	+2.3%	**
H0MINI	0.801 ± 0.096	-	-	0.775 ± 0.088	-	-
+SEAL	0.814 ± 0.085	+1.6%	-	0.781 ± 0.098	+0.8%	-
PHIKON2	0.834 ± 0.079	-	-	0.822 ± 0.091	-	-
+SEAL	0.849 ± 0.074	+1.8%	**	0.826 ± 0.086	+0.5%	*
UNIv2	0.801 ± 0.093	-	-	0.787 ± 0.088	-	-
+SEAL	0.820 ± 0.090	+2.4%	**	0.779 ± 0.092	-1.0%	-
VIRCHOW2	0.772 ± 0.084	-	-	0.754 ± 0.095	-	-
+SEAL	0.813 ± 0.090	+5.3%	-	0.773 ± 0.092	+2.5%	*
Average	0.800 ± 0.091	-	-	0.786 ± 0.092	-	-
+SEAL	0.824 ± 0.086	+3.0%	-	0.794 ± 0.092	+1.0%	-

Extended Data Table 25: Performance comparison between SEAL fine-tuned encoders and vision-only baselines on the **CPTAC CCRCC** dataset, showing the **BAP1 mutation classification** task (n=218). This is a slide-level task evaluated using **AUC** across 50 cross-validation folds. The best-performing model for each encoder backbone in **bold**.

Model	ABMIL			MeanMIL		
	AUC (↑)	% change	Sig.	AUC (↑)	% change	Sig.
CONCH	0.658 ± 0.157	-	-	0.689 ± 0.141	-	-
+SEAL	0.728 ± 0.139	+10.6%	-	0.709 ± 0.126	+2.9%	-
H0MINI	0.727 ± 0.126	-	-	0.631 ± 0.139	-	-
+SEAL	0.707 ± 0.145	-2.8%	-	0.700 ± 0.136	+10.9%	-
PHIKON2	0.620 ± 0.155	-	-	0.642 ± 0.152	-	-
+SEAL	0.613 ± 0.163	-1.1%	-	0.649 ± 0.148	+1.1%	-
UNIv2	0.693 ± 0.150	-	-	0.720 ± 0.145	-	-
+SEAL	0.685 ± 0.172	-1.2%	-	0.715 ± 0.161	-0.7%	-
VIRCHOW2	0.712 ± 0.135	-	-	0.614 ± 0.142	-	-
+SEAL	0.738 ± 0.132	+3.7%	-	0.705 ± 0.104	+14.8%	-
Average	0.682 ± 0.145	-	-	0.659 ± 0.144	-	-
+SEAL	0.694 ± 0.150	+1.8%	-	0.696 ± 0.135	+5.5%	-

Extended Data Table 26: Performance comparison between SEAL fine-tuned encoders and vision-only baselines on the **CPTAC CCRCC** dataset, showing the **VHL mutation classification** task (n=218). This is a slide-level task evaluated using **AUC** across 50 cross-validation folds. The best-performing model for each encoder backbone in **bold**.

Model	ABMIL			MeanMIL		
	AUC (↑)	% change	Sig.	AUC (↑)	% change	Sig.
CONCH	0.564 ± 0.136	-	-	0.606 ± 0.115	-	-
+SEAL	0.537 ± 0.129	-4.8%	-	0.585 ± 0.119	-3.5%	-
H0MINI	0.543 ± 0.121	-	-	0.574 ± 0.129	-	-
+SEAL	0.567 ± 0.124	+4.4%	-	0.621 ± 0.146	+8.2%	-
PHIKON2	0.454 ± 0.136	-	-	0.511 ± 0.135	-	-
+SEAL	0.443 ± 0.143	-2.4%	-	0.515 ± 0.141	+0.8%	-
UNIv2	0.538 ± 0.128	-	-	0.542 ± 0.133	-	-
+SEAL	0.533 ± 0.127	-0.9%	-	0.564 ± 0.131	+4.1%	-
VIRCHOW2	0.580 ± 0.135	-	-	0.588 ± 0.136	-	-
+SEAL	0.607 ± 0.129	+4.7%	*	0.612 ± 0.133	+4.1%	*
Average	0.536 ± 0.131	-	-	0.564 ± 0.130	-	-
+SEAL	0.537 ± 0.130	+0.3%	-	0.579 ± 0.134	+2.7%	-

Extended Data Table 27: Performance comparison between SEAL fine-tuned encoders and vision-only baselines on the **CPTAC COAD** dataset, showing the **KRAS mutation classification** task (n=97). This is a slide-level task evaluated using **AUC** across 50 cross-validation folds. The best-performing model for each encoder backbone in **bold**.

Model	ABMIL			MeanMIL		
	AUC (↑)	% change	Sig.	AUC (↑)	% change	Sig.
CONCH	0.598 ± 0.110	-	-	0.678 ± 0.108	-	-
+SEAL	0.666 ± 0.111	+11.4%	-	0.685 ± 0.105	+1.0%	-
H0MINI	0.669 ± 0.108	-	-	0.647 ± 0.118	-	-
+SEAL	0.635 ± 0.095	-5.1%	-	0.666 ± 0.113	+2.9%	*
PHIKON2	0.696 ± 0.109	-	-	0.626 ± 0.105	-	-
+SEAL	0.684 ± 0.099	-1.7%	-	0.634 ± 0.106	+1.3%	*
UNIv2	0.676 ± 0.097	-	-	0.671 ± 0.101	-	-
+SEAL	0.675 ± 0.126	-0.1%	-	0.674 ± 0.104	+0.4%	-
VIRCHOW2	0.606 ± 0.122	-	-	0.636 ± 0.110	-	-
+SEAL	0.673 ± 0.109	+11.1%	-	0.660 ± 0.101	+3.8%	-
Average	0.649 ± 0.109	-	-	0.652 ± 0.108	-	-
+SEAL	0.667 ± 0.108	+2.7%	-	0.664 ± 0.106	+1.9%	-

Extended Data Table 28: Performance comparison between SEAL fine-tuned encoders and vision-only baselines on the **CPTAC COAD** dataset, showing the **TP53 Mutation classification** task (n=97). This is a slide-level task evaluated using **AUC** across 50 cross-validation folds. The best-performing model for each encoder backbone in **bold**.

Model	ABMIL			MeanMIL		
	AUC (↑)	% change	Sig.	AUC (↑)	% change	Sig.
CONCH	0.643 ± 0.132	-	-	0.654 ± 0.134	-	-
+SEAL	0.638 ± 0.134	-0.8%	-	0.595 ± 0.135	-9.0%	-
H0MINI	0.686 ± 0.118	-	-	0.678 ± 0.143	-	-
+SEAL	0.715 ± 0.115	+4.2%	*	0.711 ± 0.133	+4.9%	**
PHIKON2	0.718 ± 0.105	-	-	0.665 ± 0.135	-	-
+SEAL	0.738 ± 0.100	+2.8%	**	0.686 ± 0.127	+3.2%	-
UNIV2	0.720 ± 0.122	-	-	0.738 ± 0.117	-	-
+SEAL	0.708 ± 0.124	-1.7%	-	0.741 ± 0.122	+0.4%	-
VIRCHOW2	0.664 ± 0.136	-	-	0.679 ± 0.115	-	-
+SEAL	0.717 ± 0.127	+8.0%	**	0.744 ± 0.117	+9.6%	-
Average	0.686 ± 0.123	-	-	0.683 ± 0.129	-	-
+SEAL	0.703 ± 0.120	+2.5%	-	0.695 ± 0.127	+1.8%	-

Extended Data Table 29: Performance comparison between SEAL fine-tuned encoders and vision-only baselines on the **CPTAC GBM** dataset, showing the **EGFR mutation classification** task (n=243). This is a slide-level task evaluated using **AUC** across 50 cross-validation folds. The best-performing model for each encoder backbone in **bold**.

Model	ABMIL			MeanMIL		
	AUC (↑)	% change	Sig.	AUC (↑)	% change	Sig.
CONCH	0.633 ± 0.136	-	-	0.606 ± 0.093	-	-
+SEAL	0.651 ± 0.127	+2.8%	-	0.623 ± 0.103	+2.8%	*
H0MINI	0.579 ± 0.122	-	-	0.549 ± 0.121	-	-
+SEAL	0.617 ± 0.119	+6.6%	**	0.622 ± 0.113	+13.3%	-
PHIKON2	0.510 ± 0.127	-	-	0.527 ± 0.104	-	-
+SEAL	0.600 ± 0.127	+17.6%	-	0.528 ± 0.106	+0.2%	-
UNIV2	0.557 ± 0.132	-	-	0.558 ± 0.113	-	-
+SEAL	0.574 ± 0.142	+3.1%	-	0.553 ± 0.108	-0.9%	-
VIRCHOW2	0.615 ± 0.124	-	-	0.572 ± 0.114	-	-
+SEAL	0.625 ± 0.128	+1.6%	-	0.604 ± 0.110	+5.6%	-
Average	0.579 ± 0.128	-	-	0.562 ± 0.109	-	-
+SEAL	0.613 ± 0.129	+6.0%	-	0.586 ± 0.108	+4.2%	-

Extended Data Table 30: Performance comparison between SEAL fine-tuned encoders and vision-only baselines on the **CPTAC GBM** dataset, showing the **TP53 Mutation classification** task (n=243). This is a slide-level task evaluated using **AUC** across 50 cross-validation folds. The best-performing model for each encoder backbone in **bold**.

Model	ABMIL			MeanMIL		
	AUC (↑)	% change	Sig.	AUC (↑)	% change	Sig.
CONCH	0.828 ± 0.084	-	-	0.705 ± 0.119	-	-
+SEAL	0.812 ± 0.107	-1.9%	-	0.757 ± 0.121	+7.4%	-
H0MINI	0.832 ± 0.101	-	-	0.803 ± 0.100	-	-
+SEAL	0.799 ± 0.125	-4.0%	-	0.785 ± 0.103	-2.2%	-
PHIKON2	0.763 ± 0.108	-	-	0.686 ± 0.130	-	-
+SEAL	0.777 ± 0.105	+1.8%	*	0.708 ± 0.116	+3.2%	-
UNIv2	0.763 ± 0.112	-	-	0.808 ± 0.093	-	-
+SEAL	0.797 ± 0.110	+4.5%	**	0.793 ± 0.094	-1.9%	-
VIRCHOW2	0.745 ± 0.119	-	-	0.759 ± 0.109	-	-
+SEAL	0.761 ± 0.114	+2.1%	-	0.775 ± 0.087	+2.1%	-
Average	0.786 ± 0.105	-	-	0.752 ± 0.110	-	-
+SEAL	0.789 ± 0.112	+0.4%	-	0.764 ± 0.104	+1.5%	-

Extended Data Table 31: Performance comparison between SEAL fine-tuned encoders and vision-only baselines on the **CPTAC LUAD** dataset, showing the **EGFR mutation classification** task (n=324). This is a slide-level task evaluated using **AUC** across 50 cross-validation folds. The best-performing model for each encoder backbone in **bold**.

Model	ABMIL			MeanMIL		
	AUC (↑)	% change	Sig.	AUC (↑)	% change	Sig.
CONCH	0.769 ± 0.091	-	-	0.810 ± 0.094	-	-
+SEAL	0.732 ± 0.121	-4.8%	-	0.762 ± 0.111	-5.9%	-
H0MINI	0.797 ± 0.094	-	-	0.796 ± 0.101	-	-
+SEAL	0.793 ± 0.106	-0.5%	-	0.776 ± 0.107	-2.5%	-
PHIKON2	0.728 ± 0.100	-	-	0.712 ± 0.096	-	-
+SEAL	0.745 ± 0.092	+2.3%	*	0.727 ± 0.093	+2.1%	**
UNIv2	0.830 ± 0.089	-	-	0.777 ± 0.099	-	-
+SEAL	0.815 ± 0.110	-1.8%	-	0.777 ± 0.096	+0.0%	-
VIRCHOW2	0.822 ± 0.089	-	-	0.819 ± 0.097	-	-
+SEAL	0.786 ± 0.105	-4.4%	-	0.802 ± 0.099	-2.1%	-
Average	0.789 ± 0.093	-	-	0.783 ± 0.097	-	-
+SEAL	0.774 ± 0.107	-1.9%	-	0.769 ± 0.101	-1.8%	-

Extended Data Table 32: Performance comparison between SEAL fine-tuned encoders and vision-only baselines on the **CPTAC LUAD** dataset, showing the **STK11 Mutation classification** task (n=324). This is a slide-level task evaluated using **AUC** across 50 cross-validation folds. The best-performing model for each encoder backbone in **bold**.

ABMIL				MeanMIL		
Model	AUC (↑)	% change	Sig.	AUC (↑)	% change	Sig.
CONCH	0.866 ± 0.093	-	-	0.861 ± 0.103	-	-
+SEAL	0.827 ± 0.110	-4.5%	-	0.831 ± 0.127	-3.5%	-
H0MINI	0.886 ± 0.072	-	-	0.869 ± 0.076	-	-
+SEAL	0.901 ± 0.060	+1.7%	*	0.877 ± 0.080	+0.9%	*
PHIKON2	0.884 ± 0.070	-	-	0.847 ± 0.084	-	-
+SEAL	0.876 ± 0.071	-0.9%	-	0.844 ± 0.082	-0.4%	-
UNIv2	0.908 ± 0.052	-	-	0.873 ± 0.072	-	-
+SEAL	0.907 ± 0.063	-0.1%	-	0.866 ± 0.079	-0.8%	-
VIRCHOW2	0.809 ± 0.104	-	-	0.845 ± 0.099	-	-
+SEAL	0.835 ± 0.090	+3.2%	*	0.871 ± 0.081	+3.1%	-
Average	0.871 ± 0.078	-	-	0.859 ± 0.087	-	-
+SEAL	0.869 ± 0.079	-0.2%	-	0.858 ± 0.090	-0.1%	-

Extended Data Table 33: Performance comparison between SEAL fine-tuned encoders and vision-only baselines on the **CPTAC LUAD** dataset, showing the **TP53 Mutation classification** task (n=324). This is a slide-level task evaluated using **AUC** across 50 cross-validation folds. The best-performing model for each encoder backbone in **bold**.

ABMIL				MeanMIL		
Model	AUC (↑)	% change	Sig.	AUC (↑)	% change	Sig.
CONCH	0.681 ± 0.115	-	-	0.705 ± 0.095	-	-
+SEAL	0.698 ± 0.114	+2.5%	-	0.736 ± 0.102	+4.4%	-
H0MINI	0.736 ± 0.099	-	-	0.741 ± 0.078	-	-
+SEAL	0.752 ± 0.097	+2.2%	-	0.761 ± 0.086	+2.7%	**
PHIKON2	0.687 ± 0.113	-	-	0.683 ± 0.117	-	-
+SEAL	0.670 ± 0.113	-2.5%	-	0.685 ± 0.113	+0.3%	-
UNIv2	0.751 ± 0.102	-	-	0.735 ± 0.102	-	-
+SEAL	0.753 ± 0.113	+0.3%	-	0.753 ± 0.093	+2.4%	**
VIRCHOW2	0.785 ± 0.082	-	-	0.771 ± 0.086	-	-
+SEAL	0.788 ± 0.099	+0.4%	-	0.778 ± 0.095	+0.9%	-
Average	0.728 ± 0.102	-	-	0.727 ± 0.096	-	-
+SEAL	0.732 ± 0.107	+0.6%	-	0.743 ± 0.098	+2.1%	-

Extended Data Table 34: Performance comparison between SEAL fine-tuned encoders and vision-only baselines on the **MUT-HET-RCC** dataset, showing the **PBRM1 mutation classification** task (n=1291). This is a slide-level task evaluated using **AUC** across 5 cross-validation folds. The best-performing model for each encoder backbone in **bold**.

ABMIL				MeanMIL		
Model	AUC (↑)	% change	Sig.	AUC (↑)	% change	Sig.
CONCH	0.791 ± 0.036	-	-	0.762 ± 0.017	-	-
+SEAL	0.798 ± 0.027	+0.9%	-	0.763 ± 0.023	+0.1%	-
H0MINI	0.819 ± 0.027	-	-	0.796 ± 0.046	-	-
+SEAL	0.836 ± 0.021	+2.1%	-	0.809 ± 0.024	+1.6%	-
PHIKON2	0.804 ± 0.047	-	-	0.798 ± 0.023	-	-
+SEAL	0.813 ± 0.013	+1.1%	-	0.799 ± 0.024	+0.1%	-
UNIv2	0.840 ± 0.035	-	-	0.820 ± 0.029	-	-
+SEAL	0.847 ± 0.065	+0.8%	-	0.823 ± 0.033	+0.4%	-
VIRCHOW2	0.822 ± 0.040	-	-	0.794 ± 0.031	-	-
+SEAL	0.829 ± 0.027	+0.9%	-	0.806 ± 0.032	+1.5%	*
Average	0.815 ± 0.037	-	-	0.794 ± 0.029	-	-
+SEAL	0.825 ± 0.031	+1.2%	-	0.800 ± 0.027	+0.8%	-

Extended Data Table 35: Performance comparison between SEAL fine-tuned encoders and vision-only baselines on the **MUT-HET-RCC** dataset, showing the **SETD2 mutation classification** task (n=1291). This is a slide-level task evaluated using **AUC** across 5 cross-validation folds. The best-performing model for each encoder backbone in **bold**.

ABMIL				MeanMIL		
Model	AUC (↑)	% change	Sig.	AUC (↑)	% change	Sig.
CONCH	0.697 ± 0.028	-	-	0.712 ± 0.027	-	-
+SEAL	0.724 ± 0.019	+3.9%	*	0.721 ± 0.019	+1.3%	-
H0MINI	0.690 ± 0.026	-	-	0.691 ± 0.035	-	-
+SEAL	0.742 ± 0.027	+7.5%	**	0.729 ± 0.028	+5.5%	*
PHIKON2	0.702 ± 0.044	-	-	0.723 ± 0.026	-	-
+SEAL	0.725 ± 0.044	+3.3%	-	0.725 ± 0.025	+0.3%	-
UNIv2	0.713 ± 0.034	-	-	0.711 ± 0.030	-	-
+SEAL	0.716 ± 0.018	+0.4%	-	0.704 ± 0.024	-1.0%	-
VIRCHOW2	0.718 ± 0.016	-	-	0.700 ± 0.021	-	-
+SEAL	0.750 ± 0.014	+4.5%	**	0.718 ± 0.028	+2.6%	-
Average	0.704 ± 0.030	-	-	0.707 ± 0.028	-	-
+SEAL	0.731 ± 0.024	+3.9%	-	0.719 ± 0.025	+1.7%	-

Extended Data Table 36: Performance comparison between SEAL fine-tuned encoders and vision-only baselines on the **CPTAC COAD** dataset, showing the **Microsatellite Instability classification** task (n=97). This is a slide-level task evaluated using **AUC** across 50 cross-validation folds. The best-performing model for each encoder backbone in **bold**.

Model	ABMIL			MeanMIL		
	AUC (↑)	% change	Sig.	AUC (↑)	% change	Sig.
CONCH	0.805 ± 0.109	-	-	0.844 ± 0.096	-	-
+SEAL	0.798 ± 0.125	-0.9%	-	0.837 ± 0.110	-0.8%	-
H0MINI	0.877 ± 0.081	-	-	0.905 ± 0.079	-	-
+SEAL	0.886 ± 0.079	+1.0%	-	0.908 ± 0.085	+0.3%	-
PHIKON2	0.808 ± 0.098	-	-	0.805 ± 0.122	-	-
+SEAL	0.814 ± 0.099	+0.7%	-	0.818 ± 0.119	+1.6%	-
UNIv2	0.879 ± 0.072	-	-	0.883 ± 0.097	-	-
+SEAL	0.877 ± 0.082	-0.2%	-	0.883 ± 0.097	+0.0%	-
VIRCHOW2	0.831 ± 0.135	-	-	0.858 ± 0.092	-	-
+SEAL	0.894 ± 0.072	+7.6%	-	0.901 ± 0.066	+5.0%	-
Average	0.840 ± 0.099	-	-	0.859 ± 0.097	-	-
+SEAL	0.854 ± 0.091	+1.6%	-	0.869 ± 0.095	+1.2%	-

Extended Data Table 37: Performance comparison between SEAL fine-tuned encoders and vision-only baselines on the **BRCA neoadjuvant therapy response** dataset, showing the **subtype classification** task (n=166). This is a slide-level task evaluated using **AUC** across 50 cross-validation folds. The best-performing model for each encoder backbone in **bold**.

Model	ABMIL			MeanMIL		
	AUC (↑)	% change	Sig.	AUC (↑)	% change	Sig.
CONCH	0.711 ± 0.082	-	-	0.733 ± 0.060	-	-
+SEAL	0.735 ± 0.071	+3.4%	**	0.743 ± 0.062	+1.4%	*
H0MINI	0.737 ± 0.085	-	-	0.718 ± 0.061	-	-
+SEAL	0.757 ± 0.078	+2.7%	*	0.727 ± 0.062	+1.3%	**
PHIKON2	0.729 ± 0.093	-	-	0.717 ± 0.058	-	-
+SEAL	0.736 ± 0.078	+1.0%	-	0.735 ± 0.059	+2.5%	-
UNIv2	0.770 ± 0.066	-	-	0.751 ± 0.058	-	-
+SEAL	0.768 ± 0.078	-0.3%	-	0.747 ± 0.059	-0.5%	-
VIRCHOW2	0.749 ± 0.074	-	-	0.735 ± 0.066	-	-
+SEAL	0.745 ± 0.075	-0.5%	-	0.742 ± 0.063	+1.0%	-
Average	0.739 ± 0.080	-	-	0.731 ± 0.061	-	-
+SEAL	0.748 ± 0.076	+1.2%	-	0.739 ± 0.061	+1.1%	-

Extended Data Table 38: Performance comparison between SEAL fine-tuned encoders and vision-only baselines on the **NSCLC** dataset, showing the **PDL1 expression regression** task (n=217). This is a slide-level task evaluated using **KAPPA** across 5 cross-validation folds. The best-performing model for each encoder backbone in **bold**.

Model	ABMIL			MeanMIL		
	KAPPA (↑)	% change	Sig.	KAPPA (↑)	% change	Sig.
CONCH	0.823 ± 0.051	-	-	0.595 ± 0.073	-	-
+SEAL	0.752 ± 0.068	-8.6%	-	0.662 ± 0.089	+11.3%	*
H0MINI	0.773 ± 0.068	-	-	0.616 ± 0.147	-	-
+SEAL	0.802 ± 0.063	+3.8%	**	0.643 ± 0.140	+4.4%	-
PHIKON2	0.829 ± 0.038	-	-	0.617 ± 0.059	-	-
+SEAL	0.815 ± 0.058	-1.7%	-	0.620 ± 0.081	+0.5%	-
UNIv2	0.865 ± 0.042	-	-	0.578 ± 0.098	-	-
+SEAL	0.869 ± 0.058	+0.5%	-	0.622 ± 0.092	+7.6%	**
VIRCHOW2	0.856 ± 0.052	-	-	0.701 ± 0.124	-	-
+SEAL	0.819 ± 0.085	-4.3%	-	0.625 ± 0.087	-10.8%	-
Average	0.829 ± 0.050	-	-	0.621 ± 0.100	-	-
+SEAL	0.811 ± 0.066	-2.1%	-	0.634 ± 0.098	+2.1%	-

Extended Data Table 39: Performance comparison between SEAL fine-tuned encoders and vision-only baselines on the **ovarian treatment response** dataset, showing the **treatment response classification** task (n=85). This is a slide-level task evaluated using **AUC** across 10 cross-validation folds. The best-performing model for each encoder backbone in **bold**.

Model	ABMIL			MeanMIL		
	AUC (↑)	% change	Sig.	AUC (↑)	% change	Sig.
CONCH	0.700 ± 0.245	-	-	0.667 ± 0.183	-	-
+SEAL	0.717 ± 0.252	+2.4%	-	0.783 ± 0.183	+17.4%	*
H0MINI	0.367 ± 0.194	-	-	0.500 ± 0.211	-	-
+SEAL	0.450 ± 0.269	+22.6%	-	0.667 ± 0.197	+33.4%	**
PHIKON2	0.283 ± 0.269	-	-	0.383 ± 0.325	-	-
+SEAL	0.317 ± 0.252	+12.0%	-	0.467 ± 0.364	+21.9%	-
UNIv2	0.433 ± 0.226	-	-	0.650 ± 0.273	-	-
+SEAL	0.617 ± 0.211	+42.5%	*	0.650 ± 0.157	+0.0%	-
VIRCHOW2	0.450 ± 0.279	-	-	0.550 ± 0.130	-	-
+SEAL	0.483 ± 0.174	+7.3%	-	0.717 ± 0.167	+30.4%	**
Average	0.447 ± 0.243	-	-	0.550 ± 0.224	-	-
+SEAL	0.517 ± 0.232	+15.7%	-	0.657 ± 0.214	+19.4%	-

Extended Data Table 40: Performance comparison between SEAL fine-tuned encoders and vision-only baselines on the **SurGen** dataset, showing the **overall survival** task (n=387). This is a slide-level task evaluated using **CINDEX** across 5 cross-validation folds. The best-performing model for each encoder backbone in **bold**.

Model	ABMIL			MeanMIL		
	CINDEX (\uparrow)	% change	Sig.	CINDEX (\uparrow)	% change	Sig.
CONCH	0.622 \pm 0.074	-	-	0.651 \pm 0.046	-	-
+SEAL	0.678 \pm 0.051	+9.0%	-	0.660 \pm 0.068	+1.4%	-
H0MINI	0.577 \pm 0.083	-	-	0.639 \pm 0.085	-	-
+SEAL	0.609 \pm 0.040	+5.5%	-	0.659 \pm 0.078	+3.1%	*
PHIKON2	0.630 \pm 0.065	-	-	0.640 \pm 0.053	-	-
+SEAL	0.634 \pm 0.069	+0.6%	-	0.609 \pm 0.059	-4.8%	-
UNIv2	0.620 \pm 0.071	-	-	0.641 \pm 0.089	-	-
+SEAL	0.623 \pm 0.067	+0.5%	-	0.665 \pm 0.076	+3.7%	-
VIRCHOW2	0.626 \pm 0.064	-	-	0.644 \pm 0.094	-	-
+SEAL	0.644 \pm 0.089	+2.9%	-	0.688 \pm 0.065	+6.8%	*
Average	0.615 \pm 0.071	-	-	0.643 \pm 0.073	-	-
+SEAL	0.638 \pm 0.063	+3.7%	-	0.656 \pm 0.069	+2.1%	-

Extended Data Table 41: Performance comparison between SEAL fine-tuned encoders and vision-only baselines on the **CPTAC BRCA** dataset, showing the **Epithelial-Mesenchymal Transition Pathway regression** task (n=112). This is a slide-level task evaluated using **PCC** across 10 cross-validation folds. The best-performing model for each encoder backbone in **bold**.

Model	ABMIL			MeanMIL		
	PCC (\uparrow)	% change	Sig.	PCC (\uparrow)	% change	Sig.
CONCH	0.660 \pm 0.088	-	-	-0.128 \pm 0.241	-	-
+SEAL	0.578 \pm 0.130	-12.4%	-	-0.141 \pm 0.224	+10.2%	-
H0MINI	0.648 \pm 0.135	-	-	0.025 \pm 0.309	-	-
+SEAL	0.655 \pm 0.140	+1.1%	-	0.003 \pm 0.271	-88.0%	-
PHIKON2	0.357 \pm 0.258	-	-	0.052 \pm 0.208	-	-
+SEAL	0.542 \pm 0.198	+51.8%	*	0.073 \pm 0.220	+40.4%	-
UNIv2	0.657 \pm 0.105	-	-	-0.047 \pm 0.294	-	-
+SEAL	0.673 \pm 0.097	+2.4%	-	0.000 \pm 0.207	-100.0%	-
VIRCHOW2	0.655 \pm 0.110	-	-	0.642 \pm 0.105	-	-
+SEAL	0.723 \pm 0.067	+10.4%	*	0.485 \pm 0.151	-24.5%	-
Average	0.595 \pm 0.139	-	-	0.109 \pm 0.231	-	-
+SEAL	0.634 \pm 0.126	+6.5%	-	0.084 \pm 0.215	-22.8%	-

Extended Data Table 42: Performance comparison between SEAL fine-tuned encoders and vision-only baselines on the **CPTAC BRCA** dataset, showing the **G2/M Checkpoint Pathway regression** task (n=112). This is a slide-level task evaluated using **PCC** across 10 cross-validation folds. The best-performing model for each encoder backbone in **bold**.

Model	ABMIL			MeanMIL		
	PCC (↑)	% change	Sig.	PCC (↑)	% change	Sig.
CONCH	0.580 ± 0.143	-	-	0.087 ± 0.317	-	-
+SEAL	0.668 ± 0.105	+15.2%	-	0.218 ± 0.311	+150.6%	-
H0MINI	0.606 ± 0.118	-	-	-0.094 ± 0.233	-	-
+SEAL	0.649 ± 0.093	+7.1%	*	-0.079 ± 0.227	-16.0%	-
PHIKON2	0.321 ± 0.195	-	-	-0.027 ± 0.348	-	-
+SEAL	0.529 ± 0.149	+64.8%	-	-0.048 ± 0.370	+77.8%	-
UNIv2	0.565 ± 0.147	-	-	-0.020 ± 0.285	-	-
+SEAL	0.628 ± 0.143	+11.2%	**	-0.030 ± 0.290	+50.0%	-
VIRCHOW2	0.619 ± 0.114	-	-	0.605 ± 0.126	-	-
+SEAL	0.678 ± 0.081	+9.5%	*	0.601 ± 0.140	-0.7%	-
Average	0.538 ± 0.143	-	-	0.110 ± 0.262	-	-
+SEAL	0.630 ± 0.114	+17.1%	-	0.132 ± 0.268	+20.1%	-

Extended Data Table 43: Performance comparison between SEAL fine-tuned encoders and vision-only baselines on the **CPTAC BRCA** dataset, showing the **Upregulated genes in PI3K/AKT/mTOR signaling Pathway regression** task (n=112). This is a slide-level task evaluated using **PCC** across 10 cross-validation folds. The best-performing model for each encoder backbone in **bold**.

Model	ABMIL			MeanMIL		
	PCC (↑)	% change	Sig.	PCC (↑)	% change	Sig.
CONCH	0.332 ± 0.220	-	-	0.019 ± 0.280	-	-
+SEAL	0.410 ± 0.196	+23.5%	*	-0.037 ± 0.273	-294.7%	-
H0MINI	0.279 ± 0.210	-	-	0.018 ± 0.195	-	-
+SEAL	0.348 ± 0.229	+24.7%	**	0.023 ± 0.193	+27.8%	-
PHIKON2	0.304 ± 0.213	-	-	0.009 ± 0.297	-	-
+SEAL	0.149 ± 0.199	-51.0%	-	0.004 ± 0.285	-55.6%	-
UNIv2	0.416 ± 0.105	-	-	0.019 ± 0.300	-	-
+SEAL	0.398 ± 0.151	-4.3%	-	0.059 ± 0.342	+210.5%	-
VIRCHOW2	0.392 ± 0.145	-	-	0.355 ± 0.131	-	-
+SEAL	0.513 ± 0.184	+30.9%	**	0.332 ± 0.232	-6.5%	-
Average	0.345 ± 0.179	-	-	0.084 ± 0.241	-	-
+SEAL	0.364 ± 0.192	+5.5%	-	0.076 ± 0.265	-9.3%	-

Extended Data Table 44: Performance comparison between SEAL fine-tuned encoders and vision-only baselines on the **CPTAC COAD** dataset, showing the **Epithelial-Mesenchymal Transition Pathway regression** task (n=97). This is a slide-level task evaluated using **PCC** across 10 cross-validation folds. The best-performing model for each encoder backbone in **bold**.

Model	ABMIL			MeanMIL		
	PCC (\uparrow)	% change	Sig.	PCC (\uparrow)	% change	Sig.
CONCH	0.740 \pm 0.081	-	-	0.731 \pm 0.100	-	-
+SEAL	0.778 \pm 0.065	+5.1%	-	0.752 \pm 0.054	+2.9%	-
H0MINI	0.725 \pm 0.112	-	-	0.767 \pm 0.087	-	-
+SEAL	0.750 \pm 0.099	+3.4%	-	0.778 \pm 0.091	+1.4%	-
PHIKON2	0.293 \pm 0.241	-	-	-0.056 \pm 0.313	-	-
+SEAL	0.488 \pm 0.213	+66.6%	-	-0.070 \pm 0.327	+25.0%	-
UNIv2	0.767 \pm 0.072	-	-	0.751 \pm 0.076	-	-
+SEAL	0.771 \pm 0.072	+0.5%	-	0.768 \pm 0.085	+2.3%	-
VIRCHOW2	0.734 \pm 0.108	-	-	0.765 \pm 0.096	-	-
+SEAL	0.772 \pm 0.088	+5.2%	-	0.677 \pm 0.119	-11.5%	-
Average	0.652 \pm 0.123	-	-	0.592 \pm 0.134	-	-
+SEAL	0.712 \pm 0.107	+9.2%	-	0.581 \pm 0.135	-1.8%	-

Extended Data Table 45: Performance comparison between SEAL fine-tuned encoders and vision-only baselines on the **CPTAC COAD** dataset, showing the **G2/M Checkpoint Pathway regression** task (n=97). This is a slide-level task evaluated using **PCC** across 10 cross-validation folds. The best-performing model for each encoder backbone in **bold**.

Model	ABMIL			MeanMIL		
	PCC (\uparrow)	% change	Sig.	PCC (\uparrow)	% change	Sig.
CONCH	0.201 \pm 0.147	-	-	0.169 \pm 0.200	-	-
+SEAL	0.301 \pm 0.206	+49.8%	**	0.272 \pm 0.237	+60.9%	*
H0MINI	0.327 \pm 0.206	-	-	0.290 \pm 0.236	-	-
+SEAL	0.441 \pm 0.183	+34.9%	**	0.316 \pm 0.261	+9.0%	-
PHIKON2	0.045 \pm 0.183	-	-	-0.045 \pm 0.231	-	-
+SEAL	0.076 \pm 0.153	+68.9%	-	-0.061 \pm 0.208	+35.6%	-
UNIv2	0.339 \pm 0.155	-	-	0.251 \pm 0.208	-	-
+SEAL	0.309 \pm 0.199	-8.8%	-	0.309 \pm 0.212	+23.1%	-
VIRCHOW2	0.436 \pm 0.154	-	-	0.423 \pm 0.178	-	-
+SEAL	0.503 \pm 0.163	+15.4%	*	0.402 \pm 0.221	-5.0%	-
Average	0.270 \pm 0.169	-	-	0.218 \pm 0.211	-	-
+SEAL	0.326 \pm 0.181	+20.9%	-	0.248 \pm 0.228	+13.8%	-

Extended Data Table 46: Performance comparison between SEAL fine-tuned encoders and vision-only baselines on the **CPTAC GBM** dataset, showing the **Epithelial-Mesenchymal Transition Pathway regression** task (n=243). This is a slide-level task evaluated using **PCC** across 10 cross-validation folds. The best-performing model for each encoder backbone in **bold**.

Model	ABMIL			MeanMIL		
	PCC (\uparrow)	% change	Sig.	PCC (\uparrow)	% change	Sig.
CONCH	0.505 \pm 0.146	-	-	0.065 \pm 0.223	-	-
+SEAL	0.485 \pm 0.181	-4.0%	-	0.027 \pm 0.251	-58.5%	-
H0MINI	0.480 \pm 0.247	-	-	0.525 \pm 0.177	-	-
+SEAL	0.621 \pm 0.102	+29.4%	*	0.168 \pm 0.293	-68.0%	-
PHIKON2	0.481 \pm 0.198	-	-	-0.080 \pm 0.252	-	-
+SEAL	0.466 \pm 0.189	-3.1%	-	-0.097 \pm 0.277	+21.3%	-
UNIv2	0.453 \pm 0.151	-	-	-0.068 \pm 0.165	-	-
+SEAL	0.552 \pm 0.153	+21.9%	*	-0.092 \pm 0.234	+35.3%	-
VIRCHOW2	0.579 \pm 0.180	-	-	0.574 \pm 0.158	-	-
+SEAL	0.666 \pm 0.123	+15.0%	*	0.613 \pm 0.192	+6.8%	-
Average	0.500 \pm 0.184	-	-	0.203 \pm 0.195	-	-
+SEAL	0.558 \pm 0.150	+11.7%	-	0.124 \pm 0.249	-39.1%	-

Extended Data Table 47: Performance comparison between SEAL fine-tuned encoders and vision-only baselines on the **CPTAC GBM** dataset, showing the **G2/M Checkpoint Pathway regression** task (n=243). This is a slide-level task evaluated using **PCC** across 10 cross-validation folds. The best-performing model for each encoder backbone in **bold**.

Model	ABMIL			MeanMIL		
	PCC (\uparrow)	% change	Sig.	PCC (\uparrow)	% change	Sig.
CONCH	0.454 \pm 0.158	-	-	0.034 \pm 0.267	-	-
+SEAL	0.504 \pm 0.213	+11.0%	-	0.061 \pm 0.234	+79.4%	-
H0MINI	0.473 \pm 0.196	-	-	0.436 \pm 0.158	-	-
+SEAL	0.514 \pm 0.162	+8.7%	-	-0.079 \pm 0.255	-118.1%	-
PHIKON2	0.156 \pm 0.241	-	-	-0.117 \pm 0.249	-	-
+SEAL	0.304 \pm 0.195	+94.9%	*	-0.084 \pm 0.224	-28.2%	-
UNIv2	0.381 \pm 0.174	-	-	0.054 \pm 0.235	-	-
+SEAL	0.535 \pm 0.124	+40.4%	-	0.039 \pm 0.205	-27.8%	-
VIRCHOW2	0.454 \pm 0.149	-	-	0.356 \pm 0.201	-	-
+SEAL	0.500 \pm 0.119	+10.1%	-	0.441 \pm 0.170	+23.9%	*
Average	0.384 \pm 0.184	-	-	0.153 \pm 0.222	-	-
+SEAL	0.471 \pm 0.163	+22.9%	-	0.076 \pm 0.218	-50.5%	-

Extended Data Table 48: Performance comparison between SEAL fine-tuned encoders and vision-only baselines on the **CPTAC GBM** dataset, showing the **Upregulated genes in PI3K/AKT/mTOR signaling Pathway regression** task (n=243). This is a slide-level task evaluated using **PCC** across 10 cross-validation folds. The best-performing model for each encoder backbone in **bold**.

Model	ABMIL			MeanMIL		
	PCC (\uparrow)	% change	Sig.	PCC (\uparrow)	% change	Sig.
CONCH	0.277 \pm 0.151	-	-	0.133 \pm 0.269	-	-
+SEAL	0.493 \pm 0.115	+78.0%	-	0.101 \pm 0.212	-24.1%	-
H0MINI	0.238 \pm 0.133	-	-	0.188 \pm 0.150	-	-
+SEAL	0.378 \pm 0.119	+58.8%	-	0.236 \pm 0.259	+25.5%	-
PHIKON2	0.196 \pm 0.134	-	-	0.003 \pm 0.275	-	-
+SEAL	0.197 \pm 0.131	+0.5%	-	-0.029 \pm 0.289	-1066.7%	-
UNIv2	0.118 \pm 0.161	-	-	-0.004 \pm 0.258	-	-
+SEAL	0.193 \pm 0.182	+63.6%	*	-0.023 \pm 0.247	+475.0%	-
VIRCHOW2	0.346 \pm 0.153	-	-	0.335 \pm 0.198	-	-
+SEAL	0.350 \pm 0.146	+1.2%	-	0.289 \pm 0.198	-13.7%	-
Average	0.235 \pm 0.146	-	-	0.131 \pm 0.230	-	-
+SEAL	0.322 \pm 0.139	+37.1%	-	0.115 \pm 0.241	-12.4%	-

Extended Data Table 49: Performance comparison between SEAL fine-tuned encoders and vision-only baselines on the **CPTAC LUAD** dataset, showing the **Epithelial-Mesenchymal Transition Pathway regression** task (n=324). This is a slide-level task evaluated using **PCC** across 10 cross-validation folds. The best-performing model for each encoder backbone in **bold**.

Model	ABMIL			MeanMIL		
	PCC (\uparrow)	% change	Sig.	PCC (\uparrow)	% change	Sig.
CONCH	0.435 \pm 0.121	-	-	0.328 \pm 0.124	-	-
+SEAL	0.577 \pm 0.121	+32.6%	*	0.452 \pm 0.126	+37.8%	**
H0MINI	0.451 \pm 0.112	-	-	0.262 \pm 0.186	-	-
+SEAL	0.473 \pm 0.096	+4.9%	-	0.415 \pm 0.136	+58.4%	*
PHIKON2	0.200 \pm 0.177	-	-	-0.052 \pm 0.215	-	-
+SEAL	0.188 \pm 0.176	-6.0%	-	-0.018 \pm 0.230	-65.4%	-
UNIv2	0.238 \pm 0.135	-	-	0.007 \pm 0.158	-	-
+SEAL	0.405 \pm 0.165	+70.2%	**	0.329 \pm 0.180	+4600.0%	-
VIRCHOW2	0.488 \pm 0.190	-	-	0.483 \pm 0.155	-	-
+SEAL	0.509 \pm 0.152	+4.3%	-	0.363 \pm 0.151	-24.8%	-
Average	0.362 \pm 0.147	-	-	0.206 \pm 0.168	-	-
+SEAL	0.430 \pm 0.142	+18.8%	-	0.308 \pm 0.165	+49.9%	-

Extended Data Table 50: Performance comparison between SEAL fine-tuned encoders and vision-only baselines on the **CPTAC LUAD** dataset, showing the **G2/M Checkpoint Pathway regression** task (n=324). This is a slide-level task evaluated using **PCC** across 10 cross-validation folds. The best-performing model for each encoder backbone in **bold**.

Model	ABMIL			MeanMIL		
	PCC (↑)	% change	Sig.	PCC (↑)	% change	Sig.
CONCH	0.736 ± 0.067	-	-	0.660 ± 0.143	-	-
+SEAL	0.742 ± 0.064	+0.8%	-	0.715 ± 0.118	+8.3%	*
H0MINI	0.670 ± 0.134	-	-	0.497 ± 0.168	-	-
+SEAL	0.773 ± 0.056	+15.4%	**	0.738 ± 0.086	+48.5%	-
PHIKON2	0.616 ± 0.075	-	-	-0.110 ± 0.314	-	-
+SEAL	0.619 ± 0.135	+0.5%	-	-0.081 ± 0.359	-26.4%	-
UNIv2	0.626 ± 0.149	-	-	0.325 ± 0.182	-	-
+SEAL	0.761 ± 0.073	+21.6%	**	0.680 ± 0.139	+109.2%	-
VIRCHOW2	0.721 ± 0.109	-	-	0.725 ± 0.088	-	-
+SEAL	0.762 ± 0.088	+5.7%	*	0.692 ± 0.082	-4.6%	-
Average	0.674 ± 0.107	-	-	0.419 ± 0.179	-	-
+SEAL	0.731 ± 0.083	+8.5%	-	0.549 ± 0.157	+30.9%	-

Extended Data Table 51: Performance comparison between SEAL fine-tuned encoders and vision-only baselines on the **CPTAC LUAD** dataset, showing the **Upregulated genes in PI3K/AKT/mTOR signaling Pathway regression** task (n=324). This is a slide-level task evaluated using **PCC** across 10 cross-validation folds. The best-performing model for each encoder backbone in **bold**.

Model	ABMIL			MeanMIL		
	PCC (↑)	% change	Sig.	PCC (↑)	% change	Sig.
CONCH	0.217 ± 0.128	-	-	0.112 ± 0.099	-	-
+SEAL	0.392 ± 0.147	+80.6%	-	0.397 ± 0.123	+254.5%	-
H0MINI	0.270 ± 0.198	-	-	0.077 ± 0.270	-	-
+SEAL	0.344 ± 0.150	+27.4%	*	0.318 ± 0.146	+313.0%	**
PHIKON2	0.105 ± 0.139	-	-	-0.115 ± 0.266	-	-
+SEAL	0.199 ± 0.145	+89.5%	-	-0.111 ± 0.265	-3.5%	-
UNIv2	0.241 ± 0.174	-	-	-0.110 ± 0.214	-	-
+SEAL	0.330 ± 0.125	+36.9%	-	0.212 ± 0.099	-292.7%	-
VIRCHOW2	0.353 ± 0.141	-	-	0.417 ± 0.144	-	-
+SEAL	0.368 ± 0.153	+4.2%	-	0.270 ± 0.156	-35.3%	-
Average	0.237 ± 0.156	-	-	0.076 ± 0.199	-	-
+SEAL	0.327 ± 0.144	+37.7%	-	0.217 ± 0.158	+185.0%	-

Extended Data Table 52: Performance comparison between SEAL fine-tuned encoders and vision-only baselines on the **CPTAC PDA** dataset, showing the **Epithelial-Mesenchymal Transition Pathway regression** task (n=242). This is a slide-level task evaluated using **PCC** across 10 cross-validation folds. The best-performing model for each encoder backbone in **bold**.

Model	ABMIL			MeanMIL		
	PCC (\uparrow)	% change	Sig.	PCC (\uparrow)	% change	Sig.
CONCH	0.357 \pm 0.138	-	-	0.359 \pm 0.132	-	-
+SEAL	0.413 \pm 0.152	+15.7%	-	0.386 \pm 0.146	+7.5%	-
HOMINI	0.341 \pm 0.081	-	-	0.236 \pm 0.209	-	-
+SEAL	0.380 \pm 0.113	+11.4%	-	0.422 \pm 0.124	+78.8%	*
PHIKON2	0.103 \pm 0.156	-	-	-0.039 \pm 0.221	-	-
+SEAL	0.209 \pm 0.257	+102.9%	-	-0.042 \pm 0.232	+7.7%	-
UNIV2	0.087 \pm 0.156	-	-	-0.014 \pm 0.177	-	-
+SEAL	0.217 \pm 0.171	+149.4%	*	0.001 \pm 0.177	-107.1%	-
VIRCHOW2	0.441 \pm 0.128	-	-	0.407 \pm 0.125	-	-
+SEAL	0.462 \pm 0.089	+4.8%	-	0.411 \pm 0.096	+1.0%	-
Average	0.266 \pm 0.132	-	-	0.190 \pm 0.173	-	-
+SEAL	0.336 \pm 0.156	+26.5%	-	0.236 \pm 0.155	+24.1%	-

Extended Data Table 53: Performance comparison between SEAL fine-tuned encoders and vision-only baselines on the **CPTAC PDA** dataset, showing the **G2/M Checkpoint Pathway regression** task (n=242). This is a slide-level task evaluated using **PCC** across 10 cross-validation folds. The best-performing model for each encoder backbone in **bold**.

Model	ABMIL			MeanMIL		
	PCC (\uparrow)	% change	Sig.	PCC (\uparrow)	% change	Sig.
CONCH	0.495 \pm 0.160	-	-	0.430 \pm 0.152	-	-
+SEAL	0.624 \pm 0.111	+26.1%	**	0.648 \pm 0.112	+50.7%	-
H0MINI	0.387 \pm 0.238	-	-	0.078 \pm 0.141	-	-
+SEAL	0.521 \pm 0.193	+34.6%	**	0.537 \pm 0.179	+588.5%	-
PHIKON2	0.010 \pm 0.184	-	-	-0.025 \pm 0.150	-	-
+SEAL	0.207 \pm 0.256	+1970.0%	*	0.012 \pm 0.213	-148.0%	-
UNIv2	0.242 \pm 0.164	-	-	0.193 \pm 0.220	-	-
+SEAL	0.463 \pm 0.073	+91.3%	**	0.324 \pm 0.208	+67.9%	**
VIRCHOW2	0.467 \pm 0.170	-	-	0.498 \pm 0.174	-	-
+SEAL	0.682 \pm 0.129	+46.0%	-	0.544 \pm 0.137	+9.2%	-
Average	0.320 \pm 0.183	-	-	0.235 \pm 0.167	-	-
+SEAL	0.499 \pm 0.152	+56.0%	-	0.413 \pm 0.170	+75.9%	-

Extended Data Table 54: Performance comparison between SEAL fine-tuned encoders and vision-only baselines on the **CPTAC PDA** dataset, showing the **Upregulated genes in PI3K/AKT/mTOR signaling Pathway regression** task (n=242). This is a slide-level task evaluated using PCC across 10 cross-validation folds. The best-performing model for each encoder backbone in **bold**.

Model	ABMIL			MeanMIL		
	PCC (\uparrow)	% change	Sig.	PCC (\uparrow)	% change	Sig.
CONCH	0.143 \pm 0.186	-	-	0.094 \pm 0.167	-	-
+SEAL	0.238 \pm 0.162	+66.4%	-	0.241 \pm 0.168	+156.4%	*
H0MINI	0.060 \pm 0.174	-	-	0.032 \pm 0.141	-	-
+SEAL	0.186 \pm 0.134	+210.0%	*	0.206 \pm 0.121	+543.7%	**
PHIKON2	0.060 \pm 0.192	-	-	-0.017 \pm 0.222	-	-
+SEAL	-0.175 \pm 0.227	-391.7%	-	-0.051 \pm 0.226	+200.0%	-
UNIv2	0.161 \pm 0.233	-	-	0.211 \pm 0.167	-	-
+SEAL	0.207 \pm 0.236	+28.6%	-	0.201 \pm 0.183	-4.7%	-
VIRCHOW2	0.188 \pm 0.087	-	-	0.175 \pm 0.081	-	-
+SEAL	0.175 \pm 0.190	-6.9%	-	0.250 \pm 0.159	+42.9%	-
Average	0.122 \pm 0.174	-	-	0.099 \pm 0.156	-	-
+SEAL	0.126 \pm 0.190	+3.1%	-	0.169 \pm 0.171	+71.1%	-

References

1. Song, A. H. *et al.* Artificial intelligence for digital and computational pathology. *Nature Reviews Bioengineering* **1**, 930–949 (2023).
2. Shmatko, A., Ghaffari Laleh, N., Gerstung, M. & Kather, J. N. Artificial intelligence in histopathology: enhancing cancer research and clinical oncology. *Nature cancer* **3**, 1026–1038 (2022).
3. Van der Laak, J., Litjens, G. & Ciompi, F. Deep learning in histopathology: the path to the clinic. *Nature medicine* **27**, 775–784 (2021).
4. Campanella, G. *et al.* A clinical benchmark of public self-supervised pathology foundation models. *Nature Communications* **16**, 3640 (2025).
5. Chen, R. J. *et al.* Towards a general-purpose foundation model for computational pathology. *Nature Medicine* 1–13 (2024).
6. Wang, X. *et al.* Transformer-based unsupervised contrastive learning for histopathological image classification. *Medical image analysis* **81**, 102559 (2022).
7. Zimmermann, E. *et al.* Virchow2: Scaling Self-Supervised Mixed Magnification Models in Pathology (2024). 2408.00738.
8. Saillard, C. *et al.* H-optimus-0 (2024). URL <https://github.com/bioptimus/releases/tree/main/models/h-optimus/v0>.
9. Filiot, A., Jacob, P., Mac Kain, A. & Saillard, C. Phikon-v2, a large and public feature extractor for biomarker prediction. *arXiv preprint arXiv:2409.09173* (2024).
10. Neidlinger, P. *et al.* Benchmarking foundation models as feature extractors for weakly supervised computational pathology. *Nature Biomedical Engineering* 1–11 (2025).
11. Huang, Z., Bianchi, F., Yuksekgonul, M., Montine, T. J. & Zou, J. A visual–language foundation model for pathology image analysis using medical twitter. *Nature medicine* **29**, 2307–2316 (2023).
12. Lu, M. Y. *et al.* A visual-language foundation model for computational pathology. *Nature Medicine* **30**, 863–874 (2024).
13. Xiang, J. *et al.* A vision–language foundation model for precision oncology. *Nature* **638**, 769–778 (2025).
14. Wang, X. *et al.* A pathology foundation model for cancer diagnosis and prognosis prediction. *Nature* **634**, 970–978 (2024).
15. Ding, T. *et al.* A multimodal whole-slide foundation model for pathology. *Nature Medicine* 1–13 (2025).

16. Shaikovski, G. *et al.* PRISM: A Multi-Modal Generative Foundation Model for Slide-Level Histopathology (2024). 2405.10254.
17. Xu, H. *et al.* A whole-slide foundation model for digital pathology from real-world data. *Nature* **630**, 181–188 (2024).
18. Jaume, G. *et al.* Transcriptomics-guided slide representation learning in computational pathology. In *Proceedings of the IEEE/CVF Conference on Computer Vision and Pattern Recognition*, 9632–9644 (2024).
19. Jaume, G. *et al.* Multistain pretraining for slide representation learning in pathology. In *Computer Vision – European Conference on Computer Vision 2024*, 19–37 (Springer Nature Switzerland, Cham, 2025).
20. Vaidya, A. *et al.* Molecular-driven Foundation Model for Oncologic Pathology (2025). 2501.16652.
21. Ståhl, P. L. *et al.* Visualization and analysis of gene expression in tissue sections by spatial transcriptomics. *Science* **353**, 78–82 (2016).
22. Moses, L. & Pachter, L. Museum of spatial transcriptomics. *Nature methods* **19**, 534–546 (2022).
23. Marx, V. Method of the year: spatially resolved transcriptomics. *Nature methods* **18**, 9–14 (2021).
24. Tian, L., Chen, F. & Macosko, E. Z. The expanding vistas of spatial transcriptomics. *Nature Biotechnology* **41**, 773–782 (2023).
25. Jaume, G. *et al.* Hest-1k: A dataset for spatial transcriptomics and histology image analysis. *Advances in Neural Information Processing Systems* **37**, 53798–53833 (2024).
26. Rao, A., Barkley, D., França, G. S. & Yanai, I. Exploring tissue architecture using spatial transcriptomics. *Nature* **596**, 211–220 (2021).
27. Mo, C.-K. *et al.* Tumour evolution and microenvironment interactions in 2D and 3D space. *Nature* **634**, 1178–1186 (2024).
28. He, B. *et al.* Integrating spatial gene expression and breast tumour morphology via deep learning. *Nature Biomedical Engineering* **4**, 827–834 (2020).
29. Xie, R. *et al.* Spatially Resolved Gene Expression Prediction from Histology Images via Bi-modal Contrastive Learning. *Advances in Neural Information Processing Systems* **36**, 70626–70637 (2023).
30. Lee, Y., Liu, X., Hao, M., Liu, T. & Regev, A. Pathomclip: Connecting tumor histology with spatial gene expression via locally enhanced contrastive learning of pathology and single-cell foundation model. *bioRxiv* 2024–12 (2024).

31. Han, M. *et al.* Towards unified molecule-enhanced pathology image representation learning via integrating spatial transcriptomics. *Pattern Recognition* 112458 (2025).
32. Chung, Y., Ha, J. H., Im, K. C. & Lee, J. S. Accurate Spatial Gene Expression Prediction by Integrating Multi-Resolution Features. In *Proceedings of the IEEE/CVF Conference on Computer Vision and Pattern Recognition*, 11591–11600 (2024).
33. Chen, W. *et al.* A visual–omics foundation model to bridge histopathology with spatial transcriptomics. *Nature Methods* 1–15 (2025).
34. Zhang, D. *et al.* Inferring super-resolution tissue architecture by integrating spatial transcriptomics with histology. *Nature Biotechnology* **42**, 1372–1377 (2024).
35. Schroeder, A. *et al.* Scaling up spatial transcriptomics for large-sized tissues: uncovering cellular-level tissue architecture beyond conventional platforms with iscale. *Nature methods* 1–12 (2025).
36. Huang, T., Liu, T., Babadi, M., Jin, W. & Ying, R. Scalable generation of spatial transcriptomics from histology images via whole-slide flow matching. *arXiv preprint arXiv:2506.05361* (2025).
37. Gindra, R. H. *et al.* A large-scale benchmark of cross-modal learning for histology and gene expression in spatial transcriptomics. *arXiv preprint arXiv:2508.01490* (2025).
38. Chen, J. *et al.* STImage-1K4M: A histopathology image-gene expression dataset for spatial transcriptomics. *Advances in Neural Information Processing Systems* **37**, 35796–35823 (2024).
39. Echle, A. *et al.* Deep learning in cancer pathology: a new generation of clinical biomarkers. *British journal of cancer* **124**, 686–696 (2021).
40. Ramasesh, V. V., Lewkowycz, A. & Dyer, E. Effect of scale on catastrophic forgetting in neural networks. In *International Conference on Learning Representations* (2021).
41. Filion, A. *et al.* Distilling foundation models for robust and efficient models in digital pathology. In *International Conference on Medical Image Computing and Computer-Assisted Intervention*, 162–172 (Springer, 2025).
42. Dosovitskiy, A. *et al.* An image is worth 16x16 words: Transformers for image recognition at scale. *arXiv preprint arXiv:2010.11929* (2020).
43. Yan, G., Hua, S. H. & Li, J. J. Categorization of 34 computational methods to detect spatially variable genes from spatially resolved transcriptomics data. *Nature Communications* **16**, 1141 (2025).
44. Radford, A. *et al.* Learning transferable visual models from natural language supervision. In *International conference on machine learning*, 8748–8763 (PMLR, 2021).

45. Hu, E. J. *et al.* Lora: Low-rank adaptation of large language models. *ICLR* **1**, 3 (2022).
46. He, B. *et al.* Integrating spatial gene expression and breast tumour morphology via deep learning. *Nature Biomedical Engineering* **4**, 827–834 (2020).
47. Zeng, Y. *et al.* Spatial transcriptomics prediction from histology jointly through transformer and graph neural networks. *Briefings in Bioinformatics* **23** (2022).
48. Wang, Y. *et al.* FmH2ST: Foundation model-based spatial transcriptomics generation from histological images. *Nucleic Acids Research* **53**, gkaf865 (2025).
49. Nonchev, K. *et al.* Deepspot: Leveraging spatial context for enhanced spatial transcriptomics prediction from h&e images. *medRxiv* 2025–02 (2025).
50. Min, W., Shi, Z., Zhang, J., Wan, J. & Wang, C. Multimodal contrastive learning for spatial gene expression prediction using histology images. *Briefings in Bioinformatics* **25**, bbae551 (2024).
51. Lin, Y. *et al.* St-align: A multimodal foundation model for image-gene alignment in spatial transcriptomics. *arXiv preprint arXiv:2411.16793* (2024).
52. Wang, Q., Chen, W.-j., Su, J., Wang, G. & Song, Q. HECLIP: Histology-enhanced contrastive learning for imputation of transcriptomics profiles. *Bioinformatics* **41**, btaf363 (2025).
53. Ilse, M., Tomczak, J. & Welling, M. Attention-based deep multiple instance learning. In *International conference on machine learning*, 2127–2136 (PMLR, 2018).
54. Lu, M. Y. *et al.* Data-efficient and weakly supervised computational pathology on whole-slide images. *Nature biomedical engineering* **5**, 555–570 (2021).
55. Zaheer, M. *et al.* Deep sets. *Advances in neural information processing systems* **30** (2017).
56. Tellez, D. *et al.* Quantifying the effects of data augmentation and stain color normalization in convolutional neural networks for computational pathology. *Medical image analysis* **58**, 101544 (2019).
57. Stacke, K., Eilertsen, G., Unger, J. & Lundström, C. Measuring domain shift for deep learning in histopathology. *IEEE journal of biomedical and health informatics* **25**, 325–336 (2020).
58. Howard, F. M. *et al.* The impact of site-specific digital histology signatures on deep learning model accuracy and bias. *Nature communications* **12**, 4423 (2021).
59. Ghaffari Laleh, N. *et al.* Adversarial attacks and adversarial robustness in computational pathology. *Nature communications* **13**, 5711 (2022).

60. Um, I. H. *et al.* Whole Slide Images of H&E Sections Digitised on Multiple Scanners. <https://www.ebi.ac.uk/biostudies/bioimages/studies/S-BIAD1343> (2024).

61. Kömen, J. *et al.* Towards robust foundation models for digital pathology. *arXiv preprint arXiv:2507.17845* (2025).

62. BinTayyash, N. *et al.* Non-parametric modelling of temporal and spatial counts data from rna-seq experiments. *Bioinformatics* **37**, 3788–3795 (2021).

63. Danaher, P. *et al.* Advances in mixed cell deconvolution enable quantification of cell types in spatial transcriptomic data. *Nature communications* **13**, 385 (2022).

64. Jia, C. *et al.* Scaling up visual and vision-language representation learning with noisy text supervision. In *International conference on machine learning*, 4904–4916 (PMLR, 2021).

65. Liberzon, A. *et al.* The molecular signatures database hallmark gene set collection. *Cell systems* **1**, 417–425 (2015).

66. Ma, C. *et al.* The prostate stromal transcriptome in aggressive and lethal prostate cancer. *Molecular Cancer Research* **21**, 253–260 (2023).

67. Fujita, K. & Nonomura, N. Role of androgen receptor in prostate cancer: a review. *World Journal of Men's Health* **37** (2019).

68. Theodoris, C. V. *et al.* Transfer learning enables predictions in network biology. *Nature* **618**, 616–624 (2023).

69. Cui, H. *et al.* scGPT: Toward building a foundation model for single-cell multi-omics using generative AI. *Nature Methods* **21**, 1470–1480 (2024).

70. De Ruiter, J. pybiomart: A simple pythonic interface to biomart. <https://github.com/jrderuiter/pybiomart> (2016).

71. Stuart, T. *et al.* Comprehensive Integration of Single-Cell Data. *Cell* **177**, 1888–1902.e21 (2019).

72. Sondka, Z. *et al.* The cosmic cancer gene census: describing genetic dysfunction across all human cancers. *Nature Reviews Cancer* **18**, 696–705 (2018).

73. Kingma, D. P., Salimans, T. & Welling, M. Variational Dropout and the Local Reparameterization Trick. In *Advances in Neural Information Processing Systems*, vol. 28 (Curran Associates, Inc., 2015).

74. He, K., Zhang, X., Ren, S. & Sun, J. Deep Residual Learning for Image Recognition. In *2016 IEEE Conference on Computer Vision and Pattern Recognition (CVPR)*, 770–778 (2016).

75. Tian, T., Zhang, J., Lin, X., Wei, Z. & Hakonarson, H. Dependency-aware deep generative models for multitasking analysis of spatial omics data. *Nature Methods* **21**, 1501–1513 (2024).

76. Rezende, D. & Mohamed, S. Variational inference with normalizing flows. In *International conference on machine learning*, 1530–1538 (PMLR, 2015).

77. Zbontar, J., Jing, L., Misra, I., LeCun, Y. & Deny, S. Barlow Twins: Self-Supervised Learning via Redundancy Reduction. In *Proceedings of the 38th International Conference on Machine Learning*, 12310–12320 (PMLR, 2021).

78. Kingma, D. P. & Ba, J. Adam: A Method for Stochastic Optimization. In *ICLR 2015* (arXiv, 2017). 1412.6980.

79. Ganin, Y. & Lempitsky, V. Unsupervised Domain Adaptation by Backpropagation. In *Proceedings of the 32nd International Conference on Machine Learning*, 1180–1189 (PMLR, 2015).

80. Sammut, S.-J. *et al.* Multi-omic machine learning predictor of breast cancer therapy response. *Nature* **601**, 623–629 (2022).

81. Xu, F. *et al.* Predicting axillary lymph node metastasis in early breast cancer using deep learning on primary tumor biopsy slides. *Frontiers in oncology* **11**, 759007 (2021).

82. Brancati, N. *et al.* BRACS: A Dataset for BReAst Carcinoma Subtyping in H&E Histology Images. *Database* **2022** (2022).

83. Edwards, N. J. *et al.* The CPTAC Data Portal: A Resource for Cancer Proteomics Research. *Journal of Proteome Research* **14**, 2707–2713 (2015).

84. Thangudu, R. R. *et al.* Abstract LB-242: Proteomic Data Commons: A resource for proteogenomic analysis. *Cancer Research* **80** (2020).

85. Liberzon, A. *et al.* The molecular signatures database hallmark gene set collection. *Cell Systems* **1**, 417–425 (2015).

86. Farahmand, S. *et al.* Deep learning trained on hematoxylin and eosin tumor region of Interest predicts HER2 status and trastuzumab treatment response in HER2+ breast cancer. *Mod. Pathol.* **35**, 44–51 (2022).

87. Roetzer-Pejrimovsky, T. *et al.* The Digital Brain Tumour Atlas, an open histopathology resource. *Scientific Data* **9**, 1–6 (2022).

88. Vaidya, A. *et al.* Demographic bias in misdiagnosis by computational pathology models. *Nature Medicine* **30**, 1174–1190 (2024).

89. Acosta, P. H. *et al.* Intratumoral resolution of driver gene mutation heterogeneity in renal cancer using deep learning. *Cancer research* **82**, 2792–2806 (2022).
90. Wang, C.-W. *et al.* Weakly supervised deep learning for prediction of treatment effectiveness on ovarian cancer from histopathology images. *Computerized Medical Imaging and Graphics* **99**, 102093 (2022).
91. Bulten, W. *et al.* Artificial intelligence for diagnosis and gleason grading of prostate cancer: the panda challenge. *Nature medicine* **28**, 154–163 (2022).
92. Pati, P. *et al.* Hierarchical graph representations in digital pathology. *Medical Image Analysis* **75**, 102264 (2022).
93. Myles, C., Um, I. H., Harrison, D. J. & Harris-Birtill, D. Leveraging foundation models for enhanced detection of colorectal cancer biomarkers in small datasets. In *Annual Conference on Medical Image Understanding and Analysis*, 329–343 (Springer, 2024).